

École doctorale n° 364 : Sciences Fondamentales et Appliquées

## Doctorat ParisTech

### THÈSE

pour obtenir le grade de docteur délivré par

**L'École Nationale Supérieure des Mines de Paris**

**Spécialité doctorale “Science et Génie des Matériaux”**

*présentée et soutenue publiquement par*

**Ali SAAD**

le xx mai 2015

## NUMERICAL MODELLING OF MACROSEGREGATION INDUCED BY SOLIDIFICATION SHRINKAGE IN A LEVEL SET APPROACH

Directeurs de thèse: **Michel BELLET**  
**Charles-André GANDIN**

### Jury

<b>M. Blablabla</b> ,	Professeur, MINES ParisTech	Rapporteur
<b>M. Blablabla</b> ,	Professeur, Arts Et Métiers ParisTech	Rapporteur
<b>M. Blablabla</b> ,	Chargé de recherche, ENS Cachan	Examinateur
<b>M. Blablabla</b> ,	Danseuse, en freelance	Examinateur
<b>M. Blablabla</b> ,	Ingénieur, MIT	Examinateur

T  
H  
E  
S  
S



# Contents

<b>1 General Introduction</b>	<b>1</b>
1.1 Casting defects . . . . .	1
1.2 Macrosegregation . . . . .	4
1.2.1 Causes . . . . .	4
1.2.2 Examples . . . . .	5
1.3 Industrial Worries . . . . .	7
1.4 Project context and objectives . . . . .	8
1.4.1 Context . . . . .	8
1.4.2 Objectives and outline . . . . .	10
<b>2 Modelling Review</b>	<b>13</b>
2.1 Modelling macrosegregation . . . . .	14
2.1.1 Dendritic growth . . . . .	14
2.1.2 Mush permeability . . . . .	14
2.1.3 Microsegregation . . . . .	16
2.1.4 Macroscopic solidification model: monodomain . . . . .	18
2.2 Eulerian and Lagrangian motion description . . . . .	24
2.2.1 Overview . . . . .	24
2.2.2 Interface capturing . . . . .	26
2.3 Solidification models with level set . . . . .	26
2.4 The level set method . . . . .	27
2.4.1 Diffuse interface . . . . .	28
2.4.2 Mixing Laws . . . . .	29
2.5 Interface motion . . . . .	31
2.5.1 Level set transport . . . . .	32
2.5.2 Level set regularisation . . . . .	33
<b>3 Energy balance with thermodynamic tabulations</b>	<b>39</b>
3.1 State of the art . . . . .	40
3.2 Thermodynamic considerations . . . . .	40
3.2.1 Volume averaging . . . . .	40

## Contents

---

3.2.2	The temperature-enthalpy relationship . . . . .	41
3.2.3	Tabulation of properties . . . . .	42
3.3	Numerical method . . . . .	43
3.3.1	Enthalpy-based approach . . . . .	47
3.3.2	Temperature-based approach . . . . .	47
3.3.3	Convergence . . . . .	48
3.4	Validation . . . . .	49
3.4.1	Pure diffusion . . . . .	49
3.4.2	Convection and diffusion . . . . .	52
3.5	Application: multicomponent alloy solidification . . . . .	55
3.5.1	Tabulations . . . . .	57
3.5.2	Discussion . . . . .	58
<b>4</b>	<b>Macrosegregation with liquid metal motion</b>	<b>63</b>
4.1	Introduction . . . . .	64
4.2	Numerical treatment . . . . .	64
4.2.1	Stable mixed finite elements . . . . .	64
4.2.2	Variational multiscale (VMS) . . . . .	64
4.3	VMS solver . . . . .	65
4.4	Computational stability . . . . .	66
4.4.1	CFL condition . . . . .	66
4.4.2	Integration order . . . . .	66
4.5	Application to multicomponent alloys . . . . .	66
4.5.1	Results . . . . .	68
4.6	Macroscopic freckle prediction . . . . .	69
4.6.1	Introduction . . . . .	71
4.6.2	Experimental work . . . . .	72
4.6.3	Macroscopic scale simulations . . . . .	72
4.7	Meso-Macro freckle prediction . . . . .	79
4.7.1	Numerical method . . . . .	79
4.7.2	Configuration . . . . .	81
4.7.3	Effect of vertical temperature gradient . . . . .	84
4.7.4	Effect of cooling rate . . . . .	86
4.7.5	Effect of lateral temperature gradient . . . . .	88
<b>5</b>	<b>Macrosegregation with solidification shrinkage</b>	<b>91</b>
5.1	Introduction . . . . .	92
5.2	FE model: Metal . . . . .	92
5.2.1	Mass and momentum conservation . . . . .	94
5.2.2	Energy conservation . . . . .	95
5.2.3	Species conservation . . . . .	97

## Contents

---

5.3	FE model: Air . . . . .	98
5.3.1	Mass and momentum conservation . . . . .	99
5.3.2	Energy conservation . . . . .	99
5.3.3	Species conservation . . . . .	99
5.4	FE monolithic model . . . . .	99
5.4.1	Permeability mixing . . . . .	99
5.4.2	Model equations . . . . .	99
5.4.3	Interface treatment . . . . .	100
5.5	Shrinkage without macrosegregation . . . . .	102
5.5.1	Al-7wt% Si . . . . .	102
5.5.2	Pb-3wt% Sn . . . . .	103
5.6	Shrinkage with macrosegregation . . . . .	103
5.6.1	Al-7wt% Si . . . . .	103
5.6.2	Pb-3wt% Sn . . . . .	103
	<b>Bibliography</b>	<b>105</b>

## **Contents**

---

---

<b>Acronym</b>	<b>Standing for</b>
ALE	Arbitrary Lagrangian-Eulerian
CCEMLCC	Chill Cooling for the Electro-Magnetic Levitator in relation with Continuous Casting of steel
CEMEF	Center for Material Forming
CSF	Continuum Surface Force
DLR	Deutsches Zentrum für Luft- und Raumfahrt
EML	Electromagnetic levitation
ESA	European Space Agency
FEM	Finite Element Method
GMAW	Gas Metal Arc Welding
ISS	International Space Station
IWT	Institut für Werkstofftechnik
LHS	Left Hand Side
LSM	Level set method
MAC	Marker-and-cell
MIN	Mini-element
PF	Phase field
RHS	Right Hand Side
RUB	Ruhr Universität Bochum
RVE	Representative Elementary Volume
SCPG	Shock Capturing Petrov-Galerkin
SUPG	Streamline Upwind Petrov-Galerkin
VMS	Variational MultiScale
VOF	Volume Of Fluid

---

## **Contents**

---

# Chapter 1

## General Introduction

**Macrosegregation** is a very known defect to metallurgical processes. Despite a great evolution achieved by active research during the last 60 years, it remains partially understood. Macrosegregation is often the consequence of several factors at the scale of a casting, all related to *microsegregation* happening at the scale of dendrites. Today, research in metallurgy focuses on a deeper understanding of such a connection between the different physical scales. Solidification is not only a phase change, but also a complex transformation involving small scales like nucleation, medium scales like grains growth and large scales like convection in the melt. From the nucleation theory to the mechanical behavior of metals, intricate phenomena combine to form defects in the final product. This has been seen in casting processes, such as continuous casting ([fig. 1.1](#)) and ingot casting. Surface and volume porosity, hot tearing and composition heterogeneity are known defects to the casting community. After a brief introduction of these defects, macrosegregation will be the focus of this dissertation.

### 1.1 Casting defects

Undesired effects are inevitable in any industrial process. More importantly, a lot of defects in the casting industry can be disastrous in some situations where the cast product is not serviceable and hence rejected. This leads to a systematic product recycling, i.e. the product is ditched to be reheated, remelted and then cast again. From an economic point view, the operation is expensive timewise and profitwise. Understanding and preventing defects when possible, is thus crucial in the casting industry. We briefly list hereafter the main encountered defects.

#### Hot tearing

This defect, also denoted solidification cracking or hot cracking, occurs in the mushy zone at high solid fractions when a failure or crack appears at specific locations, the hot

## Chapter 1. General Introduction

---

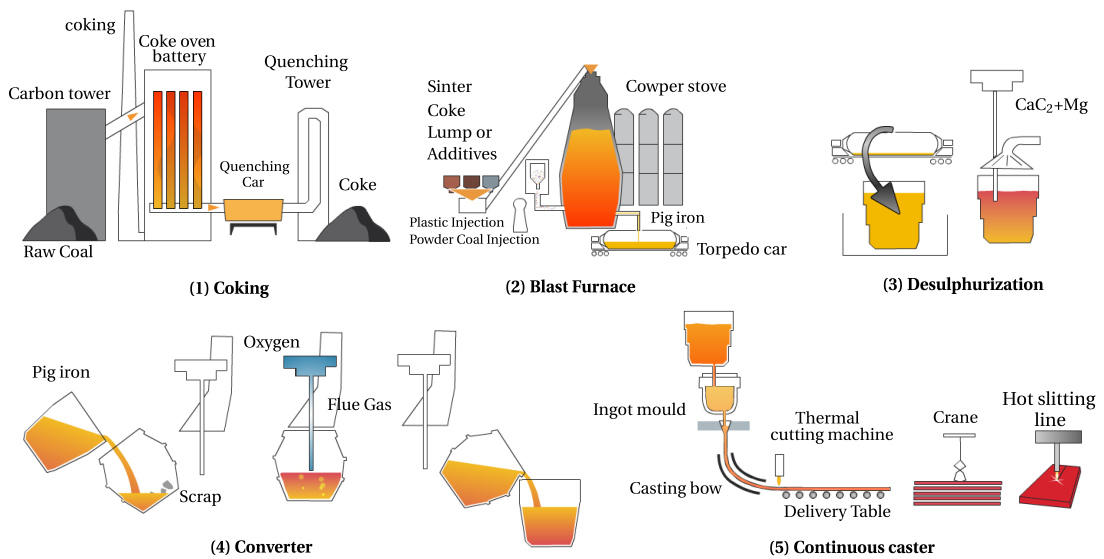


**Fig. 1.1 – Main steps in an integrated steel plant**

spots. The temperature range in which the steel is vulnerable to hot tearing is known as the brittleness temperature range (BTR). It corresponds to solid fractions greater than 90%, with the liquid phase forming a discontinuous film. Many factors can cause the failure, but the main origin is a lack of liquid feeding required to compensate for the solidification shrinkage, in the presence of thermal stresses in the mushy region. Therefore, a crack initiates then propagates in the casting, as shown in [fig. 1.2](#).



**Fig. 1.2 – Crack in an aluminium slab**

### Porosity

Porosity is a void defect formed inside the casting or at the outer surface. It may be attributed to two different factors. Firstly, we speak of *shrinkage porosity*, when a void forms as a result of density differences between the interdendritic liquid and solid network, the latter being denser than the former ([figs. 1.3c](#) and [1.3d](#)). It is basically, the same reason that initiates hot cracks. The second factor is the presence of dissolved

gaseous phases in the melt (figs. 1.3a and 1.3b). According to Dantzig et al. [2009], these gases may be initially in the melt, or created by the reaction between the metal and water found in the air or trapped in grooves at the moulds surface. If the decreasing temperature and pressure drop in the liquid are large enough, the latter becomes supersaturated. Consequently, the nucleation of gaseous phase is triggered (just like when a cold bottle of coca-cola is opened !).



**(a)** Gas porosity in casting  
[AFS 2014].



**(b)** Shrinkage porosity  
[AFS 2014].



**(c)** Gas porosity in aluminium welding [WeldReality 2014].



**(d)** Xray of volume void inside welded duplex steel [ESAB 2014].

**Fig. 1.3 – Examples of porosity in casting and welding**

### Freckles or segregated channels

The origin of this defect is a combined effect of microsegregation and buoyancy forces. Upon solidification, solid forms while rejecting some solute in the liquid due to partitioning (steels have a partition coefficient less than unity). When segregated solute is the lighter species, an increasing concentration in the liquid phase produces a solutal driving force inside the mushy zone, generating unstable convection currents, with "plume" shapes as often reported in the literature [Sarazin et al. 1992; Schneider et al. 1997; Shevchenko et al. 2013]. Temperature gradient is often an additional force of convection, the latter is hence qualified as "thermosolutal".

## 1.2 Macrosegregation

Macrosegregation generally stems from a solubility difference between a liquid phase and one or more solid phases, along with a relative velocity between these phases. While the former is responsible for local solute enrichment or depletion, the latter will propagate the composition heterogeneity on a scale much larger than just a few dendrites. This is why macrosegregation could be observed on the scale of a casting, up to several meters in length. While microsegregation can be healed by annealing the alloy to speed up the diffusion process and allow homogenization, heterogeneities spanning on larger distances cannot be treated after solidification. It is obvious that macrosegregation is irreversible defect. Failure to prevent it, may lead to a substantial decline in the alloy's mechanical behavior, hence its serviceability.

### 1.2.1 Causes

Four main factors can (simultaneously) cause fluid flow leading to macrosegregation:

#### Liquid dynamics

During solidification, thermal and solutal gradients result in density gradients in the liquid phase:

$$\rho^l = \rho_0^l(1 - \beta_T(T - T_0) - \sum_i \beta_{w_i^l}(w_i^l - \langle w_i \rangle_0^l)) \quad (1.1a)$$

$$\vec{\nabla} \rho^l = -\rho_0^l(\beta_T \vec{\nabla} T + \sum_i \beta_{w_i^l} \vec{\nabla} w_i^l) \quad (1.1b)$$

In eq. (1.1a), density is assumed to vary linearly with temperature and phase composition for each chemical species (index  $i$ ). The slopes defining such variations are respectively the thermal expansion coefficient  $\beta_T$  and the solutal expansion coefficients  $\beta_{w_i^l}$ , given by:

$$\beta_T = -\frac{1}{\rho_0^l} \left( \frac{\partial \rho^l}{\partial T} \right) \quad (1.2a)$$

$$\beta_{w_i^l} = -\frac{1}{\rho_0^l} \left( \frac{\partial \rho^l}{\partial w_i^l} \right) \quad (1.2b)$$

The linear fit assumes also that the density takes a reference value,  $\rho_0^l$ , when temperature and liquid composition reach reference values, respectively  $T_0$  and  $\langle w_i \rangle_0^l$ , while the coefficients  $\beta_{w_i^l}$  remain constant. However, in some situations, a suitable thermodynamic database providing accurate density values is far better than a linear fit, especially in the current context of macrosegregation. Such possibility will be discussed later in the manuscript (cf. SECTION TODO)

In the presence of gravity, the density gradient in [eq. \(1.1b\)](#), causes thermosolutal convection in the liquid bulk and a subsequent macrosegregation.

### Solidification shrinkage

Solid alloys generally have a greater density than the liquid phase ( $\rho^s > \rho^l$ ), thus occupy less volume, with the exception of silicon where the opposite is true. Upon solidification, the liquid moves towards the solidification front to compensate for the volume difference caused by the phase change, as well as the thermal contraction. When macrosegregation is triggered by solidification shrinkage, we speak of *inverse segregation*: while one would naturally expect negative macrosegregation in areas where solidification begins and positive inside the alloy, shrinkage promotes the opposite phenomenon, by bringing solute-richer liquid towards the solidifying areas, thus raising their solute content, and resulting in a positively segregated solid. In contrast to liquid convection, shrinkage flow may cause macrosegregation even without gravity.

### Movement of equiaxed grains

Equiaxed grains can grow in the liquid bulk where thermal gradients are weak, or in the presence of inoculants. Consequently, they are transported by the flow (floating or sedimenting, depending on their density [[Beckermann 2002](#)]) which leads to negative macrosegregation in their final position.

### Solid deformation

Stresses of thermal and mechanical nature are always found in casting processes (e.g. bulging between rolls in continuous casting). Deformation of the semi-solid in the mushy zone causes a relative solid-liquid flow in the inward (tensile stresses) or outward (compressive stresses) direction, causing macrosegregation.

#### 1.2.2 Examples

##### In continuous casting

The partially solidified slab is carried through a series of rolls that exert contact forces to straighten it. As the mushy part of a slab enters through these rolls, interdendritic liquid is expelled backwards, i.e. regions with lower solid fraction. Since the boundaries solidify earlier than the centre, the enriched liquid accumulates halfway in thickness, forming a centreline macrosegregation as shown in [fig. 1.4](#). Other types of segregates (channels, A-segregates ...) can also be found but remain more specific to ingot casting.

## Chapter 1. General Introduction

---

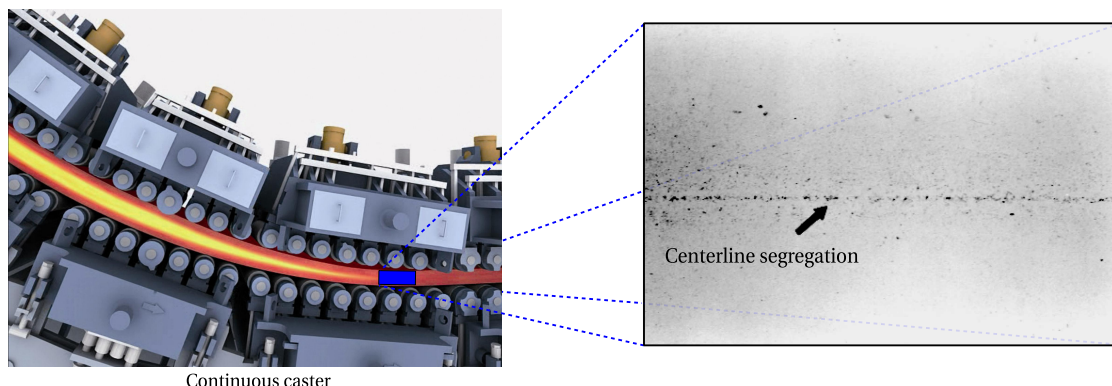


**Fig. 1.4 – Centreline segregation in a steel slab [Beckermann 2002]**

### In ingot casting

A variety of segregation patterns can be encountered in heavy ingots:

- the lower part is characterized by a negative segregation cone promoted by the sedimentation of equiaxed crystals,
- positive segregation channels, known as A-segregates, form along the columnar dendritic zones, close to the vertical contact with the mould,
- positive V-segregates can be identified in the centre of the ingot,
- a positive macrosegregation in the upper zone where the last liquid solidifies, the so-called "hot-top", caused by solidification shrinkage (inverse segregation) and thermosolutal buoyancy forces.

Combeau et al. [2009] state that A-segregates and V-segregates formation is mainly attributed to local flow phenomena. As such, their scale is finer than macrosegregation, hence called "mesosegregates".

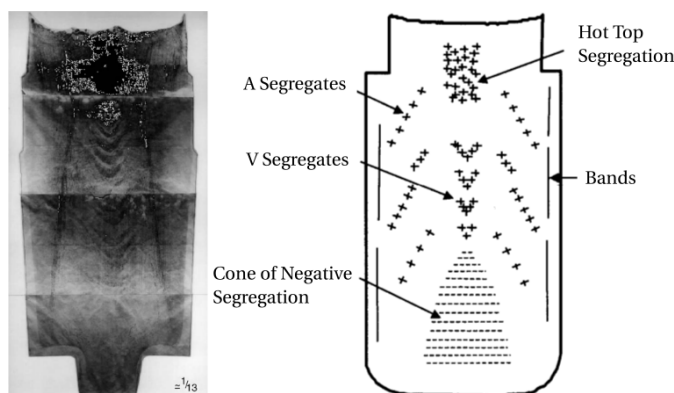


**Fig. 1.5 – Sulphur print (left) of a 65-ton steel ingot [Lesoult 2005] showing various patterns (right) of macrosegregation [Flemings 1974]**

### In investment casting

This process is widely used to cast single-crystal (SC) alloys for turbines and other applications that require excellent mechanical behavior [Giamei et al. 1970]. When performed by directional solidification, thermosolutal forces thrust segregated species outside of the mushy zone into the liquid bulk. The segregation scale ranges from a few dendrites to a few hundreds of them, hence forming "long and narrow trails" (fig. 1.6a) as described by Felicelli et al. [1991]. Freckles are frequently formed by small equiaxed grains (fig. 1.6b), probably caused by a uniform temperature gradient that settles as the channels become richer in solute. They can be observed on the ingot's surface, as well as in the volume.

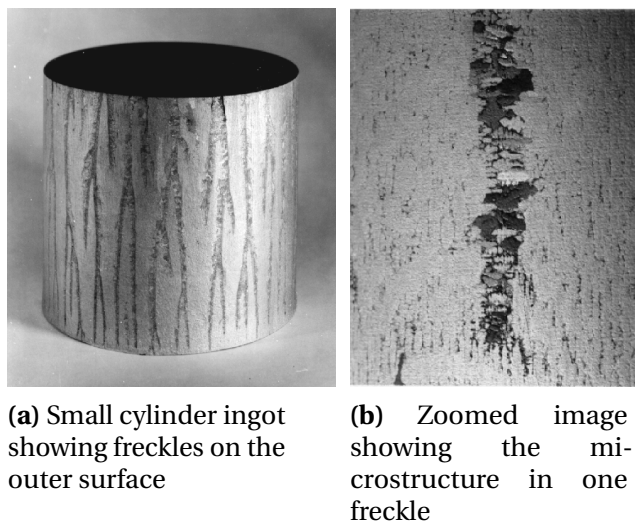


**Fig. 1.6** – Freckles in directional casting of nickel-base superalloys

## 1.3 Industrial Worries

**Steel production** has continuously increased over the years to meet the industrial needs. Figure 1.7 shows this increase between 1980 and 2013 with a clear dominance of the Chinese production. Quality constraints have also increased where specific grades of steel are needed in critical applications such as mega-structures in construction and heavy machinery. Therefore, alloys with defects are considered vulnerable and should be avoided as much as possible during the casting process. As such, steelmakers have been investing in research, with the aim of understanding better the phenomena leading to casting problems, and improve the processes when possible.

**Simulation software** dedicated to alloy casting is one of the main research investments undertaken by steelmakers. These tools coming from academic research are actively used to optimize the process. However, few are the tools that take into account

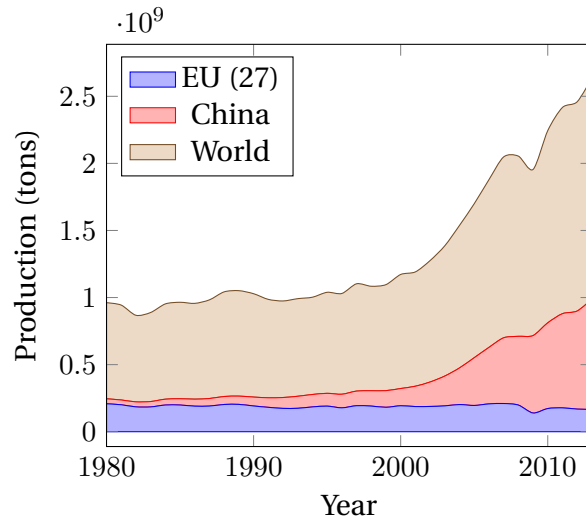


**Fig. 1.7** – Evolution curves of crude steel worldwide production from 1980 to 2013 [WSA 2014].

the casting environment. For instance, the continuous casting process, in [fig. 1.1](#), is a chain process where the last steps involve rolls, water sprays and other components. A dedicated software is one that can provide the geometric requirements with suitable meshing capabilities, as well as respond to metallurgical and mechanical requirements, mainly:

- handling moulds and their interaction with the alloy (thermal resistances ...)
- handling alloy filling and predicting velocity in the liquid and mushy zone
- handling thermomechanical stresses in the solid
- handling multicomponent alloys and predicting macrosegregation
- handling finite solute diffusion in solid phases
- handling real alloy properties (not just constant thermophysical/thermomechanical properties)

## 1.4 Project context and objectives

### 1.4.1 Context

The European Space Agency (ESA) has been actively committed, since its foundation in 1975, in the research field. Its covers not only exclusive space applications, but also fundamental science like solidification. This thesis takes part of the ESA project entitled *CCEMLCC*, abbreviating "Chill Cooling for the Electro-Magnetic Levitator in relation with Continuous Casting of steel". The three-year contract from 2011 to late 2014 denoted *CCEMLCC II*, was preceded by an initial project phase, *CCEMLCC*

I, from 2007 to 2009. The main focus is studying containerless solidification of steel under microgravity conditions. A chill plate is later used to extract heat from the alloy, simulating the contact effect with a mould in continuous casting or ingot casting. A partnership of 7 industrial and academic entities was formed in *CCEMLCC II*. Here is a brief summary of each partner's commitment:

### Academic partners

- CEMEF (France): numerical modelling of microgravity chill cooling experiments
- DLR (German Aerospace Centre) and RUB university (Germany): preparation of a chill cooling device for electromagnetic levitation (EML), microgravity testing and investigation of growth kinetics in chill-cooled and undercooled steel alloys
- University of Alberta (Canada): impulse atomization of the D2 tool steel
- University of Bremen - IWT institute (Germany): study of melt solidification in atomization processing

### Industrial partners

- ARCELORMITTAL (France): elaboration of a series of steel grades used in microgravity and ground studies
- METSO Minerals Inc. (Finland): material production with D2 tool steel for spray forming
- TRANSVALOR (France): development and marketing of casting simulation software *Thercast<sup>®</sup>*

CEMEF, as an academic partner, contributed to the work by proposing numerical models in view of predicting the chill cooling of steel droplets. A first model was developed by [Rivaux \[2011\]](#) whereas the present thesis discusses a new model. The experimental work considered various facilities and environments to set a droplet of molten alloy in levitation: EML ([fig. 1.8](#)) for ground-based experiments, microgravity in parabolic flight or sounding rockets and last, microgravity condition on-board the International Space Station (ISS)

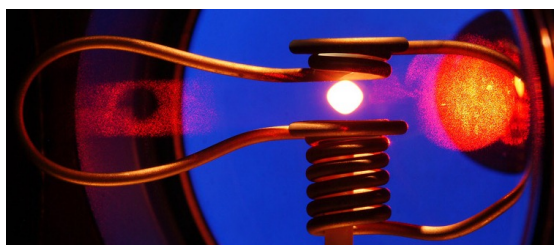


**Fig. 1.8 – Electromagnetic levitation [[DLR 2014](#)].**

### 1.4.2 Objectives and outline

The main focus of the present thesis is predicting macrosegregation with liquid dynamics assuming a fixed solid phase, i.e. no account of solid transport (e.g. equiaxed crystals sedimentation) and no account of solid deformation. In CEMEF, this scope has been adopted for previous work by Gouttebroze [2005], Liu [2005], Mosbah [2008], Rivaux [2011], and Carozzani [2012]. Nevertheless, many modelling features evolved with time such as going from two-dimensional to three-dimensional modelling, resolution schemes for each of the conservation equations: energy, chemical species and liquid momentum, Eulerian or Lagrangian descriptions, modelling of grain structure and others. In this thesis, we propose a numerical model that takes into account i) the energy conservation in a temperature formulation based on a thermodynamic database mapping, ii) the liquid momentum conservation with thermosolutal convection and solidification shrinkage as driving forces, iii) solute mass conservation and iv) solidification paths at full equilibrium for multicomponent alloys microsegregation. Moreover, all equations are formulated in a pure Eulerian description while using the Level Set method to keep implicitly track of the interface between the alloy and surrounding gas. To the author's knowledge, this work combining macrosegregation prediction using the level set methodology to track the metal-air interface during shrinkage has no precedent in casting and solidification literature. The model couples in a weak fashion, all four conservation equations presented in fig. 1.9, showing on the one hand, that microsegregation is an essential common link between these equations, while on the other hand, the level set interacts with conservations equations by giving the interface position.

Numerical tools: Cimlib relying on PETSc, parallelised with MPICH2, paraview and python as tools for postprocess and analysis.

The previously mentionned simulation requirements are not met in a single casting software package. Nevertheless, *Thercast*® is a promising tool that already handles a part of the above points. The current thesis developments are done using C++ language as a part of the in-house code, known as *CimLib* [Digonnet et al. 2007; Mesri et al. 2009]. This fully parallel library is the main academic research support for *Thercast*®.

Outline: each chapter content ...

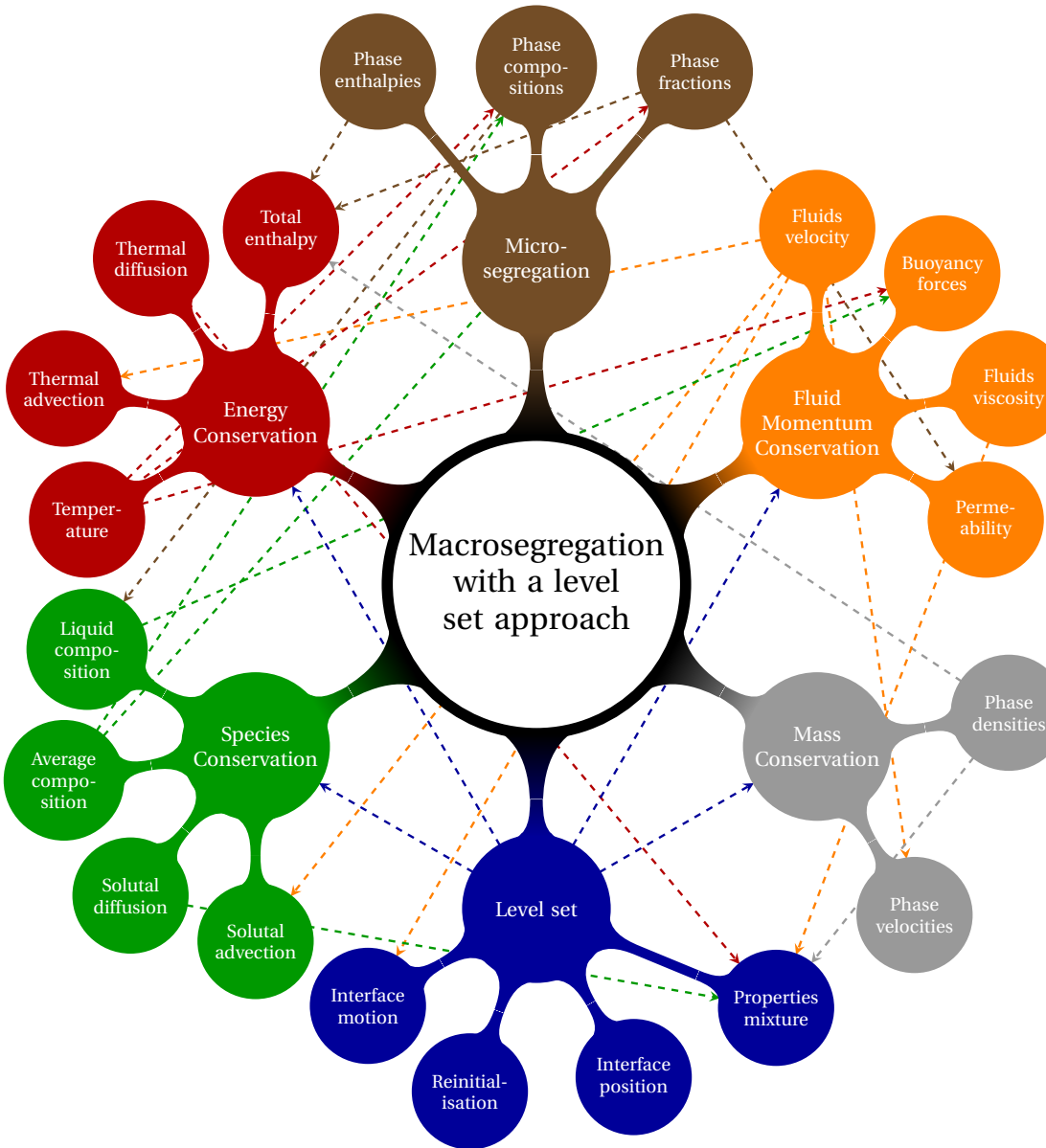


**Fig. 1.9** – A graphical representation of the main ingredients of the numerical approach, for a macrosegregation model with the level set methodology, when no solid deformation or movement are considered. The dashed lines represent the possible interaction between the components.

## **Chapter 1. General Introduction**

---

# Chapter 2

## Modelling Review

### Contents

---

<b>2.1 Modelling macrosegregation . . . . .</b>	<b>14</b>
2.1.1 Dendritic growth . . . . .	14
2.1.2 Mush permeability . . . . .	14
2.1.3 Microsegregation . . . . .	16
2.1.4 Macroscopic solidification model: monodomain . . . . .	18
<b>2.2 Eulerian and Lagrangian motion description . . . . .</b>	<b>24</b>
2.2.1 Overview . . . . .	24
2.2.2 Interface capturing . . . . .	26
<b>2.3 Solidification models with level set . . . . .</b>	<b>26</b>
<b>2.4 The level set method . . . . .</b>	<b>27</b>
2.4.1 Diffuse interface . . . . .	28
2.4.2 Mixing Laws . . . . .	29
<b>2.5 Interface motion . . . . .</b>	<b>31</b>
2.5.1 Level set transport . . . . .	32
2.5.2 Level set regularisation . . . . .	33

---

## 2.1 Modelling macrosegregation

### 2.1.1 Dendritic growth

In a casting process, the chill surface i.e. the contact between the molten alloy and relatively cold moulds, is the first area to solidify. Thermal gradient,  $G$ , and cooling rate  $R$  are two crucial process parameters that define the solid-liquid interface velocity  $\bar{v}^*$ , which in turn, affects the initial microstructure. Although it may be not easy to control them, it remains important to understand their implication in solidification.

The solid-liquid interface fluctuates when solidifying, thus perturbations may appear on the front, locally destabilizing it. Two outcome scenarios are possible. The first scenario is characterized by low values of  $\bar{v}^*$  where the interface maintains a planar shape, hence we speak of *planar growth*. With this kind of growth, a random protuberance appearing at the interface, has a low tip velocity (low driving force of solidification). As such, the rest of the interface catches up, keeping the planar geometry. In another scenario, where a real casting is considered, the interface speed is greater in general, due to high solidification rate. The protuberance tip will be pulled into a liquid less rich in solute than the interface. The zone ahead of the solid-liquid interface is constitutionally undercooled [Tiller et al. 1953], giving a greater driving force for the protuberance to grow in the direction of the thermal gradient. As it has a tree-like shape, we speak of *dendritic growth*. Near the chill surface, dendrites are columnar, with a favourable growth in the  $<100>$  direction for alloys with cubic lattices, but different orientations are also reported in the literature [see Dantzig et al. 2009, p. 289]. If temperature is uniform, which is the case usually far from mould walls, a similar dendritic growth phenomenon occurs, but with an equiaxed morphology.

Columnar dendrites are characterized by a primary spacing,  $\lambda_1$ , between the main trunks, and a secondary spacing,  $\lambda_2$ , for the arms that are perpendicular to the trunks. It should be noted that  $\lambda_1$  and  $\lambda_2$ , together with the grain size, are three important microstructural parameters in the as-cast microstructure [Easton et al. 2011]. Further branching may occur but will not be discussed here.

### 2.1.2 Mush permeability

The dendritic geometry is crucial in solidification theory as it exhibits lower solid fraction compared to a microstructure formed by planar growth. This fact has consequences on the fluid-structure interaction in the mushy zone, namely the liquid flow through dendrites. At the chill surface, the solid grows gradually from dispersed growing nuclei to a permeable solid skeleton, until finally grains have fully grown at the end of phase change. In the intermediate state, the liquid flow in and out of the mushy zone through the dendrites is a key phenomenon from a rheological perspective. The flow through the solid skeleton is damped by primary and secondary dendrites, result-

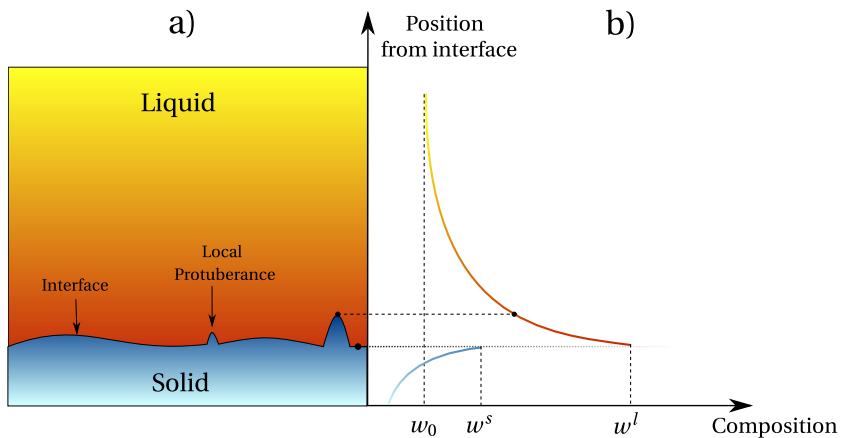


**Fig. 2.1** – Schematic of a) a protuberance growing on the solid-liquid interface with b) the corresponding composition profiles (Reproduced and adapted from DoITPoMS [2000], © DoITPoMS, University of Cambridge).

ing in momentum dissipation just like in saturated porous media. The famous [Darcy \[1856\]](#) law relates the pressure gradient ( $\vec{\nabla}p$ ) to the fluid velocity  $\vec{v}$  (assuming a the solid phase is fixed), through the following equation [[Rappaz et al. 2003](#)]:

$$\vec{v} = \frac{\mathbb{K}}{\mu^l} \vec{\nabla}p \quad (2.1)$$

where  $\mu^l$  is the liquid dynamic viscosity and  $\mathbb{K}$  is the permeability tensor. The latter parameter has been the subject of numerous studies that aimed to predict it from various microstructural or morphological parameters. Some of these studies have started even before the first attempts to model macrosegregation by [Flemings et al. \[1967\]](#), [Flemings et al. \[1968a\]](#), and [Flemings et al. \[1968b\]](#). Basically, all models include the solid fraction,  $g^s$ , as input to predict mush permeability along with empirical data. An instance of such models is the work of [Xu et al. \[1991\]](#). Some models rely additionally on the primary dendrite arm spacing  $\lambda_1$  like Blake-Kozeny [[Ramirez et al. 2003](#)], or the secondary dendrite arm spacing  $\lambda_2$  like Carman-Kozeny, as a meaningful parameter to determine an isotropic permeability. Other models like [Poirier \[1987\]](#) and [Felicelli et al. \[1991\]](#) derive an anisotropic permeability based on both  $\lambda_1$  and  $\lambda_2$ .

The present work uses Carman-Kozeny as a constitutive model for the isotropic permeability scalar (zero order tensor):

$$\mathbb{K} = \frac{\lambda_2^2 g^l{}^3}{180 (1 - g^l)^2} \quad (2.2)$$

### 2.1.3 Microsegregation

Microsegregation is a fundamental phenomenon in solidification. The simplest definition is an uneven distribution of solute between the liquid and the herein growing solid, at the microscopic scale of the interface separating these phases. If we consider a binary alloy, then the solubility limit is the key factor that dictates the composition at which a primary solid phase exists in equilibrium. The segregation (or partition) coefficient  $k$  determines the extent of solute rejection into the liquid during solidification:

$$k = \frac{w^s}{w^l} \quad (2.3)$$

where  $w^s$  and  $w^l$  are the compositions of the solid and liquid respectively, at the interface. When the segregation coefficient is less than unity (such is the case for most alloys during dendritic solidification), the first solid forms with a composition  $w^s = kw^l = kw_0$  less than the liquid's composition  $w_0$ , the latter being initially at the nominal composition,  $w_0$ . Figure 2.2 illustrates a typical binary phase diagram where the real solidus and liquidus are represented by solid lines, while the corresponding linear approximations are in grey dashed lines. For most binary alloys, this linearisation simplifies derivation of microsegregation models, as  $k$  becomes independent of temperature.

For each phase, the relationship between the composition at the interface and that in the bulk depends on the chemical homogenisation ability of the phase. The more homogeneous a phase, the closer the concentrations between the interface and the bulk, hence closer to equilibrium. It is thus essential to study the effect of homogenisation on the segregation behaviour and the subsequent effect on solidification, which leads the formalism of microsegregation models.

### Microsegregation models

Solid formation depends greatly on the ability of chemicals species to diffuse within each of the solid and liquid phases, but also across the solid-liquid interface. Furthermore, chemical diffusion like all other diffusional processes, is a time-dependent phenomenon. One can thus conclude that two factors influence the amount of solid formation: cooling rate and diffusion coefficients. However, convection and other mechanical mixing sources, homogenise the composition much faster than atomic diffusion. As such, *complete mixing* in the liquid is always an acceptable assumption, regardless of the solidification time. We may speak of infinite diffusion in the liquid. Nevertheless, diffusion in the solid, also known as *back diffusion*, is the only transport mechanism with very low diffusion coefficients. Therefore, chemical species require a long time, i.e. low cooling rate, to completely diffuse within the solid. The difference

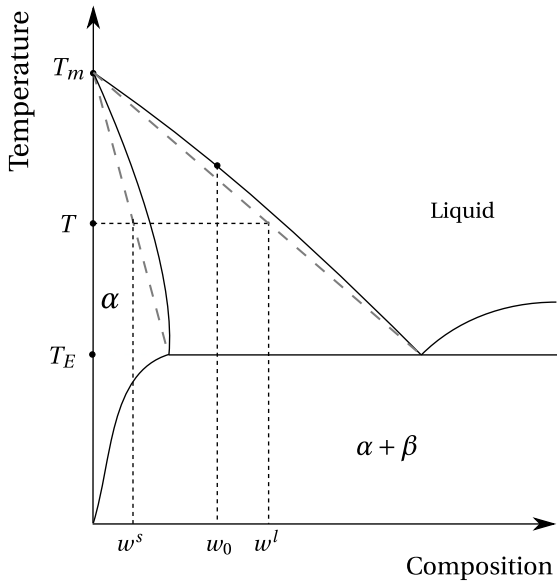


**Fig. 2.2** – Typical eutectic phase diagram of a binary alloy showing the real solidus and liquidus at full equilibrium, with the corresponding linear approximations (grey dashed lines).  $T_m$  and  $T_E$  are respectively the melting point of the solvent and the eutectic temperature.

in diffusional behaviour at the scale of a secondary dendrite arm, is summarized by two limiting segregation models of perfect equilibrium and nonequilibrium, which are the lever rule and Gulliver-Scheil models, respectively. Afterwards, models with finite back diffusion are presented.

### Lever rule

The lever rule considers an ideal equilibrium in all phases, i.e. solidification is extremely slow, hence phase compositions are homogeneous ( $w^{l*} = w^l$  and  $w^{s*} = w^s$ ) at all times as a consequence of complete mixing. These compositions are given by:

$$w^l = w^{l*} = k^{-1}w^{s*} = k^{-1}w^s \quad (2.4)$$

$$w^s = w^{s*} = \frac{kw_0}{kf^s + (1 - f^s)} \quad (2.5)$$

At the end of solidification, the composition of the solid phase is equal to the nominal composition,  $w^s = w_0$

### Gulliver-Scheil

The other limiting case is the absence of diffusion in the solid. That includes also the diffusion at the interface, so nothing diffuses in or out. The consequence is a steady increase of the homogeneous liquid composition while the solid composition remains non-uniform. Compared to a full equilibrium approach, higher fractions of liquid will

remain until eutectic composition is reached, triggering a eutectic solidification. The phase compositions are given by:

$$w^l = w^{l*} = k^{-1}w^{s*} \quad (2.6)$$

$$w^{s*} = kw_0(1 - f^s)^{k-1} \quad (2.7)$$

### Finite back diffusion

It has been concluded that the assumption of a negligable back diffusion overestimates the liquid composition and the resulting eutectic fraction. Therefore, many models studied the limited diffusion in the solid. One of the earliest models is the Brody-Flemings models [Khan et al. 2014] that is a based on a differential solute balance equation for a parabolic growth rate, as follows:

$$w^l = w^{l*} = k^{-1}w^{s*} \quad (2.8)$$

$$w^{s*} = kw_0 [1 - (1 - 2\text{Fo}^s k) f^s]^{\frac{k-1}{1-2\text{Fo}^s k}} \quad (2.9)$$

where  $\text{Fo}^s$  is the dimensionless *Fourier number* for diffusion in the solid [Dantzig et al. 2009]. It depends on the solid diffusion coefficient  $D^s$ , solidification time  $t_s$  and the secondary dendrite arm spacing, as follows:

$$\text{Fo}^s = \frac{D^s t_s}{(\lambda_2/2)^2} \quad (2.10)$$

Several other models were since suggested and used. The interested reader is referred to the following non exhaustive list of publications: Clyne et al. [1981], Kobayashi [1988], Ni et al. [1991], Wang et al. [1993], Combeau et al. [1996], Martorano et al. [2003], and Tourret et al. [2009]. It is noted that some of these publications consider also a finite diffusion in the liquid phase.

#### 2.1.4 Macroscopic solidification model: monodomain

In this section, we will present the macroscopic conservations equations that enable us to predict macrosegregation in the metal when the latter is the only domain in the system.

#### Volume averaging

It is crucial for a solidification model to represent phenomena on the microscale, then scale up to predict macrscopic phenomena. Nevertheless, the characteristic length of a small scale in solidification may represent a dendrite arm spacing, for instance the mushy zone permeability, as it may also represent an atomic distance if one is

interested, for instance, in the growth competition between diffusion and surface energy of the solid-liquid interface. Modelling infinitely small-scale phenomena could be prohibitively expensive in computation time, if we target industrial scales.

The volume averaging is a technique that allows bypassing this barrier by averaging small-scale variations on a so-called *representative volume element* (RVE) [Dantzig et al. 2009] of volume  $V_E$ , with the following dimensional constraints: the element should be large enough to "see" and average microscopic fluctuations whilst being smaller than the scale of macroscopic variations. Solid and liquid may exist simultaneously in the RVE, but no gas phase is considered (volume saturation:  $V^s + V^l = V_E$ ). Moreover, temperature is assumed uniform and equal for all the phases. The formalism, introduced by Ni et al. [1991], is summarized by the following equations for any physical quantity  $\psi$ :

$$\langle \psi \rangle = \frac{1}{V_E} \int_{V_E} \psi \, d\Omega = \langle \psi^s \rangle + \langle \psi^l \rangle \quad (2.11)$$

where  $\langle \psi \rangle^s$  and  $\langle \psi \rangle^l$  are phase averages of  $\psi$ . Then, for any phase  $\phi$ , one can introduce the *phase intrinsic average* of  $\psi$ , denoted  $\langle \psi \rangle^\phi$ , by writing:

$$\langle \psi^\phi \rangle = \frac{1}{V_E} \int_{V^\phi} \psi \, d\Omega = g^\phi \langle \psi \rangle^\phi \quad (2.12)$$

where  $g^\phi$  is the volume fraction of phase  $\phi$  with  $g^\phi = V_\phi / V_E$ . To finalize, the averaging is applied to temporal and spatial derivation operators:

$$\langle \frac{\partial \psi^\phi}{\partial t} \rangle = \frac{\partial \langle \psi^\phi \rangle}{\partial t} - \int_{\Gamma^*} \psi^\phi \vec{v}^* \cdot \vec{n}^\phi \, dA \quad (2.13)$$

$$\langle \vec{\nabla} \psi^\phi \rangle = \vec{\nabla} \langle \psi^\phi \rangle + \int_{\Gamma^*} \psi^\phi \vec{n}^\phi \, dA \quad (2.14)$$

where  $\vec{v}^*$  is the local relative interface velocity and  $\Gamma^*$  is the solid-liquid interface, while  $\vec{n}^\phi$  is the normal to  $\Gamma^*$ , directed outwards. The surface integral terms in eqs. (2.13) and (2.14) are *interfacial averages* that express exchanges between the phases across the interface. The previous equations will be used to derive a set macroscopic conservation equations. It is noted that the intrinsic average  $\langle \psi \rangle^\phi$  may be replaced by  $\psi^\phi$  for notation simplicity, whenever the averaging technique applies.

## Macroscopic equations

A monodomain macroscopic model relies on four main conservation equations to predict macrosegregation in a single alloy, i.e. the latter is considered without any interaction with another alloy or ambient air. The general form of an averaged conser-

## Chapter 2. Modelling Review

---

vation equation of any physical quantity  $\psi$  is given by:

$$\frac{\partial \langle \psi \rangle}{\partial t} + \nabla \cdot \langle \psi \vec{v} \rangle + \nabla \cdot \langle \vec{j}_\psi \rangle = \langle Q_\psi \rangle \quad (2.15)$$

The first LHS term in eq. (2.15) represents the time variation of  $\psi$ , the second term accounts for transport by advection while the third is the diffusive transport and the RHS term represents a volume source. The considered equations are mass, energy, species conservation and momentum, all summarized in table 2.1. The latter equation is averaged only for the liquid phase, as we assume a fixed and rigid solid phase ( $\vec{v}^s = \vec{0}$ ), thus the corresponding equation vanishes. We develop the ingredients of these

**Table 2.1** – Summary of conservation equations with their variables.

Conservation Equation	$\psi$	$\vec{j}_\psi$	$Q_\psi$
Mass	$\rho$	—	—
Energy	$\rho h$	$\vec{q}$	—
Species	$\rho w_i$	$\vec{j}_i$	—
Liquid momentum	$\rho^l \vec{v}^l$	$-\overline{\sigma^l}$	$\vec{F}_v^l$

equations using the averaging technique, as follows:

$$\langle \rho \rangle = g^l \rho^l + g^s \rho^s \quad (2.16)$$

$$\langle \rho \vec{v} \rangle = g^l \rho^l \vec{v}^l + g^s \rho^s \vec{v}^s \quad (2.17)$$

$$\langle \rho h \rangle = g^l \rho^l h^l + g^s \rho^s h^s \quad (2.18)$$

$$\langle \rho h \vec{v} \rangle = g^l \rho^l h^l \vec{v}^l + g^s \rho^s h^s \vec{v}^s \quad (2.19)$$

$$\langle \rho w_i \rangle = g^l \rho^l w_i^l + g^s \rho^s w_i^s \quad (2.20)$$

$$\langle \rho w_i \vec{v} \rangle = g^l \rho^l w_i^l \vec{v}^l + g^s \rho^s w_i^s \vec{v}^s \quad (2.21)$$

$$\langle \rho^l \vec{v}^l \rangle = \langle \rho^l \vec{v}^l \rangle^l = g^l \rho^l \vec{v}^l \quad (2.22)$$

$$\langle \rho^l \vec{v}^l \times \vec{v} \rangle = g^l \rho^l \vec{v}^l \times \vec{v}^l + g^s \rho^s \vec{v}^l \times \vec{v}^s \quad (2.23)$$

Next, we define the average diffusive fluxes,  $\vec{q}$  for energy and  $\vec{j}_i$  for solutes, using Fourier's conduction law and Fick's first law, respectively [Rappaz et al. 2003]:

$$\langle \vec{q} \rangle = -g^l \langle \kappa^l \rangle \vec{\nabla} T - g^s \langle \kappa^s \rangle \vec{\nabla} T = -\langle \kappa \rangle \vec{\nabla} T \quad (2.24)$$

$$\langle \vec{j}_i \rangle = -g^l \rho^l D^l \vec{\nabla} w_i^l - g^s \rho^s D^s \vec{\nabla} w_i^s \quad (2.25)$$

In eq. (2.25), the macroscopic diffusion coefficient in the solid is neglected, by considering that for macroscopic scales, the average composition of the alloy is much more

influenced by advective and diffusive transport in the liquid. In eq. (2.24), we assume that phases are at thermal equilibrium, that is, temperature is uniform in the RVE.

Now that the main conservation equations ingredients are properly defined, we may write each averaged conservation equation as the sum of two local conservation equations for each phase in the RVE, hence introducing also interfacial average terms. For instance, the local mass balance in each phase is given by:

$$\frac{\partial}{\partial t} \left( g^l \rho^l \right) + \nabla \cdot \left( g^l \rho^l \vec{v}^l \right) = S_V \langle \rho^l \vec{v}^{l*} \cdot \vec{n} \rangle^* - S_V \langle \rho^l \vec{v}^* \cdot \vec{n} \rangle^* \quad (2.26a)$$

$$\frac{\partial}{\partial t} \left( g^s \rho^s \right) + \nabla \cdot \left( g^s \rho^s \vec{v}^s \right) = -S_V \langle \rho^s \vec{v}^{s*} \cdot \vec{n} \rangle^* + S_V \langle \rho^s \vec{v}^* \cdot \vec{n} \rangle^* \quad (2.26b)$$

where  $S_V = A_{sl}/V_E$  is the specific surface area,  $\vec{v}^{l*}$  and  $\vec{v}^{s*}$  are respectively, the liquid and solid phase velocity at the interface and  $\vec{v}^*$  is the previously introduced solid-liquid interface velocity. For instance, the first interfacial exchange term in the RHS of eq. (2.26a) is expanded as follows [Dantzig et al. 2009]:

$$S_V \langle \rho^l \vec{v}^{l*} \cdot \vec{n} \rangle^* = \frac{A_{sl}}{V_E} \left( \frac{1}{A_{sl}} \int_{A_{sl}} \rho^l \vec{v}^{l*} \cdot \vec{n} \, dA \right) \quad (2.27a)$$

$$= \frac{1}{V_E} \int_{A_{sl}} \rho^l \vec{v}^{l*} \cdot \vec{n} \, dA \quad (2.27b)$$

Summing equations (2.26a) and (2.26b), results in the overall mass balance in the RVE:

$$\begin{aligned} \frac{\partial}{\partial t} \left( g^l \rho^l + g^s \rho^s \right) + \nabla \cdot \left( g^l \rho^l \vec{v}^l + g^s \rho^s \vec{v}^s \right) = \\ S_V \langle \rho^l \left( \vec{v}^{l*} - \vec{v}^* \right) \cdot \vec{n} \rangle^* - S_V \langle \rho^s \left( \vec{v}^{s*} - \vec{v}^* \right) \cdot \vec{n} \rangle^* \end{aligned} \quad (2.28)$$

where the RHS cancels to zero as shown by Ni et al. [1991]. Moreover, the authors show that with their averaging technique, interfacial exchanges for energy, chemical species and momentum cancel out as they are equal in absolute value but opposite in sign. Using eqs. (2.16) to (2.25) and following the same procedure done in eq. (2.28), the averaged mass balance hence writes:

$$\frac{\partial \langle \rho \rangle}{\partial t} + \nabla \cdot \langle \rho \vec{v} \rangle = 0 \quad (2.29)$$

whereas the averaged energy balance writes:

$$\frac{\partial \langle \rho h \rangle}{\partial t} + \nabla \cdot \langle \rho h \vec{v} \rangle - \nabla \cdot \left( \langle \kappa \rangle \vec{\nabla} T \right) = 0 \quad (2.30)$$

and finally the species balance writes:

$$\frac{\partial \langle \rho w_i \rangle}{\partial t} + \nabla \cdot \langle \rho w_i \vec{v} \rangle - \nabla \cdot \left( g^l \rho^l D^l \vec{\nabla} w_i^l \right) = 0 \quad (2.31)$$

As stated previously, the momentum balance in the solid phase is not taken into consideration, hence we do not sum the corresponding local conservation equations. This has consequences on the advection terms in energy and species conservation, and later on we will show the consequences on the momentum conservation in the liquid. First, the advection terms in [eqs. \(2.30\)](#) and [\(2.31\)](#) shall be redefined by considering that the fluid is incompressible ( $\nabla \cdot \langle \vec{v}^l \rangle = 0$ ), which yields:

$$\nabla \cdot \langle \rho h \vec{v} \rangle = \langle \vec{v}^l \rangle \cdot \vec{\nabla} \left( \rho^l h^l \right) \quad (2.32)$$

$$\nabla \cdot \langle \rho w_i \vec{v} \rangle = \langle \vec{v}^l \rangle \cdot \vec{\nabla} \left( \rho^l w_i^l \right) \quad (2.33)$$

As for the liquid momentum balance, we write:

$$\frac{\partial}{\partial t} \left( \rho^l g^l \vec{v}^l \right) + \vec{\nabla} \cdot \left( \rho^l g^l \vec{v}^l \times \vec{v}^l \right) = \vec{\nabla} \cdot \left( g^l \bar{\sigma}^l \right) + g^l \vec{F}_v^l + \vec{\Gamma}^l \quad (2.34)$$

where  $\vec{F}_v^l$  is the vector of external body forces exerted on the liquid phase. In our case, it accounts for the fluid's weight:

$$\vec{F}_v^l = \rho^l \vec{g} \quad (2.35)$$

The interfacial momentum transfer between the solid and liquid phases in [eq. \(2.34\)](#) is modelled by a momentum flux vector  $\vec{\Gamma}^l$ , consisting of hydrostatic and deviatoric parts, such that:

$$\vec{\Gamma}^l = \vec{\Gamma}_p^l + \vec{\Gamma}_{\mathbb{S}}^l \quad (2.36)$$

$$\vec{\Gamma}_p^l = p^{l*} \vec{\nabla} g^l = p^l \vec{\nabla} g^l \quad (2.37)$$

$$\vec{\Gamma}_{\mathbb{S}}^l = -g^{l2} \mu^l \mathbb{K}^{-1} \left( \vec{v}^l - \vec{x}^s \right) \quad (2.38)$$

where  $p^{l*}$  is the pressure at the interface, considered to be equal to the liquid hydrostatic pressure  $p^l$ ,  $\mathbb{K}$  is a permeability scalar (isotropic) computed using [eq. \(2.1\)](#) and  $\mu^l$  is the liquid's dynamic viscosity. The general form of the Cauchy liquid stress tensor in [eq. \(2.34\)](#) is decomposed as follows:

$$\langle \bar{\sigma}^l \rangle = g^l \bar{\sigma}^l = - \left( \langle p^l \rangle - \lambda \nabla \cdot \langle \vec{v}^l \rangle \right) \bar{\mathbb{I}} + \langle \bar{\mathbb{S}}^l \rangle \quad (2.39)$$

where  $\lambda$  is a dilatational viscosity [[Dantzig et al. 2009](#)] and  $\bar{\mathbb{S}}^l$  is the liquid strain deviator tensor. In the literature, the coefficient  $\lambda$  is taken proportional to the viscosity:  $\lambda = \frac{2}{3} \mu^l$ .

However, as we consider an incompressible flow, the divergence term vanishes, thus rewriting eq. (2.39) as follows:

$$\langle \bar{\bar{\sigma}}^l \rangle = -\langle p^l \rangle \bar{\bar{I}} + \langle \bar{\bar{S}}^l \rangle \quad (2.40a)$$

$$\langle \bar{\bar{\sigma}}^l \rangle = -\langle p^l \rangle \bar{\bar{I}} + 2\mu^l \langle \bar{\dot{\varepsilon}}^l \rangle \quad (2.40b)$$

where the transition from eq. (2.40a) to eq. (2.40b) is made possible by assuming a Newtonian behaviour for the liquid phase. The strain rate tensor,  $\langle \bar{\dot{\varepsilon}}^l \rangle$ , depends on the average liquid velocity:

$$\langle \bar{\dot{\varepsilon}}^l \rangle = \frac{1}{2} \left( \bar{\nabla} \langle \vec{v}^l \rangle + \bar{\nabla}^t \langle \vec{v}^l \rangle \right) \quad (2.41)$$

Finally, we obtain the final form of momentum conservation in the liquid phase coupled with the averaged mass balance, by injecting eqs. (2.35), (2.37), (2.38), (2.40b) and (2.41) in eq. (2.34):

$$\begin{aligned} \frac{\partial}{\partial t} \left( \rho^l \langle \vec{v}^l \rangle \right) + \frac{1}{g^l} \vec{\nabla} \cdot \left( \rho^l \langle \vec{v}^l \rangle \times \langle \vec{v}^l \rangle \right) = \\ - g^l \vec{\nabla} p^l - 2\mu^l \vec{\nabla} \cdot \left( \bar{\nabla} \langle \vec{v}^l \rangle + \bar{\nabla}^t \langle \vec{v}^l \rangle \right) - g^l \mu^l \mathbb{K}^{-1} \langle \vec{v}^l \rangle + g^l \rho^l \vec{g} \end{aligned} \quad (2.42)$$

where we intentionally employed the *superficial velocity*,  $\langle \vec{v}^l \rangle = g^l \vec{v}^l$ , as the main unknown, together with the liquid pressure  $p^l$ . This system, when modelled in 3D, has a total of 4 unknowns (velocity vector and pressure) and 3 equations ( $X, Y$  and  $Z$  projections for the velocity vector). A fourth equation provided by the mass balance (eq. (2.29)) is therefore added for closure, giving the following system of equations :

$$\left\{ \begin{array}{l} \frac{\partial}{\partial t} \left( \rho^l \langle \vec{v}^l \rangle \right) + \frac{1}{g^l} \vec{\nabla} \cdot \left( \rho^l \langle \vec{v}^l \rangle \times \langle \vec{v}^l \rangle \right) = \\ - g^l \vec{\nabla} p^l - 2\mu^l \vec{\nabla} \cdot \left( \bar{\nabla} \langle \vec{v}^l \rangle + \bar{\nabla}^t \langle \vec{v}^l \rangle \right) - g^l \mu^l \mathbb{K}^{-1} \langle \vec{v}^l \rangle + g^l \rho^l \vec{g} \\ \nabla \cdot \langle \vec{v}^l \rangle = 0 \end{array} \right. \quad (2.43)$$

Last, the Boussinesq approximation allows taking a constant density in the inertial terms of eq. (2.43) while the variations responsible for buoyancy forces can be computed using eq. (1.1a), if the system is incompressible. Hence, the final set of equations is better known as the incompressible *Navier-Stokes* equations, applied to a solidifying

melt:

$$\left\{ \begin{array}{l} \rho_0^l \left( \frac{\partial \langle \vec{v}^l \rangle}{\partial t} + \frac{1}{g^l} \vec{\nabla} \cdot (\langle \vec{v}^l \rangle \times \langle \vec{v}^l \rangle) \right) = \\ - g^l \vec{\nabla} p^l - 2\mu^l \vec{\nabla} \cdot (\overline{\nabla} \langle \vec{v}^l \rangle + \overline{\nabla}^t \langle \vec{v}^l \rangle) - g^l \mu^l \mathbb{K}^{-1} \langle \vec{v}^l \rangle + g^l \rho^l \vec{g} \\ \nabla \cdot \langle \vec{v}^l \rangle = 0 \end{array} \right. \quad (2.44)$$

Since all conservation equations were presented and simplified by the main assumption of a static solid phase, we may include them in a graphical summary in [section 2.1.4](#).

\* Macro models: Rivaux ? Gu beckermann 1999 ?

\* Micro macro: Tommy Carozzani2013, guo beckermann 2003, Combeau 2009, Miha Zaloznik 2010 (indirect), P. Thévoz, J.-L. Desbiolles, M. Rappaz, Metallurgical and Materials TransactionsA 20 (2) (1989) 311–322

\* end by talking about taking air into account and the need for an interface capturing method

## 2.2 Eulerian and Lagrangian motion description

### 2.2.1 Overview

In mechanics, it is possible to describe motion using two well-known motion description: Eulerian and Lagrangian descriptions. To start with the latter, it describes the motion of a particle by attributing a reference frame that moves with the particle. In other words, the particle itself is the center of a reference frame moving at the same speed during time. The position vector, denoted by  $\vec{x}$ , is hence updated as follows:

$$\vec{x}^{(t+1)} = \vec{x}^{(t)} + \vec{v} \Delta t \quad (2.48)$$

As such, the total variation of any physical quantity  $\psi$  related to the particle can be found by deriving with respect to time,  $\frac{d\psi}{dt}$ . In contrast to the Lagrangian description, the Eulerian description considers a fixed reference frame and independent of the particle's trajectory. The total variation of  $\psi$  cannot be simply described by a temporal derivative, since the particle's velocity is not known to the reference frame, and thus the velocity effect, namely the advective transport of  $\psi$ , should also be considered as follows:

$$\frac{d\psi}{dt} = \frac{\partial \psi}{\partial t} + \underbrace{\vec{v} \cdot \vec{\nabla} \psi}_{\text{Advection Transport}} \quad (2.49)$$

In this case, the LHS term is also known as *total* or *material derivative*. The importance of these motion descriptions is essential to solve mechanics, whether for fluids or

## 2.2. Eulerian and Lagrangian motion description

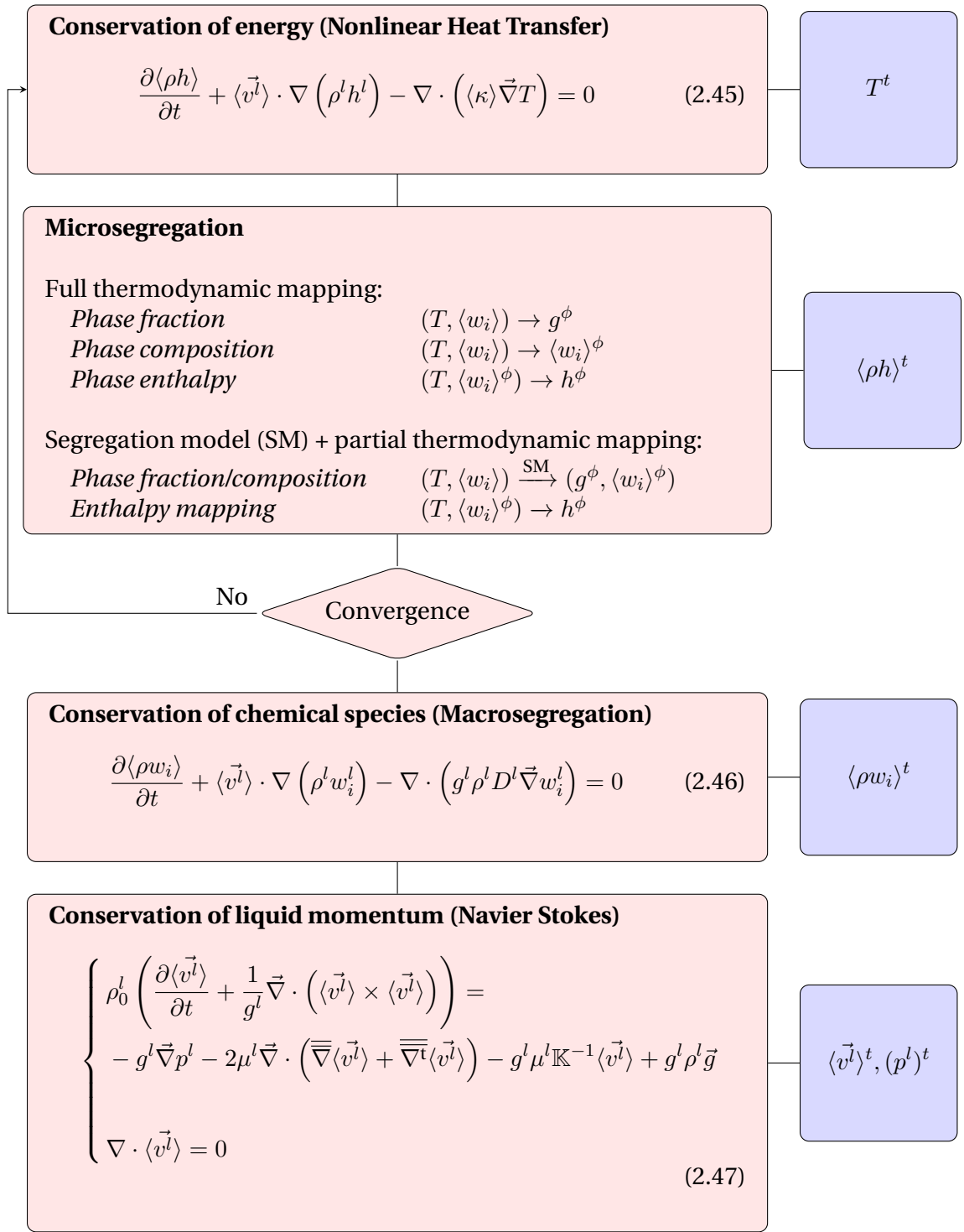


**Fig. 2.3** – Graphical resolution algorithm of the conservation equations used in a monodomain macroscopic model to predict macrosegregation for a time increment  $t$ . The blue boxes represent the output of each equation.

solids, using a numerical method like the finite element method (FEM). One of the main steps of this method is to spatially discretise a continuum into a grid of points (nodes, vertices ...), where any physical field shall be accordingly discretised. Now, if we focus on a node where velocity has a non zero value and following the previously made analysis, two outcomes are possible: either the node would be fixed (Eulerian) or it would move by a distance proportional to the prescribed velocity (Lagrangian). In the latter case, points located on the boundaries constantly require an update of the imposed boundary conditions.

From these explanations, one can deduce that an Eulerian framework is suited for fluid mechanics problems where velocities are high and may distort the mesh points, whereas the Lagrangian framework is better suited for solid mechanics problems where deformation velocities are relatively low and should well behave when predicting strains.

Another motion description has emerged some decades ago, [Hirt \[1971\]](#) call it the Arbitrary Langrangian-Eulerian (ALE) method. ALE combines advantages from both previous descriptions as it dictates a Lagrangian behaviour at "solid" nodes where solid is deforming, and an Eulerian behaviour at "fluid" nodes.

### 2.2.2 Interface capturing

As no solid deformation is considered in this work, the Eulerian framework is a convenient choice. Solidification shrinkage is to be considered in our current scope, so it will deform the alloy's outer surface in contact with the air. We intend to track this interface and its motion over time via a numerical method. A wide variety of methods accomplish this task while they yield different advantages and disadvantages. Such methods fall into two main classes, either interface tracking or interface capturing, among which we cite: marker-and-cell (MAC) [[Harlow et al. 1965](#)], volume of fluid (VOF) [[Hirt et al. 1981](#)], phase field methods (PF), level set method (LSM) [[Osher et al. 1988](#)], coupled level set - VOF method and others. The interested reader may refer to quick references by [Prosperetti \[2002\]](#) and [Maitre \[2006\]](#) about these methods.

In the past years, the level set method received a considerable attention in many computational fields, specifically in solidification. For this reason, we will focus on this method henceforth, giving a brief literature review and technical details in the next sections.

## 2.3 Solidification models with level set

In classic solidification problems, the need to track an interface occurs usually at the solid-liquid interface, that is why the phase field method [[Karma et al. 1996; Boettinger et al. 2002](#)] and the level set method [[Chen et al. 1997; Gibou et al. 2003; Tan et al.](#)

2007] were applied at a microscale to follow mainly the dendritic growth of a single crystal in an undercooled melt. In our case however, when we mention "solidification models using LSM", we do not mean the solid-liquid interface inside the alloy, but it is the alloy(liquid)-air interface that we intend to track, assuming that microscale phenomena between the phases within the alloy, are averaged using the previously defined technique in section 2.1.4.

Very few models were found in the literature, combining solidification and level set as stated previously. Du et al. [2001] applied it to track the interface between two molten alloys in a double casting technique. Welding research, on another hand, has been more active adapting the level set methodology to corresponding applications. In CEMEF, two projects made use of the metal-air level set methodology in welding simulations and showed promising results. Desmaison et al. [2014] employed this methodology to simulate a hybrid arc and laser beam welding used in high thickness steel sheet welding. Later, Chen [2014] applied it to gas metal arc welding (GMAW) to predict the grain structure in the heat affected zone essentially. More recently, Courtois et al. [2014] used the same methodology but this time to predict keyhole defect formation in spot laser welding. The tracked interface in this case was that between the molten alloy and the corresponding vapor phase.

## 2.4 The level set method

Firstly introduced by Osher et al. [1988], this method became very popular in studying multiphase flows. It is reminded that the term *multiphase* in computational domains usually refers to multiple fluids, and thus should not be mixed with definition of a phase in the current solidification context. For disambiguation, we shall use *multifluid flow* when needed. The great advantage lies in the way the interface between two fluids,  $F_1$  and  $F_2$  is implicitly captured, unlike other methods where the exact interface position is needed. In a discrete domain, the concept is to assign for each mesh node of position vector  $\vec{x}$ , the minimum distance  $d_\Gamma(\vec{x})$  separating it from an interface  $\Gamma$ . The distance function, denoted  $\alpha$  and defined in eq. (2.50), is then signed positive or negative, based on the fluid or domain to which the node belongs.

$$\alpha(\vec{x}) = \begin{cases} d_\Gamma(\vec{x}) & \text{if } \vec{x} \in F_1 \\ -d_\Gamma(\vec{x}) & \text{if } \vec{x} \in F_2 \\ 0 & \text{if } \vec{x} \in \Gamma_{F1,F2} \end{cases} \quad (2.50)$$

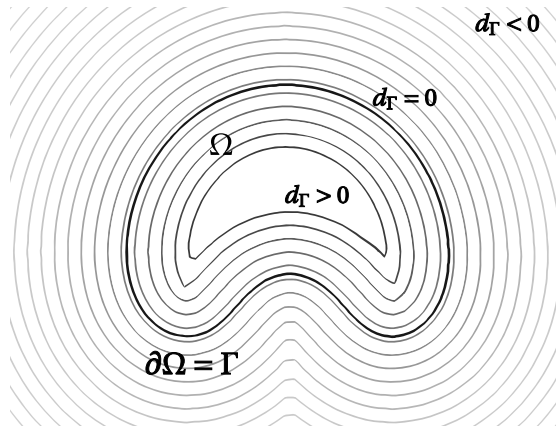


**Fig. 2.4** – Schematic of the interface  $\Gamma$  (thick black line) of a rising air bubble ( $\Omega$ ) in water. The other contours represent isovalues of the distance function around and inside the interface contour. Those outside are signed negative whereas inside they are signed positive.

#### 2.4.1 Diffuse interface

The level set has many attractive properties that allows seamless implementation in 2D and 3D models. It is a continuously differentiable  $C^1$ -function. The Heaviside function is also continuous but non differentiable, with an abrupt transition from 0 to 1 across the sharp interface, as follows:

$$H = H(\alpha(\vec{x})) = \begin{cases} 0 & \text{if } \alpha(\vec{x}) < 0 \\ 1 & \text{if } \alpha(\vec{x}) \geq 0 \end{cases} \quad (2.51)$$

With the help of [eq. \(2.51\)](#), we can define the geometric "presence" of a domain with respect to the interface. As such, material properties depend upon this function, which will be discussed later in [section 2.4.2](#). It is established that a steep transition can lead to numerical problems, so the Heaviside function should be smoothed in a volume of fixed thickness around the interface. Sinusoidal smoothing in [eq. \(2.52\)](#) is widely used with level set formulations.

$$H = \begin{cases} 0 & \text{if } \alpha(\vec{x}) < -\varepsilon \\ 1 & \text{if } \alpha(\vec{x}) > \varepsilon \\ \frac{1}{2} \left( 1 + \frac{\alpha(\vec{x})}{\varepsilon} + \frac{1}{\pi} \sin \left( \frac{\pi \alpha(\vec{x})}{\varepsilon} \right) \right) & \text{if } -\varepsilon \leq \alpha(\vec{x}) \leq \varepsilon \end{cases} \quad (2.52)$$

where the interval  $[-\varepsilon; +\varepsilon]$  is an artificial interface thickness around the zero distance. Defining a diffuse interface rather than a sharp one, is also a common approach in phase field methods [[Beckermann et al. 1999](#); [Sun et al. 2004](#)]. It is emphasized that the latter methods give physically meaningful analysis of a diffuse interface and the optimal thickness by thoroughly studying the intricate phenomena happening at the

scale of the interface. However, for level set methods, there has not been a formal work leading the same type of analysis. For this reason, many aspects of the level set method lack physical meanings but remain computationally useful. In a recent paper by [Gada et al. \[2009\]](#), the authors respond partially to this problem by analysing and deriving conservation equations using a level set in a more meaningful way, but do not discuss the diffuse interface aspect.

The Dirac delta function is also an important property to convert surface integrals to volume terms, which could turn useful when modelling surface tension effects for instance, using the *continuum surface force* method (CSF) [[Brackbill et al. 1992](#)]. The Dirac function, plotted in [fig. 2.5](#) along with the Heaviside function within an interface thickness of  $[-\varepsilon; +\varepsilon]$ , is derived from the Heaviside as follows:

$$\delta(\alpha) = \delta(\alpha(\vec{x})) = \frac{\partial H}{\partial \alpha(\vec{x})} = \begin{cases} \frac{1}{2\varepsilon} \left(1 + \cos\left(\frac{\pi\alpha(\vec{x})}{\varepsilon}\right)\right) & \text{if } |\alpha(\vec{x})| \leq \varepsilon \\ 0 & \text{if } |\alpha(\vec{x})| > \varepsilon \end{cases} \quad (2.53)$$

The Heaviside and delta Dirac functions can be readily processed to obtain other geometric properties from the level set, which are extremely useful. We mention the most relevant ones [[Peng et al. 1999](#)]:

$$\text{normal vector : } \vec{n} = \frac{\vec{\nabla}\alpha}{\|\vec{\nabla}\alpha\|} \quad (2.54)$$

$$\text{curvature : } \zeta = -\nabla \cdot \vec{n} \quad (2.55)$$

$$\text{surface area of the air-metal interface : } A^\Gamma = \int_{\Omega} \delta(\alpha) \|\vec{\nabla}\alpha\| d\Omega \quad (2.56)$$

$$\text{metal volume : } V^M = \int_{\Omega} H^M d\Omega \quad (2.57)$$

where, for the last two equations, we consider a three-dimensional domain  $\Omega$  containing two subdomains, metal and air, separated by an interface  $\Gamma$ . It is reminded that for a 2D case, [eq. \(2.56\)](#) evaluates a length instead of the area while [eq. \(2.57\)](#) gives the area instead of volume. Finally, within the diffuse interface, fluids properties may vary linearly or not, depending on the mixing law, which is presented in the next section.

### 2.4.2 Mixing Laws

A *monolithic* resolution style, as opposed to a *partitioned* resolution, is based on solving a single set of equations for both fluids separated by an interface, as if a single fluid were considered. Level set is one among many methods that use the monolithic style to derive a single set of conservation equations for both fluids. The switch from one material to the other is implicitly taken care of by using the Heaviside function as well as mixing laws. These laws are crucial to define how properties vary across

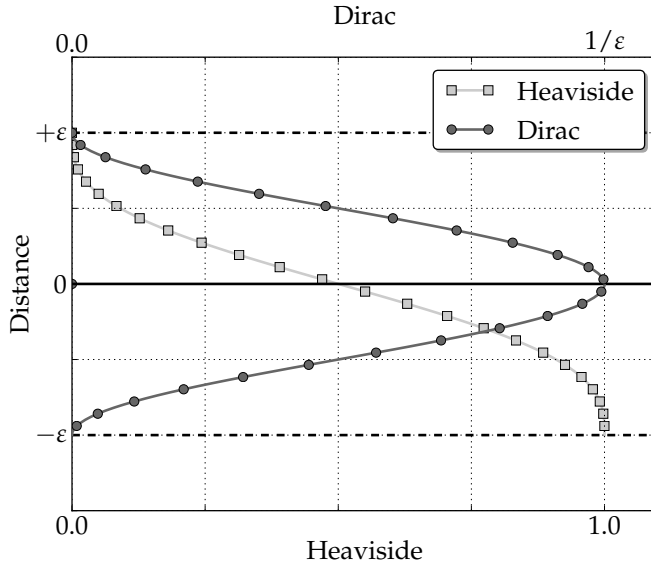


**Fig. 2.5** – Schematic of two level properties inside the diffuse interface: Heaviside (lower x-axis) and Dirac delta (upper x-axis) functions. Note that the peak of the Dirac function depends on the interface thickness to ensure a unity integral of the delta function over  $\Omega$ .

the diffuse interface in view of a more accurate resolution. The most frequently used mixing law in the literature is the arithmetic law. Other transitions are less known such as the harmonic and logarithmic mixing. The first law is maybe the most intuitive and most used for properties mixture as it emanates from VOF-based methods. If we consider any property  $\psi$  (for instance the fluid's dynamic viscosity  $\mu$ ) then the arithmetic law will give a mixed property  $\hat{\psi}$  as follows:

$$\hat{\psi} = H^{F_1} \psi^{F_1} + H^{F_2} \psi^{F_2} \quad (2.58)$$

Basically, the result is an average property that follows the same trend as the Heaviside function. As for the harmonic law, it writes:

$$\hat{\psi} = \left( \frac{H^{F_1}}{\psi^{F_1}} + \frac{H^{F_2}}{\psi^{F_2}} \right)^{-1} \quad (2.59)$$

and last, the logarithmic law writes:

$$\hat{\psi} = n^{(H^{F_1} \log_n \psi^{F_1} + H^{F_2} \log_n \psi^{F_2})} \quad (2.60)$$

where  $n$  is any real number serving as a logarithm base, which often is either the exponential  $e$  or 10. The mixture result with this law is the same, regardless of the value of  $n$ . By looking to [fig. 2.6](#), we clearly see that the difference between all three approaches is the property weight given to each side of the level set in the mixture. The arithmetic law, being symmetric, has equal weights,  $\psi^{F_1}$  and  $\psi^{F_2}$ , in the final mixture.

Nevertheless, the asymmetric harmonic mixing varies inside the diffuse interface with a dominant weight of one property over the other. As for the logarithmic mixture, it can be seen as an intermediate transition between the preceding laws. As long

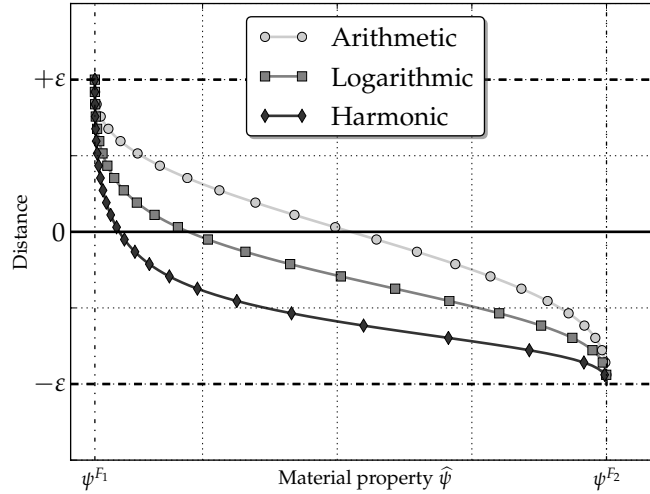


**Fig. 2.6** – Three mixing laws, arithmetic, logarithmic and harmonic commonly used in monolithic formulations.

as the interface thickness is small enough, the choice of a mixing law should not drastically change the result, inasmuch as it depends on the discretisation resolution of the interface. This fact made the arithmetic mixing the most applied one, because it is symmetric and easy to implement (no handling of potential division problems like harmonic laws for instance). However, [Stratos et al. \[2008\]](#) claim that the harmonic law proves to conserve better diffusive fluxes at the interface. More recently, an interesting study made by [Ettrich et al. \[2014\]](#) focused on mixing thermal properties using a phase field method. They define a diffuse interface in which they separately mix the thermal conductivity,  $\kappa$ , and the heat capacity,  $C_p$ , then compute the thermal diffusivity as the ratio of these properties. Later, the authors compare the temperature field obtained by diffusion to a reference case in order to decide which combination of mixing laws gives the best result. Despite not being directly related to a level set method, this work gives an insight of the mixture possibilities and their effect on a pure thermal diffusion. Otherwise, little work has been found in the literature on the broad effects of mixture types on simulation results in a level set context.

## 2.5 Interface motion

When a physical interface needs to have topology changes because of fluid structure interaction or surface tension for instance, the level set model can follow these changes by a transport step. The idea is to advect the signed distance function, its zero

isovalue representing the interface and all other distant isovales, with the velocity field as input. The motion of the interface is thus expressed by:

$$\frac{d\alpha}{dt} = \frac{\partial\alpha}{\partial t} + \vec{v} \cdot \vec{\nabla}\alpha = 0 \quad (2.61)$$

### 2.5.1 Level set transport

The finite element method gives the fully discretised weak form of [eq. \(2.61\)](#) by using a convenient set of test functions  $\alpha^*$  belonging the Hilbertian *Sobolev* space:

$$\int_{\Omega} \alpha^* \frac{\partial\alpha}{\partial t} d\Omega + \int_{\Omega} \alpha^* \vec{v} \cdot \vec{\nabla}\alpha d\Omega = 0 \quad \forall \alpha^* \in \mathcal{H}^1(\Omega) \quad (2.62)$$

The spatial discretisation of  $\alpha$  assigns, for each of the total  $N$  nodes of a simplex, the following values:

$$\alpha = \sum_N P_j \alpha_j \quad (2.63)$$

Furthermore, with the standard Galerkin method, we replace test functions by the interpolation functions  $P_j$ , then we apply a temporal discretisation for the main unknowns by a forward (implicit) finite difference in time. Consequently, [eq. \(2.62\)](#) can be recast as follows:

$$i, j : 1 \rightarrow \text{Nnodes}$$

$$\frac{1}{\Delta t} (\alpha_j^t - \alpha_j^{t-\Delta t}) \int_{\Omega} P_i P_j d\Omega + \alpha_j^t \int_{\Omega} \vec{v}^t \cdot \vec{\nabla} P_j d\Omega = 0 \quad (2.64a)$$

$$\left[ \frac{1}{\Delta t} \int_{\Omega} P_i P_j d\Omega + \int_{\Omega} \vec{v}^t \cdot \vec{\nabla} P_j d\Omega \right] \alpha_j^t = \frac{1}{\Delta t} \int_{\Omega} \alpha^{t-\Delta t} P_i d\Omega \quad (2.64b)$$

$$[\mathcal{M}_{ij} + \mathcal{A}_{ij}] \alpha_j^t = \mathcal{F}_i \quad (2.64c)$$

where  $\mathcal{M}_{ij}$  and  $\mathcal{A}_{ij}$  are respectively the mass (or capacity) matrix and advection matrix, both written within a local finite element, whereas  $\mathcal{F}_i$  is a local vector of known quantities from the previous time step. The solution of the linear system in [eq. \(2.64c\)](#) is the transported distance function.

When the convection regime becomes more dominant diffusion (for high Reynolds number), the standard Galerkin method may lead to instabilities in the solution. In this case, stabilisation is crucial to avoid these oscillations, unless very fine remeshing is done "such that convection no longer dominates on an element level", as stated by [Brooks et al. \[1982\]](#). The authors give a brief explanation of how numerically a convection-dominated equation can lead to oscillatory solutions with the standard Galerkin approximation. They proposed a stabilisation scheme, the Streamline Up-

wind Petrov-Galerkin, better known as SUPG, to stabilise advection dominated Navier-Stokes equations. However, their technique applies to any convection-diffusion equation. The SUPG method consists of modifying the test functions (like a classical Petrov-Galerkin method) by adding artificial diffusion in the flow direction. The modified test function writes:

$$\alpha_{SUPG}^* = \alpha^* + \underbrace{C_{SUPG}^E (\vec{v}_{\text{transport}} \cdot \vec{\nabla} \alpha^*)}_{\text{Upwind contribution}} \quad (2.65)$$

where the upwind contribution for each finite element  $E$  depends on a stabilisation parameter  $C_{SUPG}^E$  that is expressed as follows:

$$C_{SUPG}^E = \frac{h^E}{v_{\text{flow}}^E} \quad (2.66)$$

[Equation \(2.66\)](#) shows that the SUPG parameter represents a time constant relative to an element mesh size,  $h^E$ , and an average velocity that should represent the magnitude in the flow direction. In the present work, all convection-diffusion equations are stabilised with the SUPG method, namely the conservation of mass, energy, momentum and chemical species as well as the level set transport.

### 2.5.2 Level set regularisation

Upon transport the distance function field, a crucial property of the level set may be partially or totally lost over the domain, which is:

$$\begin{cases} \|\vec{\nabla} \alpha\| = 1 \\ \alpha(x, t) = 0 & \text{if } x \in \Gamma(t) \end{cases} \quad (2.67)$$

The closer this  $L^2$ -norm to one, the more regular the level set. An irregular distance function induces cumulative numerical errors while transporting distance values far from the interface, resulting in wrong distance information, and loss of properties that make up a "distance function". To show one the benefit of level set regularisation, [Basset \[2006\]](#) states after showing several tests of distance function transport, that regularised distance functions transported with a standard Galerkin method (i.e. without any stabilisation) show better "quality" globally in the domain, compared to initially non-regularised ones. When the transport equation in [eq. \(2.61\)](#) is discretised in time then solved, a *regularisation* (also known as *reinitialisation*) is necessary to conserve as much as possible the property in [eq. \(2.67\)](#).

[Figure 2.7](#) shows the need of regularisation in two different simulations of the same phenomenon: rising air bubble inside water. The importance of this well studied case

[Sussman et al. 1994; Hysing et al. 2009] is that the interface between two fluids is highly deformable as the bubble rises because of buoyancy, and therefore the task of tracking the dynamic interface while maintaining an accurate distance function is a considerable numerical task. In the first simulation, the distance contours are squeezed against the zero-distance contour marked by the thick black line. A closer look to the interface reveals undesired distortions, with a "wavy" shape at some points. This effect is evidently an artefact of a level set transport lacking subsequent reinitialisation, inasmuch as the surface tension tends to minimise the total surface area and make it as smooth as possible. Nevertheless, the second simulation unveils much better results, especially how the interface shows no sign of destabilisation. We also note the regular spacing between contours, which is a consequence of conserving the property defined in eq. (2.67). This improvement is attributed to the regularization done at each time step after the transport. In the forthcoming sections, we present two regularisation methods, then show their strong and weak points.

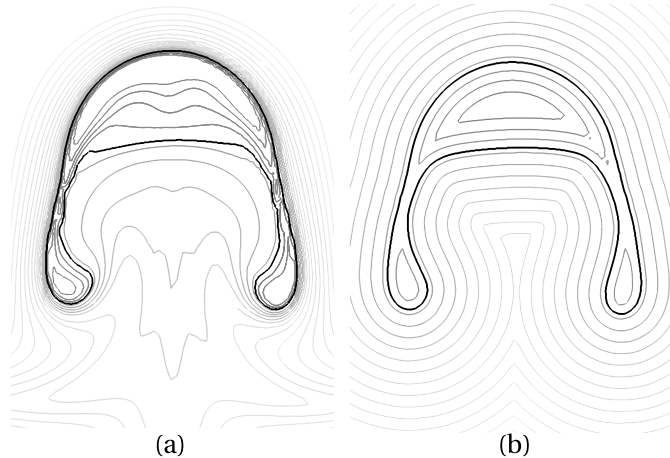


**Fig. 2.7** – Schematic of the influence of level set regularisation on the distance function at the same time frame: a) without any regularisation step, the isovalue contours are distorted in the wake of the rising air bubble while being squeezed ahead of it, b) in contrast to regularising the distance function, where the contours maintain their spacing and geometric properties with respect to the tracked interface.

### Classic Hamilton-Jacobi reinitialisation

In order to repair a distance function impaired by convective transport, Sussman et al. [1994] proposed solving a classic *Hamilton-Jacobi* equation, given in its most general form:

$$\frac{\partial \alpha}{\partial t} + \mathbb{H}(\alpha, x, t) = 0 \quad x \in \Omega, t > 0 \quad (2.68)$$

where  $\alpha(x, t = 0) = \alpha_0$  is the initial value of the distance function. The term  $\mathbb{H}$  is known as the *Hamiltonian*. When the sign of the level set and its metric property ( $\|\vec{\nabla}\alpha\| = 1$ ) are considered, eq. (2.68) reduces to:

$$\frac{\partial \alpha}{\partial t} + S(\alpha) (\|\vec{\nabla}\alpha\| - 1) = 0 \quad (2.69)$$

where  $S(\alpha)$  is a step function giving the sign of the level set as follows:

$$S(\alpha) = \frac{\alpha}{|\alpha|} = \begin{cases} -1 & \text{if } \alpha < 0 \\ 0 & \text{if } \alpha = 0 \\ +1 & \text{if } \alpha > 0 \end{cases} \quad (2.70)$$

The sign function defined in eq. (2.70) is often smoothed to avoid numerical problems, as proposed for instance by [Sussman et al. \[1994\]](#):

$$S(\alpha) = S_\varepsilon(\alpha) = \frac{\alpha}{\sqrt{\alpha^2 + \varepsilon^2}} \quad (2.71)$$

where  $\varepsilon$  is a smoothing parameter that depends on the mesh size around the interface. However, one should be aware that within the smoothing thickness, the regularised function may suffer from local oscillations because of the reciprocal reinitialisation taking place at each side of the level set. [Peng et al. \[1999\]](#) states that this problem is more likely to happen if the initial level set shows very weak or very steep gradients, and therefore is not regular enough. The authors eventually propose a new sign function which would reinitialise the distance function, as close as possible to the interface without modifying the latter, as follows:

$$S(\alpha) = S_\varepsilon(\alpha) = \frac{\alpha}{\sqrt{\alpha^2 + \|\vec{\nabla}\alpha\|^2 \varepsilon^2}} \quad (2.72)$$

### Convective reinitialization

A recent work by [Ville et al. \[2011\]](#) introduced another concept for reinitialisation called the *convective reinitialisation*. The idea lies in combining both level set advection and regularisation in a single equation, saving resolution time. The key components of their method starts by defining a pseudo time step,  $\Delta\tau$ , that is linked to the main time variable through a numerical parameter  $\lambda_\tau$ , as follows:

$$\lambda_\tau = \frac{\partial \tau}{\partial t} \quad (2.73)$$

The order of magnitude of  $\lambda_\tau$ , which can be seen as a relaxation parameter [see [Vigneaux 2007, p. 89](#)], is close to the ratio  $h/\Delta t$ . Then, the classic Hamilton-Jacobi

eq. (2.68) is combined into the convection step by writing:

$$\frac{\partial \alpha}{\partial t} + (\vec{v} + \lambda_\tau \vec{U}) \cdot \vec{\nabla} \alpha = \lambda_\tau S(\alpha) \quad (2.74)$$

where  $\vec{U}$  is a velocity vector in the normal direction to the interface, defined by  $\vec{U} = S(\alpha)\vec{n}$ , the normal vector  $\vec{n}$  being previously defined in eq. (2.54). The obvious shortcoming of convective reinitialisation is that it depends on a numerical parameter  $\lambda_\tau$ . Another limitation of the method is the use of a sinusoidal filter to modify the distance function by truncating its values beyond a thickness threshold, which is also another parameter to calibrate the resolution. The drawback of truncating the level set is the loss of information far from the interface and the inability to fully reconstruct the distance function. If we denote this threshold by  $E$  and the modified level set by  $\tilde{\alpha}$  inside the thickness, then eq. (2.74) is recast as:

$$\frac{\partial \alpha}{\partial t} + (\vec{v} + \lambda_\tau \vec{U}) \cdot \vec{\nabla} \alpha = \lambda_\tau S(\alpha) \sqrt{1 - \left(\frac{\pi}{2E}\tilde{\alpha}\right)^2} \quad (2.75)$$

Equation (2.75) describes the transport and partial reconstruction of the distance function  $\alpha$ , knowing its value  $\tilde{\alpha}$  inside the thickness  $E$ .

### Geometric reinitialization

This category of methods go from the level set's basic geometric principle to construct a distance function, instead of solving a partial differential system of equations as in the classic Hamilton-Jacobi reinitialisation. A widely known instance of this category is the *fast marching method* developed by Sethian [1996] and influenced by the Dijkstra [1959]'s method to compute the shortest path in a network of nodes. The method aims to solve the eikonal equation in eq. (2.67) to propagate the distance function in a single direction by *upwinding*, i.e. going from low to high values of the distance function, while preserving a unitary distance gradient.

*Direct reinitialisation* is another interesting method in the geometric reinitialise category. However, it has not gained noticeable attention in the literature given the terrible cost in terms of computation time and efficiency if not optimised. The main idea is very simple: reconstruct the distance function over  $\Omega$  or a subset of  $\Omega$ , by computing the minimum distance between each mesh node and the interface. It means that, for any point  $\vec{x} \in \Omega$ , the following constraint should be satisfied Osher et al. [2003]:

$$d_\Gamma(\vec{x}) = \min \|\vec{x} - \vec{x}_\Gamma\| \quad \forall \vec{x}_\Gamma \in \partial\Omega = \Gamma, \quad (2.76)$$

A efficient and optimised implementation of this method is done by Shakoor et al. [2015] making use of *k-d* trees to limit the search operations of elements and the subsequent distance evaluations in each of these elements. Moreover, the authors

give a comparison of the previously stated methods on 2D and 3D cases, showing the great performance of direction reinitialisation when used with k-d trees algorithm, hence we use it in the present work.

### To do ?

Interface Remeshing: Importance when using a static level set and more importantly when LS is transported, influence of mixing area *thickness* and *resolution* (i.e. nb of nodes with the area), Isotropic or anisotropic ? the first is more important to composition calculation while the second is more relevant if we mean do thermohydraulics without macrosegregation



# Chapter 3

## Energy balance with thermodynamic tabulations

### Contents

---

<b>3.1 State of the art . . . . .</b>	<b>40</b>
<b>3.2 Thermodynamic considerations . . . . .</b>	<b>40</b>
3.2.1 Volume averaging . . . . .	40
3.2.2 The temperature-enthalpy relationship . . . . .	41
3.2.3 Tabulation of properties . . . . .	42
<b>3.3 Numerical method . . . . .</b>	<b>43</b>
3.3.1 Enthalpy-based approach . . . . .	47
3.3.2 Temperature-based approach . . . . .	47
3.3.3 Convergence . . . . .	48
<b>3.4 Validation . . . . .</b>	<b>49</b>
3.4.1 Pure diffusion . . . . .	49
3.4.2 Convection and diffusion . . . . .	52
<b>3.5 Application: multicomponent alloy solidification . . . . .</b>	<b>55</b>
3.5.1 Tabulations . . . . .	57
3.5.2 Discussion . . . . .	58

---

## 3.1 State of the art

When speaking about macrosegregation, one needs to know that the problem involves phase change. For that, a minimum of four conservation equations are necessary: conservation of mass, momentum, chemical species and energy. The phase change literature contains a wealth of numerical methods to solve energy conservation in solidifying alloys. A comprehensive overview of these methods is given by [Swaminathan. et al. \[1993\]](#). The corresponding equation associates the total average enthalpy to the temperature via intrinsic alloy properties, such as the heat capacity of the phases and the latent heat associated with the phase transformations. However, in the course of solidification and while macrosegregation is taking place, these properties change because the average composition may vary significantly: the transformation paths are thus modified, as well as the phases' composition and heat capacity. Similarly, the latent heat of phase transformations is not a mere constant that could be distributed as a function of the phase fractions assuming only temperature-dependent phases' properties, as often found in the literature [\[Bellet et al. 2009\]](#). It is thus impossible to establish a priori the dependence of the enthalpy with respect to temperature when macrosegregation alters the average composition, even in the case of full thermodynamic equilibrium between phases. In this chapter, we discuss a suitable numerical scheme based on an enthalpy method, already used in the literature to alleviate this macrosegregation-related problem [\[Swaminathan. et al. 1993; Carozzani et al. 2013\]](#). Later on, we introduce a modified formulation, using the effective heat capacity method that increases the original scheme's efficiency.

The method introduced in this chapter is an enthalpy method that makes use of a temperature-based solver. Moreover, it uses tabulated thermodynamic quantities (solidification paths, phases' enthalpy and composition) in a range of average compositions and temperatures as found in the literature [\[Doré et al. 2000; Thuinet et al. 2004; Du et al. 2007\]](#), with the aim of evaluating the total average enthalpy as well as the effective heat capacity. The novelty of the modified method resides in the use of thermodynamic tabulations without losing the advantages of the previous method, thus yielding faster computation times while maintaining a good accuracy.

## 3.2 Thermodynamic considerations

### 3.2.1 Volume averaging

The volume averaging technique, presented in [section 2.1.4](#), is the first thing consider when solving the energy equation in the presence of macrosegregation. The reason is that phase quantities that vary with the average composition, have a great impact on the thermal properties, hence on the overall heat transfer in the system. We recall the

basic equation:

$$\langle \psi \rangle = \sum_{\phi} g^{\phi} \langle \psi \rangle^{\phi} \quad (3.1)$$

where  $g^{\phi}$  denotes the volume fraction of phase  $\phi$  in the RVE. It should be emphasized that the averaging technique applies to virtually all thermodynamic variables (enthalpy, density . . .). Among these variables, the temperature is also considered to be uniform in the RVE. Applying the volume averaging technique to the energy conservation principle along with interfacial balances between the phases, results in the following averaged equation [Rappaz et al. 2003]:

$$\frac{\partial \langle \rho h \rangle}{\partial t} + \vec{\nabla} \cdot (\langle \rho h \vec{v} \rangle) = \vec{\nabla} \cdot (\langle \kappa \rangle \vec{\nabla} T) + \langle \dot{Q}_V \rangle \quad (3.2)$$

where  $\rho$  stands for the density,  $h$  the mass enthalpy,  $\vec{v}$  the velocity field,  $\kappa$  the thermal conductivity,  $T$  the temperature and  $\dot{Q}_V$  a possible volume heat source. [Equation \(3.2\)](#) is the standard averaged form of the energy conservation equation used in non-stationary phase change problems.

I could elaborate more in this paragraph by showing the possible equations for the explicit formulation and maybe a figure to show the AlSi7 computation that I did with a very small time step

Once the variational form has been discretised in space and time, two possible resolution schemes emerge: the first is an explicit forward Euler scheme which gives rise to a linear equation where the temperature is known at time  $t$ ,  $T^t$ . This requires very small time steps in the current context, which limits the solver's usability at the scale of industrial applications. The second scheme is the backward Euler or full implicit discretisation where terms are function of  $T^{t+\Delta t}$ . It leads to a nonlinear equation with 2 interdependent unknowns,  $\langle \rho h \rangle^{t+\Delta t}$  and  $T^{t+\Delta t}$ . It is clear that the nature of the temperature-enthalpy relationship plays a central role when formulating the resolution strategy of this nonlinear equation. Generally, it is admitted that, depending on the resolution strategy, it is necessary to express enthalpy as a function of temperature or vice-versa, together with associated partial derivatives,  $\frac{d\langle \rho h \rangle}{dT}$  or  $\frac{dT}{d\langle \rho h \rangle}$ .

### 3.2.2 The temperature-enthalpy relationship

In solidification problems, additional variables are involved in [eq. \(3.1\)](#) and [eq. \(3.2\)](#), like the transformation path that defines the history of the phase fractions, as well as the average chemical composition  $\langle w_i \rangle$ ,  $i$  being the index of the chemical species (only the solutes are considered). The temperature-enthalpy relation averaged over

the phases in a given RVE writes:

$$\langle \rho h \rangle = \sum_{\phi} g^{\phi}_{(T, \langle w_i \rangle \dots)} \rho^{\phi}_{(T, \langle w_i \rangle^{\phi} \dots)} h^{\phi}_{(T, \langle w_i \rangle^{\phi} \dots)} \quad (3.3)$$

Note that the volume average enthalpy is approximated by the product  $\langle \rho h \rangle^{\phi} = \langle \rho \rangle^{\phi} \langle h \rangle^{\phi}$  in the current work. As stated in the introduction, it becomes clear from [eq. \(3.3\)](#) that phase properties, i.e. average phase density,  $\rho^{\phi}$  and enthalpy,  $h^{\phi}$ , are temperature and composition dependent. This equation is the key to convert the average volume enthalpy to temperature (through a procedure named *H2T*) or vice-versa (*T2H*). The values of the different phase fractions  $g^{\phi}$  (solidification path) and phase enthalpies  $\langle \rho h \rangle^{\phi}$  are thus needed to close the relation.

### 3.2.3 Tabulation of properties

The complexity of performing a thermodynamic conversion is directly linked to the simplicity of determining the alloy properties, namely the phase fractions and phase enthalpies. In the case of binary alloys and with several assumptions with respect to the system (e.g., linear mono-variant temperature composition relationships, constant heat capacity of phases and constant latent heat of transformations, equilibrium approximations between phases) analytical calculations are often used to determine the properties. Nevertheless, analytical relations are more complex or even impossible to derive in the case of multicomponent alloys ( $i > 1$ ). To overcome this problem, one can resort to thermodynamic databases and phase equilibrium calculations to tabulate the transformation paths and the phase enthalpies for a given range of temperatures and average compositions. It is a handy solution for two main reasons: first, the conversion is merely a binary search in a table; secondly, it is a simple solution for coupling with macrosegregation. In this way, phase fractions  $g^{\phi}$  are tabulated as functions of temperature and average composition, while for each phase  $\phi$  the mass enthalpy,  $h^{\phi}$ , and the density,  $\rho^{\phi}$ , are tabulated as functions of temperature and phase intrinsic average compositions  $\langle w_i \rangle^{\phi}$ , as well as other possible parameters. [Table 3.1](#) summarizes the steps in order to perform a temperature-to-enthalpy (*T2H*) conversion using the predefined tabulation approach. In step 1, the transformation path is acquired for each average composition and temperature to determine the list of phases, their volume fractions  $g^{\phi}$  and their intrinsic compositions  $\langle w_i \rangle^{\phi}$ . In step 2, the phase enthalpy  $h^{\phi}$  and density  $\rho^{\phi}$  are determined by searching for the temperature and the already known phase composition  $\langle w_i \rangle^{\phi}$ . In step 3, the average volume enthalpy is computed from the volume fraction, density and mass enthalpy of phases using [eq. \(3.3\)](#). The methodology to build the tabulations is straightforward. It is based on two main scans. On the one hand, intervals for the variation of the average composition  $\langle w_i \rangle$  are chosen from the known alloy composition. These variations have to cover the extreme

**Table 3.1** – Tabulation processing for a  $T2H$  procedure

Step Number	1	2	3
Inputs	$T, \langle w_i \rangle$	$T, \langle w_i \rangle^\phi$	$g^\phi, \rho^\phi h^\phi$
Outputs	$g^\phi, \langle w_i \rangle^\phi$	$\rho^\phi, h^\phi$	$\langle ph \rangle$ (eq. (3.3))

values adopted during the simulation, which are not known a priori. An interval is also selected for the variation of temperature. The latter is easier to determine as it usually starts from the initial melt temperature and goes down to the room temperature in a standard casting simulation. For each mapping of composition and temperature, a thermodynamic equilibrium state is computed. The outputs are the number of phases encountered, together with their fraction and intrinsic compositions. The minimum and maximum intrinsic composition for each phase could then be determined. On the other hand, for each phase, a scan of the intrinsic composition and temperature is made to compute the intrinsic properties. The same temperature interval and step as defined earlier are used. Regarding the enthalpy-to-temperature conversion ( $H2T$ ), a backward iterative  $T2H$  search is performed. For a known composition  $\langle w_i \rangle$ , denoting  $(\tau)$  the iteration index to convert the enthalpy  $H_{\text{input}}$ , we start with an initial guess for temperature  $T^{(\tau=0)}$  then convert it to an enthalpy  $H^{(\tau=0)}$  with the  $T2H$  conversion. Using an appropriate nonlinear algorithm (Brent is the most versatile in our case), we aim at minimizing the following scalar residual:  $R_H = |H_{\text{input}} - H^{(\tau)}|$ . Once the algorithm has converged, the temperature  $T^{(\tau)}$  is the result of the  $H2T$  conversion. It is inferred that the first conversion ( $T2H$ ) is a direct one whereas the latter ( $H2T$ ) is indirect and requires a series of iterative steps; each step being a single  $T2H$  resolution. In other words, a  $H2T$  conversion is a backward search for a temperature, hence it is slower. This conversion's speed lag is exacerbated when tabulations increase in size (e.g. large number of temperature and composition steps) and complexity (e.g., multi-component industrial alloys used in casting), since the search gets more complicated with the increasing number of input columns (one column for each alloying element).

### 3.3 Numerical method

The finite element method is used to solve the energy conservation as expressed by eq. (3.2). A test function  $\mathcal{W}$  belonging to the Hilbertian Sobolev space  $\mathcal{H}^1(\Omega_E)$  of continuous integrable test functions is used to formulate the integral variational form of eq. (3.2) [Süli 2000]. A Fourier boundary condition is considered on the domain boundary  $\partial\Omega_E$ . The domain  $\Omega$  is discretised using first-order linear simplexes,  $\Omega_E$ , defined by their number of local nodes (denoted “NbLoc”): triangles in 2D with NbLoc=3 and tetrahedra in 3D with NbLoc=4. The outcome is a residual that we aim to minimize so

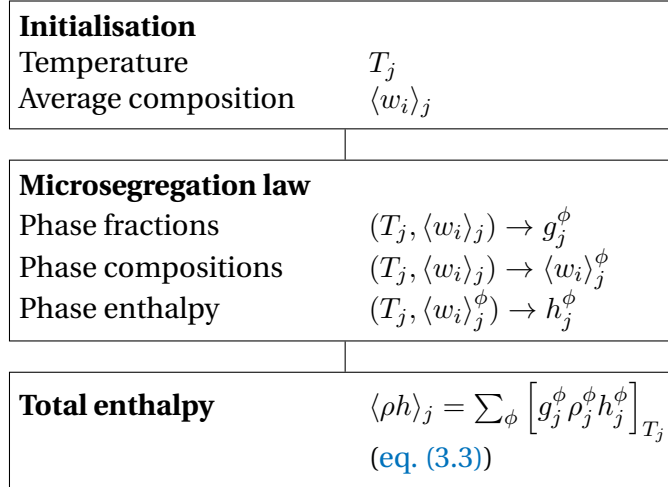


**Fig. 3.1** – Algorithm for a single temperature to enthalpy ( $T2H$ ) conversion.

that the conservation principle is satisfied. Therefore, the weak form writes:

$$\begin{aligned} \forall \mathcal{W} \in M = \{u \in \mathcal{H}^1(\Omega_E)\} \\ \int_{\Omega_E} \mathcal{W} \frac{\partial \langle \rho h \rangle}{\partial t} dV + \int_{\Omega_E} \mathcal{W} \langle \vec{v}^l \rangle \cdot \vec{\nabla} (\rho^l h^l) dV - \int_{\Omega_E} \mathcal{W} \nabla \cdot (\langle \kappa \rangle \vec{\nabla} T) dV - \int_{\Omega_E} \mathcal{W} \langle \dot{Q}_V \rangle dV = 0 \end{aligned} \quad (3.4)$$

where we assumed a static solid phase and an incompressible liquid phase, which allowed recasting the second term of [eq. \(3.2\)](#) into  $\langle \vec{v}^l \rangle \cdot \vec{\nabla} (\rho^l h^l)$ . The steps for discretizing in time and space the previous equation are well detailed in some book references like [Rappaz et al. \[2003\]](#) and [Dantzig et al. \[2009\]](#). As for enthalpy and temperature, they are spatially discretised in each simplex using interpolations functions  $\mathcal{P}$ , thus defining the nodal values  $H_j$  and  $T_j$ , respectively:

$$\langle \rho h \rangle = \sum_{j=1}^{\text{NbLoc}} \mathcal{P}_j H_j \quad (3.5)$$

$$T = \sum_{j=1}^{\text{NbLoc}} \mathcal{P}_j T_j \quad (3.6)$$

Note that  $H_j$  is a volumetric enthalpy. The Galerkin formulation gives the following expression for the residual contribution at a mesh node  $i$  (PS: here  $i$  is not the usual solute index) for time step  $t$  in a local element  $\Omega_E$ :

$$\begin{aligned} (R_i^E)^t &= \mathcal{M}_{ij}^E (H_j^t - H_j^{t-\Delta t}) + \mathcal{A}_{ij}^E T_j^t + (\mathcal{K}1_{ij}^E + \mathcal{K}2_{ij}^E) - \mathcal{F}_i^E - \mathcal{S}_i^E = 0 \\ i, j : 1 &\rightarrow \text{NbLoc} \end{aligned} \quad (3.7)$$

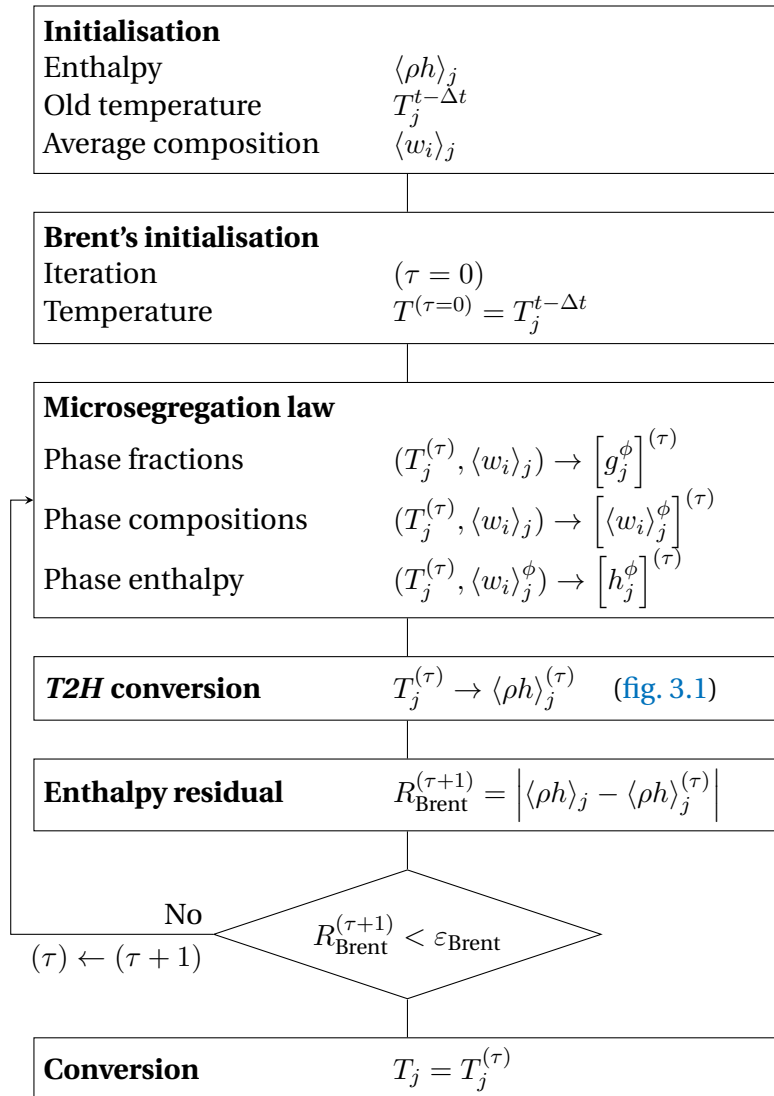


**Fig. 3.2 – Algorithm for a single enthalpy to temperature (H2T) conversion.**

### Chapter 3. Energy balance with thermodynamic tabulations

---

where the volumetric contributions are detailed as follows:

$$\text{transient term: } \mathcal{M}_{ij}^E = \int_{\Omega_E} \frac{1}{\Delta t} \mathcal{P}_i \mathcal{P}_j \, dV \quad (3.8)$$

$$\text{advection term: } \mathcal{A}_{ij}^E = \int_{\Omega_E} \rho^l C_p^l \mathcal{P}_i \langle \vec{v}^l \rangle \cdot \vec{\nabla} \mathcal{P}_j \, dV \quad (3.9)$$

$$\text{diffusion term: } \mathcal{K1}_{ij}^E = \int_{\Omega_E} \langle \kappa \rangle \vec{\nabla} \mathcal{P}_i \vec{\nabla} \mathcal{P}_j \, dV \quad (3.10)$$

$$\text{source term: } \mathcal{S}_i^E = \int_{\Omega_E} \mathcal{P}_i \langle \dot{Q}_V \rangle \, dV \quad (3.11)$$

while the surface boundary contributions are given by:

$$\text{boundary condition term 1: } \mathcal{K2}_{ij}^E = \int_{\partial\Omega_E} h_{\text{ext}} \mathcal{P}_i \mathcal{P}_j \, dS \quad (3.12)$$

$$\text{boundary condition term 2: } \mathcal{F}_i^E = \int_{\partial\Omega_E} h_{\text{ext}} T_{\text{ext}} \mathcal{P}_i \, dS \quad (3.13)$$

(3.14)

The surface integrals  $\mathcal{K2}_{ij}^E$  and  $\mathcal{F}_i^E$  are related to a Fourier-type boundary condition, with  $h_{\text{ext}}$  as a coefficient of heat exchange and  $T_{\text{ext}}$  as the external temperature far from the boundary. The energy conservation principle is satisfied when the sum of the residual contributions coming from all the mesh elements is zero. In other words, the following global residual defined by the assembly of these contributions, should be minimized:

$$(R_i)^t = \mathcal{M}_{ij} \left( H_j^t - H_j^{t-\Delta t} \right) + \mathcal{A}_{ij} T_j^t + (\mathcal{K1}_{ij} + \mathcal{K2}_{ij}) T_j^t - \mathcal{F}_i - \mathcal{S}_i = 0 \quad (3.15)$$

$i, j : 1 \rightarrow \text{NbGlob}$

where the global tensors  $\mathcal{M}_{ij}$ ,  $\mathcal{A}_{ij}$ ,  $\mathcal{K1}_{ij}$ ,  $\mathcal{K2}_{ij}$ ,  $\mathcal{F}_i$  and  $\mathcal{S}_i$  contain respectively, after an assembly step, the contributions of the local matrices  $\mathcal{M}_{ij}^E$ ,  $\mathcal{A}_{ij}^E$ ,  $\mathcal{K1}_{ij}^E$ ,  $\mathcal{K2}_{ij}^E$ ,  $\mathcal{F}_i^E$  and  $\mathcal{S}_i^E$  from each discretised element in the domain  $\Omega$ . Accordingly, the indices  $i$  and  $j$  refer to global node numbers, where the total number of nodes is denoted by "NbGlob". It is clear that the global residual inherits the dependence between enthalpy and temperature. This is shown in eq. (3.15) where the average volume enthalpy is a function of the temperature. It infers that this residual is a non-linear function; therefore minimizing it requires an iterative non-linear algorithm. Our choice settles on the Newton-Raphson method, known for its quadratic convergence speed. A solidification problem can induce severe non-linearities from the release of the latent heat (which itself is temperature-composition dependent) and the variations of the thermophysical properties of the alloy with respect to temperature and average composition. This algorithm could thus treat such variations. Considering the link

between enthalpy and temperature, eq. (3.15) may be solved either for enthalpy or for temperature as a nodal unknown; hence both formulations are presented hereafter.

### 3.3.1 Enthalpy-based approach

The residual is re-written using a Taylor series expansion to the first order for a non-linear iteration ( $\nu$ ) :

$$(R_i)^{(\nu+1)} = (R_i)^{(\nu)} + \left( \frac{dR}{dH} \right)_{ij}^{(\nu)} \Delta H_j^{(\nu)} + \mathcal{O}(H_j^2) \quad (3.16)$$

Neglecting the second order terms, the suggested correction at each iteration in view of cancelling the residual and giving the new value  $H_j^{(\nu)}$ , is given by the linear system in eq. (3.17) relative to what we call a *Hsolver*:

$$\left( \frac{dR}{dH} \right)_{ij}^{(\nu)} (H_j^{(\nu+1)} - H_j^{(\nu)}) = -R_i^{(\nu)} \quad (3.17)$$

where  $\frac{dR}{dH}$  is a global tangent matrix yielding the variations of the residual with respect to the enthalpy in the last iteration,  $H_j^{(\nu)}$ . If eq. (3.7) is considered, then the contribution of an element  $\Omega_E$  writes:

$$\left( \frac{dR}{dH} \right)_{ij}^{(\nu)E} = \underbrace{\mathcal{M}_{ij}^E + \mathcal{A}_{ij}^E \left( \frac{dT}{dH} \right)_j^{(\nu)}}_{\text{no sum on } j} + \underbrace{(\mathcal{K}1_{ij}^E + \mathcal{K}2_{ij}^E) \left( \frac{dT}{dH} \right)_j^{(\nu)}}_{\text{no sum on } j} \quad (3.18)$$

Equation (3.18) is the core of the enthalpy-based solver. The resolution of eq. (3.17) then yields a new estimate of the vector of nodal enthalpies  $H^{(\nu+1)}$ , which are the only unknowns to be solved for. Once determined at iteration ( $\nu$ ), convergence tests are performed (refer to section

### 3.3.2 Temperature-based approach

Similarly to the *Hsolver*, the local residual is recast for a nonlinear iteration ( $\nu$ ), leading this time to an iterative temperature correction:

$$\left( \frac{dR}{dT} \right)_{ij}^{(\nu)} (T_j^{(\nu+1)} - T_j^{(\nu)}) = -R_i^{(\nu)} \quad (3.19)$$

where  $\frac{dR}{dT}$  is a global tangent matrix yielding the variations of the residual with respect to temperature  $T_j^{(\nu)}$  at the previous iteration. This solver will be referred to as *Tsolver*.

The contribution of an element  $\Omega_E$  to this tangent matrix is evaluated as:

$$\left[ \left( \frac{dR}{dT} \right)_{ij}^{(\nu)} \right]^E = \underbrace{\mathcal{M}_{ij}^E \left( \frac{dH}{dT} \right)_j^{(\nu)}}_{\text{no sum on } j} + \mathcal{A}_{ij}^E + (\mathcal{K}1_{ij}^E + \mathcal{K}2_{ij}^E) \quad (3.20)$$

In contrast to the previous solver, eq. (3.20) is the core of the temperature-based solver. The resolution of eq. (3.19) then yields a new estimate of the vector of nodal temperatures  $T^{(\nu+1)}$ , which are the only unknowns to be solved for. Once updated for iteration  $(\nu)$ , convergence tests are performed (refer to section

### 3.3.3 Convergence

The previous two sections described the iterative resolution of the same discretised energy conservation by both Tsolver and Hsolver. However, in eqs. (3.18) and (3.20), an important term emerges from the tangent matrix evaluation describing the variations between temperature and enthalpy:  $\frac{dH}{dT}$  (or  $\frac{dT}{dH}$ ). This term invokes the previously mentioned temperature-enthalpy tabulations which depend on the alloy composition. Consequently,  $\frac{dH}{dT}$  (or  $\frac{dT}{dH}$ ) has a great influence on the convergence of the Tsolver (respectively the Hsolver). When eq. (3.17) or eq. (3.19) is solved at iteration  $(\nu)$ , this term is written using a finite difference:

$$\textbf{Tsolver} \quad \left( \frac{dH}{dT} \right)_j^{(\nu+1)} = \frac{\langle \rho h \rangle_j^{(\nu+1)} - \langle \rho h \rangle_j^{(\nu)}}{T_j^{(\nu+1)} - T_j^{(\nu)}} \quad (3.21)$$

$$\textbf{Hsolver} \quad \left( \frac{dT}{dH} \right)_j^{(\nu+1)} = \frac{T_j^{(\nu+1)} - T_j^{(\nu)}}{\langle \rho h \rangle_j^{(\nu+1)} - \langle \rho h \rangle_j^{(\nu)}} \quad (3.22)$$

For the Tsolver, the enthalpy  $\langle \rho h \rangle_j^{(\nu)}$  is needed to evaluate eq. (3.21). In contrast, the Hsolver requires the value of  $T_j^{(\nu)}$  to evaluate the corresponding eq. (3.22). In both cases, the unknown is determined by the temperature-enthalpy relation. The indices next to the mentioned unknowns indicate that this relation is used for each iteration  $(\nu)$  at each mesh node  $j$ , hence affecting the global resolution time between the two solvers. The Hsolver needs a  $H2T$  to evaluate  $\frac{dT}{dH}$ , whereas the Tsolver needs a  $T2H$  to evaluate  $\frac{dH}{dT}$ . It can be seen that Tsolver uses solely  $T2H$  procedure (flowchart in fig. 3.1) and the thermodynamic tabulations to determine the enthalpy, hence the term  $\frac{dH}{dT}$ . On the other hand, Hsolver repeats the same procedure a finite number of times in order to determine a temperature output through  $H2T$  (flowchart in fig. 3.2) and use it to compute  $\frac{dT}{dH}$ . This algorithmic difference leverages the Tsolver in terms of computation time providing the same numerical accuracy while conserving the total system energy.

Convergence tests are necessary at the end of each iteration of the energy solver to determine the convergence status of the algorithm. In the context of the Tsolver for instance, the residual is re-evaluated with the newly determined temperature  $T_j^{(\nu+1)}$  and enthalpy  $H_j^{(\nu+1)}$  so eq. (3.15) rewrites:

$$(R_i)^{(\nu+1)} = \mathcal{M}_{ij} \left( H_j^{(\nu+1)} - H_j^{t-\Delta t} \right) + \mathcal{A}_{ij} T_j^{(\nu+1)} + (\mathcal{K}1_{ij} + \mathcal{K}2_{ij}) T_j^{(\nu+1)} - \mathcal{F}_i - \mathcal{S}_i$$

$$i, j : 1 \rightarrow \text{NbGlob}$$
(3.23)

The norm of the current residual,  $\|R^{(\nu+1)}\|$ , is compared to a fixed small value  $\varepsilon_R \approx [10^{-5}; 10^{-4}]$ . The resulting temperature variation,  $|T_j^{(\nu)} - T_j^{(\nu-1)}|$ , should also respond to similar criterion between two consecutive iterations. For that purpose, we compare it to another fixed value  $\varepsilon_T \approx [10^{-3}; 10^{-2}]$ . Convergence is ultimately achieved when the following criteria are simultaneously met:

$$\begin{cases} \|R^{(\nu+1)}\| < \varepsilon_R \\ \text{Max}_{j:1 \rightarrow \text{NbGlob}} |T_j^{(\nu+1)} - T_j^{(\nu)}| < \varepsilon_T \end{cases}$$
(3.24)

A comparison of both solver formulations is done in the hereafter test cases section.

## 3.4 Validation

### 3.4.1 Pure diffusion

The two solvers are first tested in a purely diffusive case for a one-dimensional solidification configuration. Predictions with a 1D front tracking model [Gandin 2000] is used as a benchmark. It provides solutions for the temperature and solid fraction during directional solidification of a 10 cm long Al-7 wt.% Si ingot. The melt, with initial uniform temperature, is cooled with a heat exchange coefficient (assuming a Fourier boundary condition) from one side, the other side being adiabatic. All values for alloy properties, initial and boundary conditions and numerical parameters are listed in table 3.2. For this simple test case, we use linear temperature dependence of the intrinsic phase enthalpies, that is  $\langle \rho h \rangle^s = \langle \rho C_p \rangle T$  and  $\langle \rho h \rangle^l = \langle \rho C_p \rangle T + \rho L$ , where  $\langle \rho C_p \rangle$  is the heat capacity per unit volume and  $\rho L$  is the latent heat per unit volume. Values for  $\langle \rho C_p \rangle$  and  $\rho L$ , as well as for the thermal conductivities,  $\kappa = \langle \kappa^l \rangle = \langle \kappa^s \rangle$ , are taken constant. Moreover, a Gulliver Scheil approximation is used to compute a single temperature – fraction of solid relationship in the absence of macrosegregation. This is done assuming a linear binary phase diagram and thus requires using the properties listed in table 3.2, i.e. the segregation coefficient,  $k$ , the liquidus slope,  $m_L$ , the liquidus temperature,  $T_L$ , and the eutectic temperature,  $T_E$ . Figure 3.5 show

### Chapter 3. Energy balance with thermodynamic tabulations

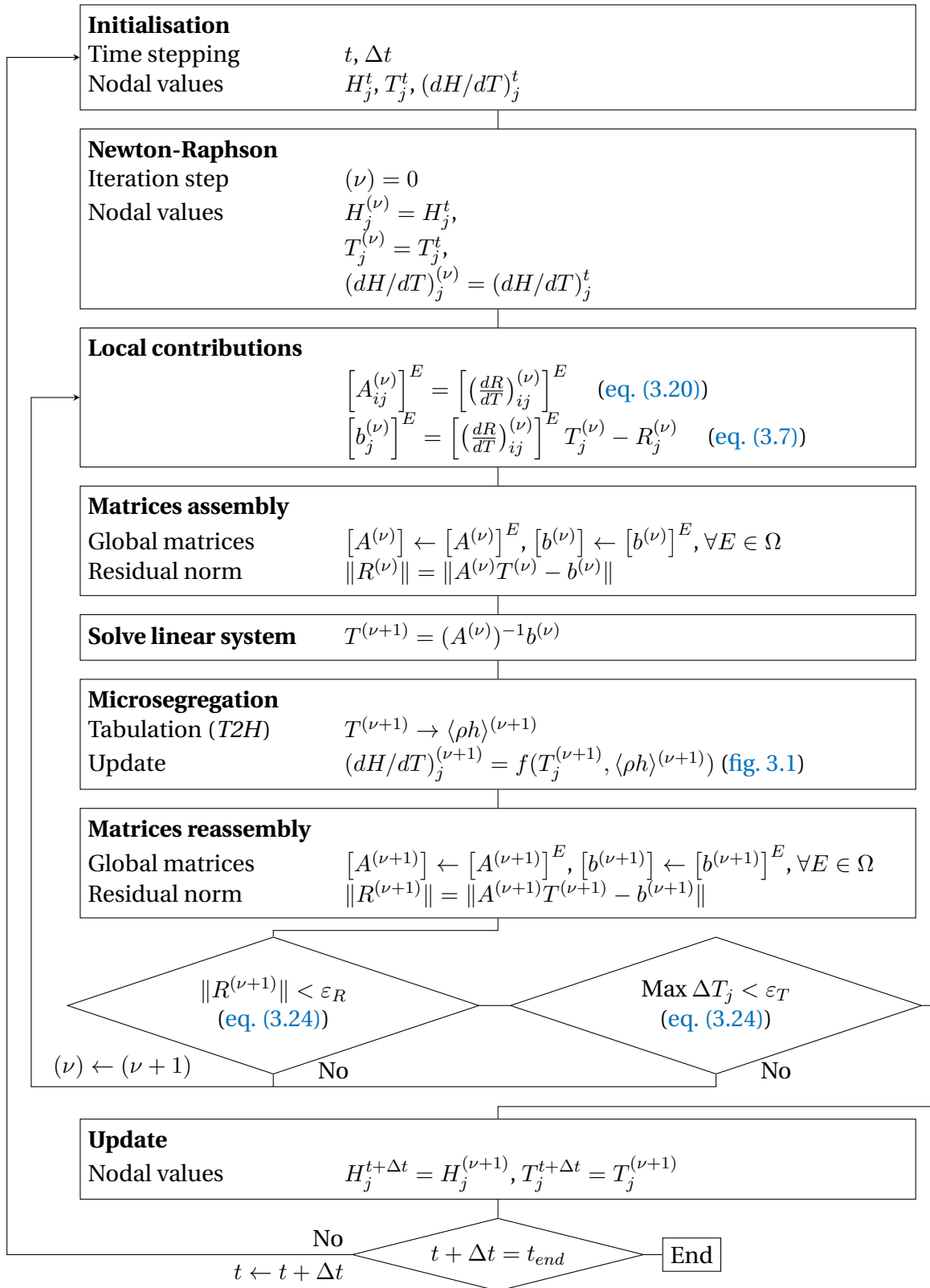


Fig. 3.3 – Resolution algorithm of the temperature-based solver.

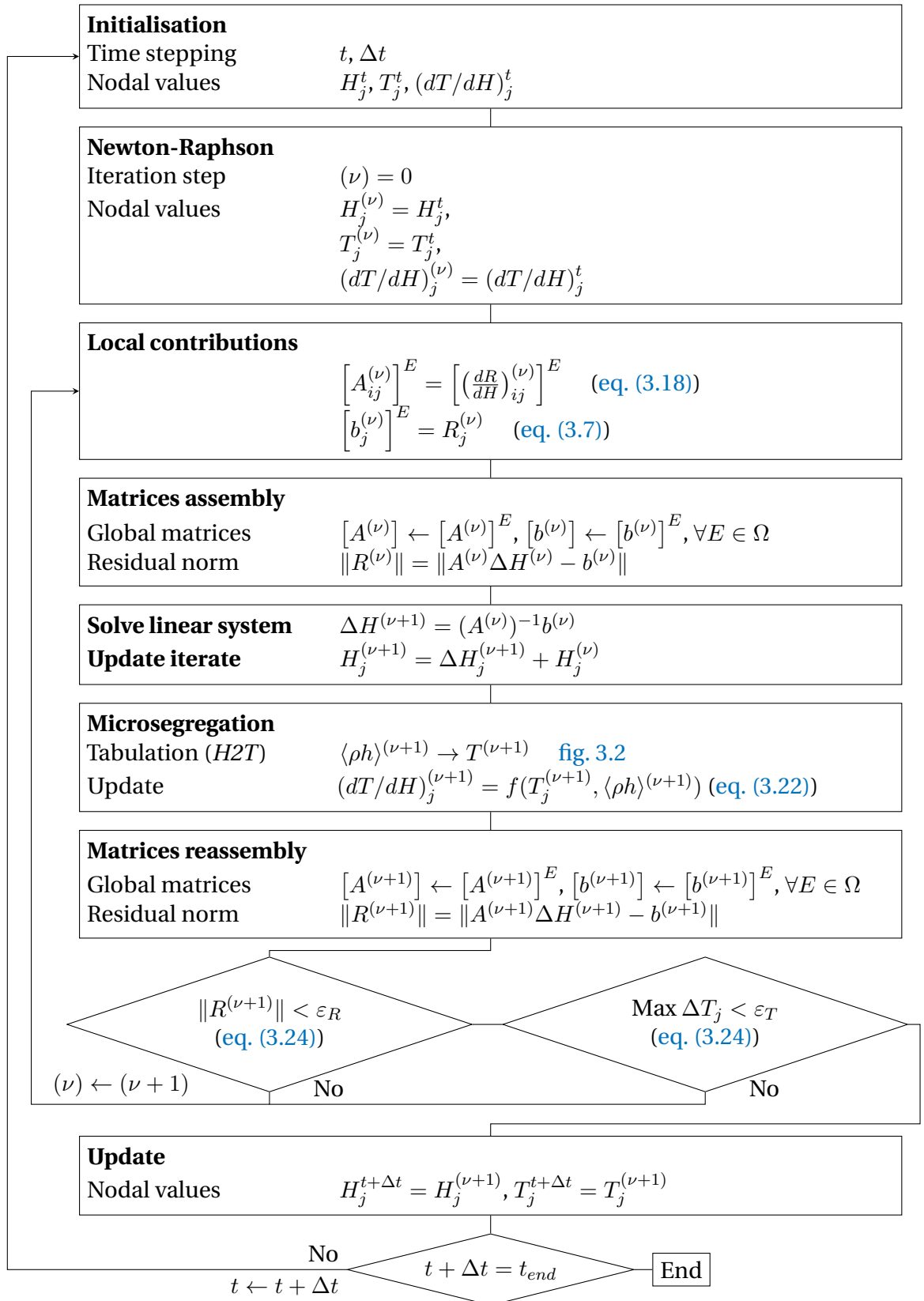


Fig. 3.4 – Resolution algorithm of the enthalpy-based solver.

### Chapter 3. Energy balance with thermodynamic tabulations

---

the comparison with the Hsolver and Tsolver. The cooling curves and liquid fraction results are found superimposed to the front tracking solution, thus giving validation of the implementation as well as the iterative schemes presented above to solve the energy conservation

**Table 3.2** – Parameters for the pure diffusion test case with an Al-7 wt.% Si alloy presented in [fig. 3.5](#)

Parameter	Symbol	Value	Unit
Nominal composition	$\langle w \rangle_0$	7	wt.%
Liquidus temperature	$T_l$	618	°C
Eutectic temperature	$T_E$	577	°C
Segregation coefficient	$k$	0.13	—
Liquidus slope	$m_l$	-6.5	K wt.% <sup>-1</sup>
Heat capacity (liquid and solid)	$\rho C_p$	$2.6 \times 10^6$	J m <sup>-3</sup> K <sup>-1</sup>
Enthalpy of fusion	$\rho L$	$9.5 \times 10^8$	J m <sup>-3</sup>
Thermal conductivity (liquid and solid)	$\kappa$	70	W m <sup>-1</sup> K <sup>-1</sup>
Heat transfer coefficient	$h_{\text{ext}}$	500	W m <sup>-2</sup> K <sup>-1</sup>
External temperature	$T_{\text{ext}}$	100	°C
Initial temperature	$T_0$	800	°C
Ingot length		0.1	m
FE mesh size		$10^{-3}$	m
Time step	$\Delta t$	0.1	s
Convergence criterion (residual)	$\varepsilon_R$	$10^{-6}$	—
Convergence criterion (temperature)	$\varepsilon_T$	$10^{-2}$	K

#### 3.4.2 Convection and diffusion

To validate the Tsolver with fluid flow, we consider the following set of equations already defined in the flowchart of [section 2.1.4](#). Moreover, an assumption of a static and non deformable solid phase is made. Consequently, the mechanical model is reduced to the conservation of momentum in the liquid phase. This assumption also yields some other consequences on the mass balance and the liquid momentum conservation. In the latter, a Darcy term is added to take into account the dissipative interfacial stress in the porous-like mushy zone. Its main parameter is the permeability of the mushy zone,  $K$ . It is considered isotropic, hence reducing to a scalar which is given by the Carman-Kozeny relation, based on the secondary dendrite arm spacing  $\lambda_2$  :  $K = \frac{g^{l^3} \lambda_2^2}{180(1-g^l)^2}$ . The liquid density being taken constant, its spatial variations as a function of temperature and average composition are still needed to compute

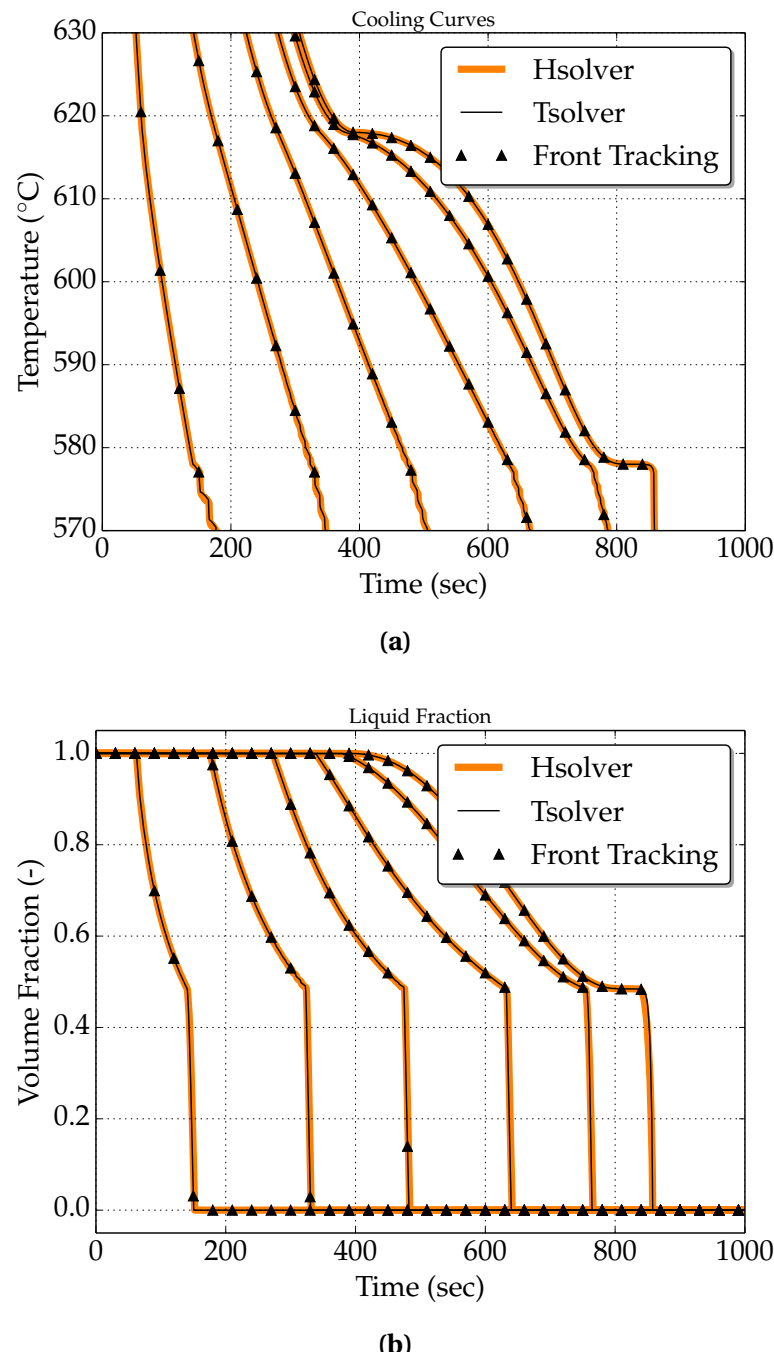


**Fig. 3.5** – Computed unidirectional heat diffusion during solidification of an Al-7 wt.% Si alloy using (orange) the enthalpy method and (black) the temperature method, comparison being made for (a) cooling curves and (b) the liquid fraction history. Each curve corresponds to a position along the sample, from 0 cm (cooling side) to 10 cm (insulated side), with 2 cm spacing between the positions.

thermosolutal convection forces. For that purpose, the Boussinesq approximation  $\rho^l = \rho_0^l \left( 1 - \beta_T (T - T_0) - \beta_{\langle w \rangle^l} (\langle w \rangle^l - w_0^l) \right)$  is used, considering the thermal  $\beta_T$  and solutal  $\beta_{\langle w \rangle^l}$  expansion coefficients and a reference density,  $\rho_{ref}$ , defined at a reference temperature  $T_0$  and reference composition  $w_0^l$ . Values for the references are taken at the liquidus temperature and the nominal composition of the alloy,  $\langle w \rangle_0$  [Carozzani et al. 2013]. More details about the FE formulation can be found in the PhD work of Rivaux [2011] and Carozzani [2012]. The Tsolver's ability to be coupled with vari-

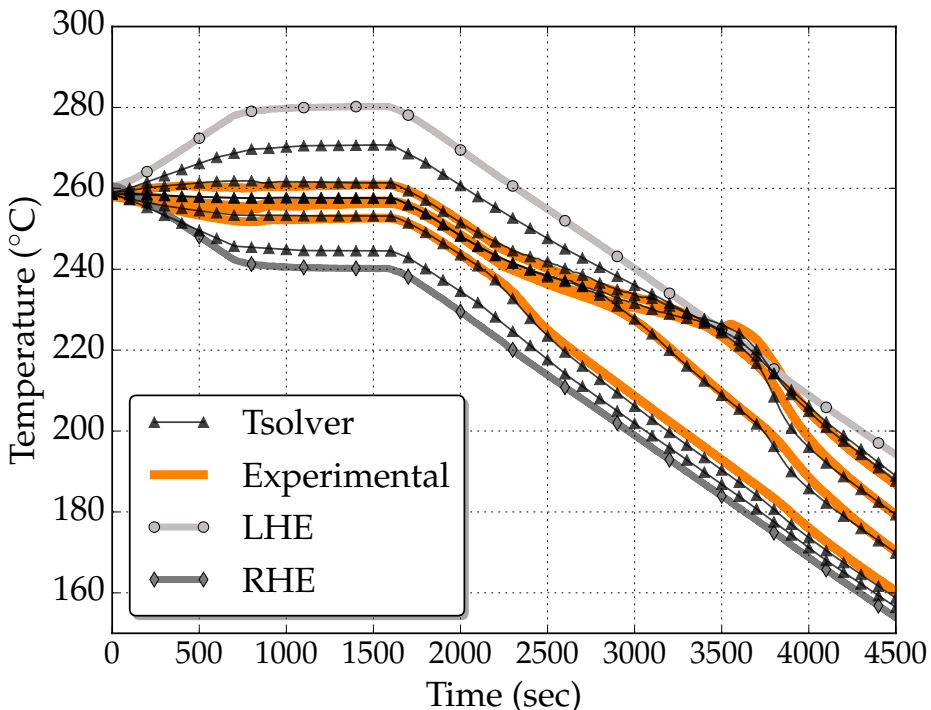


**Fig. 3.6** – Experimental cooling curves overlap with the results of the 3D FE convection-diffusion simulation. The left (LHE) and right (RHE) heat exchangers impose the boundary temperature in the experiment.

ous physical phenomena like macrosegregation and fluid flow in porous medium is displayed in this test case. Details about fluid flow resolution will not be given in this section, but rather in the next chapter. It consists of a solidification benchmark where a 10 cm width  $\times$  6 cm height  $\times$  1 cm thick cavity containing a Sn-3 wt.% Pb melt is cooled down from its two narrowest vertical sides using heat exchangers (LHE: left heat exchanger, RHE: right heat exchanger). The experiment, inspired by Hebditch et al. [1974] similar set up, has been revisited by Hachani et al. [2012] who performed the solidification with better controlled conditions and using an increased number of samples for composition analysis. Recently, a successful attempt to simulate the experiment was carried out by Carozzani et al. [2013] relying on an enthalpy resolution. All details regarding geometry, finite element discretization, material properties

and boundary conditions can be found in the latter reference. For this computation, solidification paths, phase compositions and phase enthalpies were determined by a thermodynamic module dedicated to equilibrium calculations for binary alloys. The 3D simulation results in [fig. 3.6](#) show a satisfactory agreement with the experimental temperature measurements recorded at mid heights of the cavity and uniformly distributed along its width [Carozzani et al. 2013]. In fact, simulation results with the Tsolver and the Hsolver were found to be almost superimposed, as shows [fig. 3.6](#). Further comparison is made between both solvers, as shows [fig. 3.7](#), where the average composition, liquid fraction and temperature fields are extracted from a cut plane halfway through the ingot. On the same figure, if we compare the composition, we notice that the solidified part (right side) has basically the same segregation pattern, while in the convected liquid has a slightly different solute distribution. As for the extent of the mushy zone, we observe that liquid fraction contours are very close, indicating that temperature distributions and interdendritic segregation are also close between both solvers predictions. Regarding the computation, the Tsolver resolution proves to be faster than the Hsolver used by Carozzani et al. [2013]: a process time of 7000s required a computation time of 90 hours 13 minutes compared to 114 hours 21 minutes spent by the enthalpy resolution with 32 cores on the same cluster. The gain factor is about 20%.

### 3.5 Application: multicomponent alloy solidification

We have shown that the efficiency of the temperature-based resolution resides in its performance when combined with thermodynamic tabulations. A multicomponent alloy consists of at least two solute elements, and therefore the tabulation size increases, hence the number of search operations also increases. To demonstrate the speed-up ability of the temperature-based approach while predicting all phase transformations during macrosegregation caused solely by mass diffusion, we consider the solidification of a ternary alloy, Fe-2 wt.% C-30 wt.% Cr. In order to neglect fluid flow resolution, we assume that solidification in this case is so slow that no forces are generated inside the melt, while additionally all buoyancy forces are also neglected, so no momentum conservation is solved in this section. As illustrated in [fig. 3.9a](#), the alloy domain has a cylinder shape close to 3-inch height  $\times$  1-inch diameter. Exact values are reported in [table 3.3](#) with all material properties, initial and boundary conditions, as well as numerical parameters for the simulations. The melt steel is initially at 1395 °C. The temperature of the bottom surface is imposed with a constant decreasing rate of 0.1 K s<sup>-1</sup> starting with 1380 °C, i.e. 40 °C higher than the nominal liquidus temperature, as shown in [fig. 3.9b](#). The other surfaces are kept adiabatic. The cylinder is held in a vertical position. [fig. 3.8](#) also provides the transformation path of the alloy at nominal composition, i.e. assuming no macrosegregation and full thermodynamic equilibrium

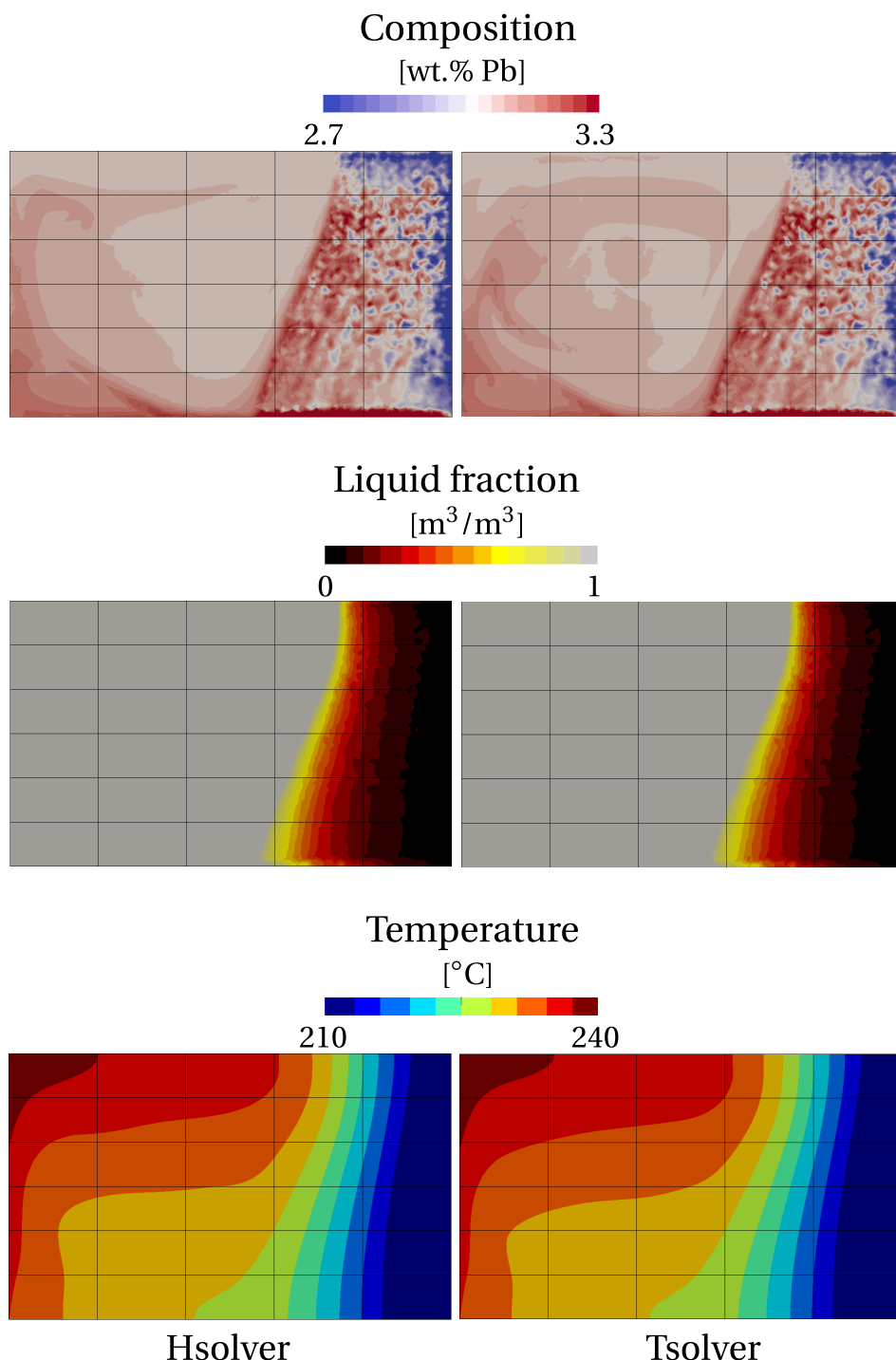


**Fig. 3.7** – Comparison of 3D simulation results: average composition, liquid fraction and temperature at  $t=3000$  s for Tsolver and Hsolver.

as computed with ThermoCalc and the TCFE6 database [TCFE6 2010; Andersson et al. 2002]. A total of 5 phases need to be handled, the characteristic temperature for their formation being reported in fig. 3.9b.

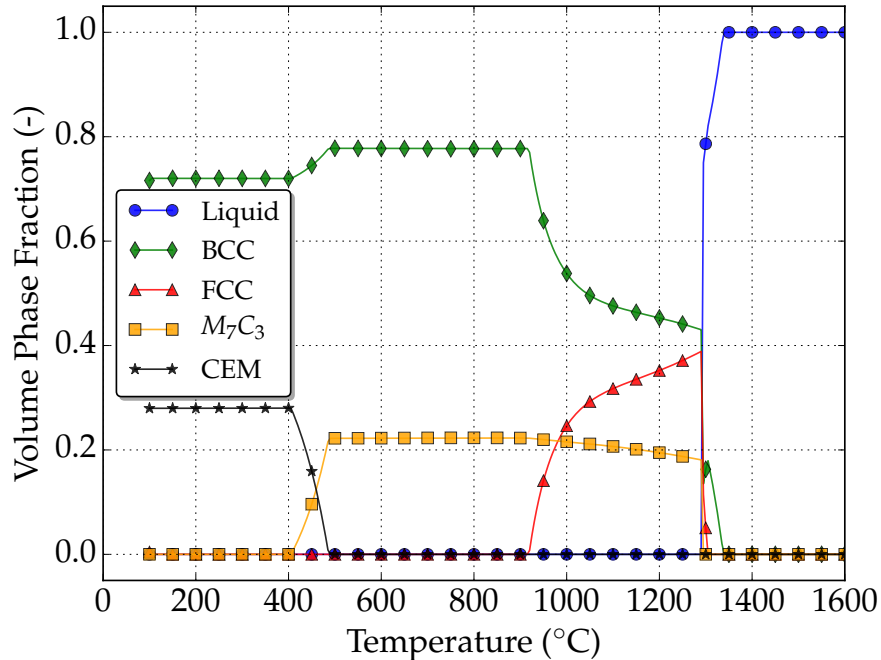


**Fig. 3.8** – Thermodynamic mapping [TCFE6 2010; Andersson et al. 2002] of the transformation path for the Fe-2 wt.% C-30 wt.% Cr at nominal composition.

### 3.5.1 Tabulations

Full thermodynamic equilibrium is considered in the present case. Due to macrosegregation, the average composition is expected to continuously vary in time and space during casting. Transformation paths are thus determined a priori for a set of average compositions around the nominal value. Hence, carbon content varies in the interval [1.8 wt.%, 2.2 wt.%] while chromium content variation is in the interval [27 wt.%, 33 wt.%]. The offset of  $\pm 10\%$  with respect to the nominal composition value allows tabulating relatively small composition steps to ensure a fairly accurate mapping when compared to the corresponding ternary phase diagram. The average composition step is 0.04 wt.% for carbon and 0.6 wt.% for chromium, thus representing 2% intervals with respect to the nominal composition. The temperature varies in the interval [100 °C, 1600 °C] by 5 °C steps. For each triplet (carbon content in wt.% C,  $\langle w_C \rangle_0$ , chromium content in wt.% Cr,  $\langle w_{Cr} \rangle_0$ , temperature in K) corresponds a phase fraction  $g^\phi$  and a pair of intrinsic phase composition ( $\langle w_{Cr} \rangle^\phi, \langle w_C \rangle^\phi$ ). For the 5 phases listed in fig. 3.8 (LIQ=liquid, BCC=ferrite, FCC=austenite, M<sub>7</sub>C<sub>3</sub>=carbide, CEM=cementite), the enthalpy  $h^\phi$  and density  $\rho^\phi$ , are tabulated as functions of temperature and phase intrinsic

composition. If this latter input lies between two tabulated values, a linear interpolation is performed to determine the output, i.e. phase enthalpy and density. With the advancement of solidification, the liquid is enriched with solute by macrosegregation, which enables new solidification paths. It means that the primary solidifying phase is not necessarily the same as when considering the nominal composition. For this reason, the tabulation approach is interesting inasmuch as it provides phase transformation paths and values of phase properties that are compatible with the system's actual composition. [Figure 3.10](#) summarizes the tabulated thermodynamic data for two sets of average composition for the considered ternary system. Note that in the present test case, phase densities are taken constant ( $\rho^s = \rho^l = 6725 \text{ kg m}^{-3}$ ). Therefore they are not tabulated. With this assumption, no shrinkage occurs upon phase change.

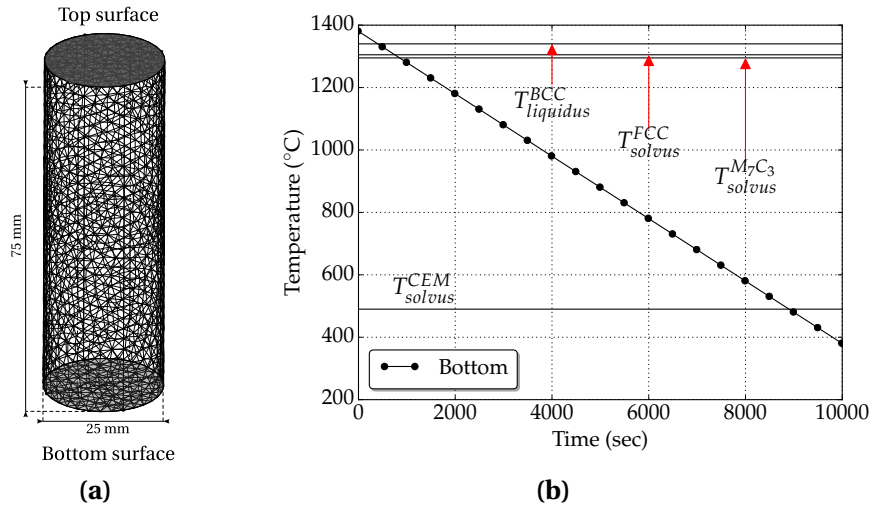


**Fig. 3.9** – Configurations for directional casting of (a) a 1 inch diameter  $\times$  3 inches height cylindrical domain for which (b) temperature-time conditions are imposed at its bottom surface.

### 3.5.2 Discussion

A first case is considered without macrosegregation, that is, all mechanical driving forces are bypassed, leading to a static melt. This is achieved by nullifying the thermal and solutal expansion coefficients, which is equivalent to a constant density in space and time, i.e. no Boussinesq force is considered. This way, the average composition may only vary due to diffusion in the liquid phase according to [eq. \(2.46\)](#) where the convection term is neglected. Diffusion is significantly small in the present case and can be neglected too. In such a case, the composition distribution maintains a homogeneous aspect throughout the sample during the entire cooling sequence. The phase transformations then are necessarily expected to follow the unique path shown in [fig. 3.8](#). After 407 s of cooling, the liquidus isotherm enters the bottom surface of

### 3.5. Application: multicomponent alloy solidification

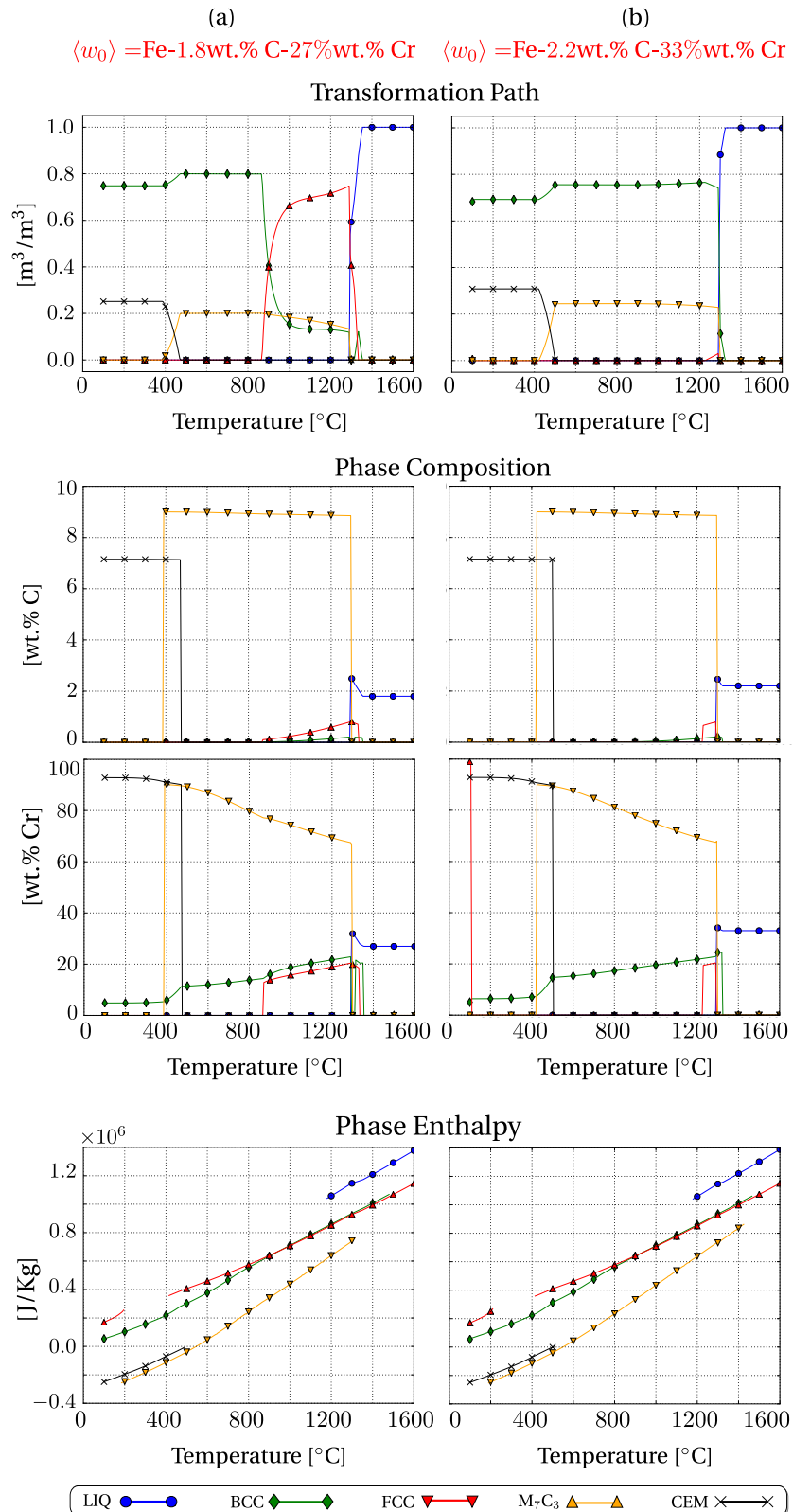


**Fig. 3.10** – Tabulated thermodynamic data for the ternary system Fe-C-Cr alloy with software Thermo-Calc [Andersson et al. 2002] with database TCFE6 [TCFE6 2010]. The two columns represent two values of nominal average composition, for a) low carbon and chromium content and b) high carbon and chromium content. The effect of their variation on transformation paths, phase compositions and phase enthalpies is shown in the corresponding graphs.

### Chapter 3. Energy balance with thermodynamic tabulations

---

the geometry and starts its upward propagation, marking the solidification onset. [Figure 3.11](#) presents the simulation results at 3 successive times for the distribution of the solute species and the temperature, as well as for the fraction of phases listed in [fig. 3.8](#). At 600 s, a fully liquid region is still largely present while the mushy zone is made of liquid plus the primary solid phase (ferrite). At 10 560 s, the sample is full solid, with fractions of ferrite and cementite that corresponds to the values read in [fig. 3.8](#) at low temperature. At the selected intermediate time, the presence of 4 phases is found. The solid region at the bottom of the cylinder is made of ferrite, austenite plus carbide, the temperature being still too high to permit the cementite to form. The mushy zone above the solid region is characterized by the presence of 3 phases due to a peritectic reaction taking place that progressively transform ferrite into austenite in the presence of liquid. It can be noticed that the phase fraction isovalues in [fig. 3.11](#) (at 600 s) are horizontal, owing this to two factors: the first is the temperature field, which varies unidirectionally from bottom to top, controlled by thermal diffusion, while the second is the uniform average composition throughout the sample due to the absence of convection. In fact both factors are consequences of the flow absence, which would transport heat and solute by advection, thus inevitably changing the phase distribution. The succeeding phase change is a solid-state transformation where  $\alpha$ -ferrite and the carbide  $M_7C_3$  react to form cementite at 490 °C at nominal composition, as shown in [fig. 3.9b](#). The reaction is relatively slow, ending with 28% of cementite and 72% of  $\alpha$ -ferrite.

### 3.5. Application: multicomponent alloy solidification

**Table 3.3** – Solidification parameters for the Fe-2 wt.% C-30 wt.% Cr alloy.

Parameter	Symbol	Value	Unit
Nominal composition	$\langle w_C \rangle_0$	2	wt.%
	$\langle w_{Cr} \rangle_0$	30	wt.%
Characteristic temperatures	$T_{\text{bottom}}$	<a href="#">fig. 3.9b</a>	°C
Phase fraction	$g^\phi$	Tabulations <a href="#">fig. 3.10</a>	–
Phase enthalpy	$\langle h \rangle^\phi$	Tabulations <a href="#">fig. 3.10</a>	–
Phase composition	$\langle w_C \rangle^\phi$	Tabulations <a href="#">fig. 3.10</a>	wt.%
Phase composition	$\langle w_{Cr} \rangle^\phi$	Tabulations <a href="#">fig. 3.10</a>	wt.%
Diffusion coefficients	$\langle D_C \rangle^l$	$15 \times 10^{-10}$	$\text{m}^2 \text{s}^{-1}$
	$\langle D_{Cr} \rangle^l$	$15 \times 10^{-10}$	$\text{m}^2 \text{s}^{-1}$
Dynamic viscosity	$\mu^l$	$2 \times 10^{-3}$	Pa s
Thermal expansion coefficient	$\beta_T$	$8.96 \times 10^{-5}$	$\text{K}^{-1}$
Solutal expansion coefficient	$\beta_{\langle w_C \rangle^l}$	$1.54 \times 10^{-3}$	$\text{wt.\%}^{-1}$
	$\beta_{\langle w_{Cr} \rangle^l}$	$1.72 \times 10^{-2}$	$\text{wt.\%}^{-1}$
Thermal conductivity in the solid	$\langle \kappa^s \rangle$	40	$\text{W m}^{-1} \text{K}^{-1}$
Thermal conductivity in the liquid	$\langle \kappa^l \rangle$	28	$\text{W m}^{-1} \text{K}^{-1}$
Dendrite arm spacing	$\lambda$	$60 \times 10^{-6}$	m
Density	$\rho_0^l$	6725	$\text{kg m}^{-3}$
Reference composition (carbon)	$\langle w_C \rangle_{\text{ref}}^l$	2	wt.%
Reference composition (chromium)	$\langle w_{Cr} \rangle_{\text{ref}}^l$	30	wt.%
Reference temperature	$\langle w_C \rangle_{\text{ref}}^l$	1377	°C
Initial temperature	$T_0$	1395	°C
Ingot diameter		$25 \times 10^{-3}$	m
Ingot length		$75 \times 10^{-3}$	m
FE mesh size		$10^{-3}$	m
Time step	$\Delta t$	0.1	s
Convergence criterion (residual)	$\varepsilon_R$	$10^{-6}$	–
Convergence criterion (temperature)	$\varepsilon_T$	$10^{-2}$	K

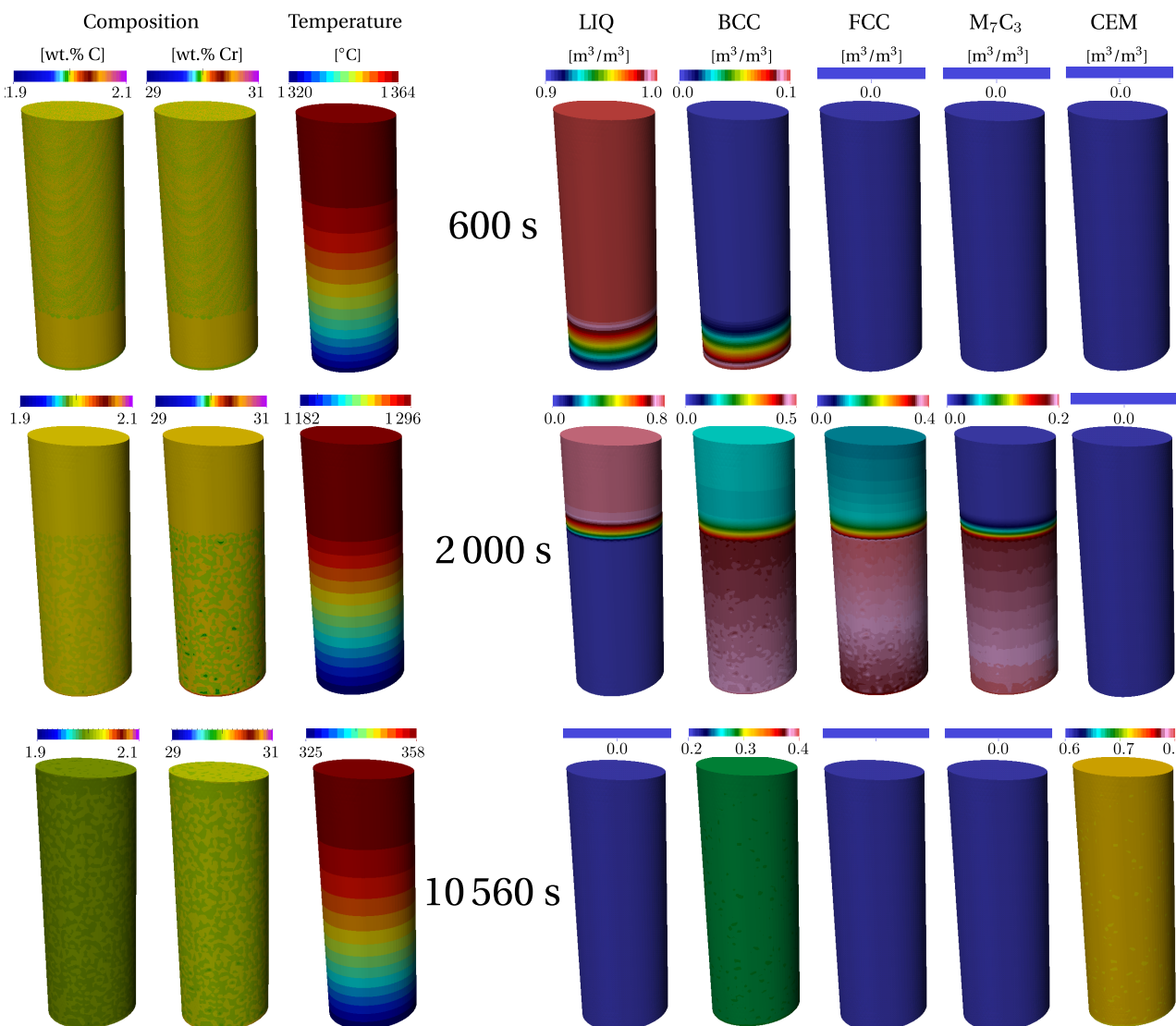


**Fig. 3.11 – :** Upward solidification of a cylinder rod with a static liquid at 3 stages in a Fe-2 wt.% C-30 wt.% Cr. The left columns show the average composition and temperature distribution, while the right columns show the phase fractions.

## Chapter 4

# Macrosegregation with liquid metal motion

### Contents

---

<b>4.1</b>	<b>Introduction</b>	<b>64</b>
<b>4.2</b>	<b>Numerical treatment</b>	<b>64</b>
4.2.1	Stable mixed finite elements	64
4.2.2	Variational multiscale (VMS)	64
<b>4.3</b>	<b>VMS solver</b>	<b>65</b>
<b>4.4</b>	<b>Computational stability</b>	<b>66</b>
4.4.1	CFL condition	66
4.4.2	Integration order	66
<b>4.5</b>	<b>Application to multicomponent alloys</b>	<b>66</b>
4.5.1	Results	68
<b>4.6</b>	<b>Macroscopic freckle prediction</b>	<b>69</b>
4.6.1	Introduction	71
4.6.2	Experimental work	72
4.6.3	Macroscopic scale simulations	72
<b>4.7</b>	<b>Meso-Macro freckle prediction</b>	<b>79</b>
4.7.1	Numerical method	79
4.7.2	Configuration	81
4.7.3	Effect of vertical temperature gradient	84
4.7.4	Effect of cooling rate	86
4.7.5	Effect of lateral temperature gradient	88

---

## 4.1 Introduction

Fluid flow is an important part, if not the most important, in understanding the evolution of a system undergoing phase change and chemical segregation. It is attributed to the convective transport in fluids where the variations time scale is much smaller than the remaining physics that are characterized by smoother variations. To understand how fluid motion contributes to the heat and mass transfer, we have swiftly presented the momentum conservation equation in a solidifying liquid, [eq. \(2.44\)](#). In this chapter, we will first give quick overview of the numerical treatment of this system of Navier-Stokes equations, then comment on some computational aspects such as the choice of a suitable time step and the conditions that impose minimum and maximum bounds on both time step and mesh size.

## 4.2 Numerical treatment

As for any computational domain, we have a wide array of numerical methods that help solving systems of equations like [eq. \(2.44\)](#). When speaking about Navier-Stokes equations the choice can be narrowed to two basic approaches with some similarities: Stabilised finite element method and Variational MultiScale (VMS). These approaches are different from a classical finite element approach by introducing additional degrees freedom then eliminating them in a way to satisfy a crucial set of conditions which guarantee the famous *Inf-Sup* condition stemming from the Lax-Milgram theorem.

### 4.2.1 Stable mixed finite elements

First introduced by [Arnold et al. \[1984\]](#), the MINI element is the key ingredient in this approach. For equal order velocity and pressure P1-approximation, the Inf-Sup condition is not satisfied unless the velocity has an additional degree of freedom, the bubble, which vanishes on the element's boundary. We may thus speak of a P1+/P1 element in velocity-pressure formulation. The P1+/P1 approach has been the de facto standard for solving fluid and solid mechanics for some years in CEMEF.

### 4.2.2 Variational multiscale (VMS)

As the name indicates, this approach considers two scales of phenomena: the coarse and fine scales. Applied to a velocity-pressure formulation, these fields are decom-

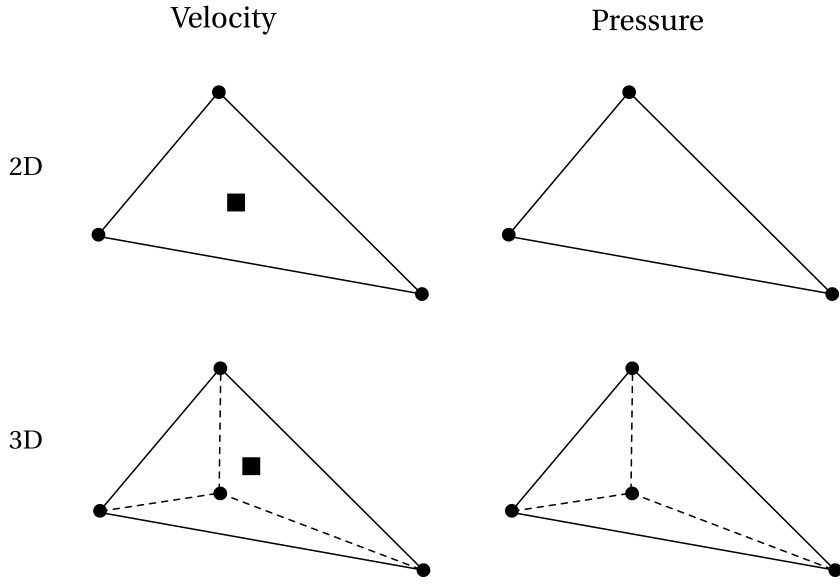


**Fig. 4.1** – Schematic of 2D and 3D stable P1+/P1 finite elements, respectively triangle and tetrahedron, with velocity and pressure fields interpolation order. The dots represent the nodal values while the square represents the bubble.

posed according to these scales as follows:

$$\langle \vec{v}^l \rangle = \langle \vec{v}^l \rangle_h + \tilde{\vec{v}}^l \quad (4.1)$$

$$p = p_h + \tilde{p} \quad (4.2)$$

where  $\langle \vec{v}^l \rangle_h$  and  $p_h$  are the coarse scale velocity and pressure discretised on the finite element mesh (hence the subscript  $h$ ), while the remaining terms represent the fine scale velocity and pressure that cannot be captured at the scale of the FE grid. Instead of defining a finer grid to model the effect of these terms, one can solve the fine scale equations obtained once eqs. (4.1) and (4.2) are injected in eq. (2.44) then use the output in the coarse scale equations. Further technical details about the method and the equations are found in the PhD work of Hachem [2009]. The added value of the VMS method is the time gain that we get by incorporating the effect of the fine scale into the coarse scale physics without discretising on a finer grid, while maintaining the ability to predict localised fluid motion such as small vortices.

### 4.3 VMS solver

In the present thesis, we chose to solve the fluid momentum conservation using the VMS approach. The VMS solver developed by Hachem et al. [2010] is a convenience choice to solve Navier-Stokes with Darcy terms while at the same time have convection stabilisation terms, such as the well known Streamline Upwind Petrov-Galerkin (SUPG)

and Shock Capturing Petrov-Galerkin (SCPG) stabilisation techniques for convection-dominated problems.

### 4.4 Computational stability

#### 4.4.1 CFL condition

#### 4.4.2 Integration order

Using P1 linear elements implies a P2 integration ? what are the advantages (time) and limitations ?

### 4.5 Application to multicomponent alloys

In the previous chapter, we have considered a static melt upon solidification of multi-component alloy. The artificial consideration of a still flow is dropped in this chapter, hence taking into account macrosegregation caused by fluid motion, using realistic values of the expansion coefficients given in [table 3.3](#). In the real conditions, the melt is in constant motion and knowing that the carbon and chromium solutes have lightening effects on the liquid at nominal composition, the density inversion resulting from the composition gradient in the interdendritic liquid, may cause flow instability (segregation plumes) at the solidification front. While the selected alloy is a steel, this application is also representative of directional cooling in a single crystal casting, e.g. for nickel-base superalloys [[Beckermann et al. 2000](#)]. Solidification of this class of alloys is carefully controlled so as to prevent any freckle-type defect to exist in the as-cast state. In this section, we consider the same simulation parameters defined in [table 3.3](#) as well the geometry and thermal boundary conditions previously defined in [fig. 3.9](#). Moreover, we solve the liquid momentum conservation equation, with non-slip boundary conditions on all external sides of the cylinder.

#### 4.5. Application to multicomponent alloys

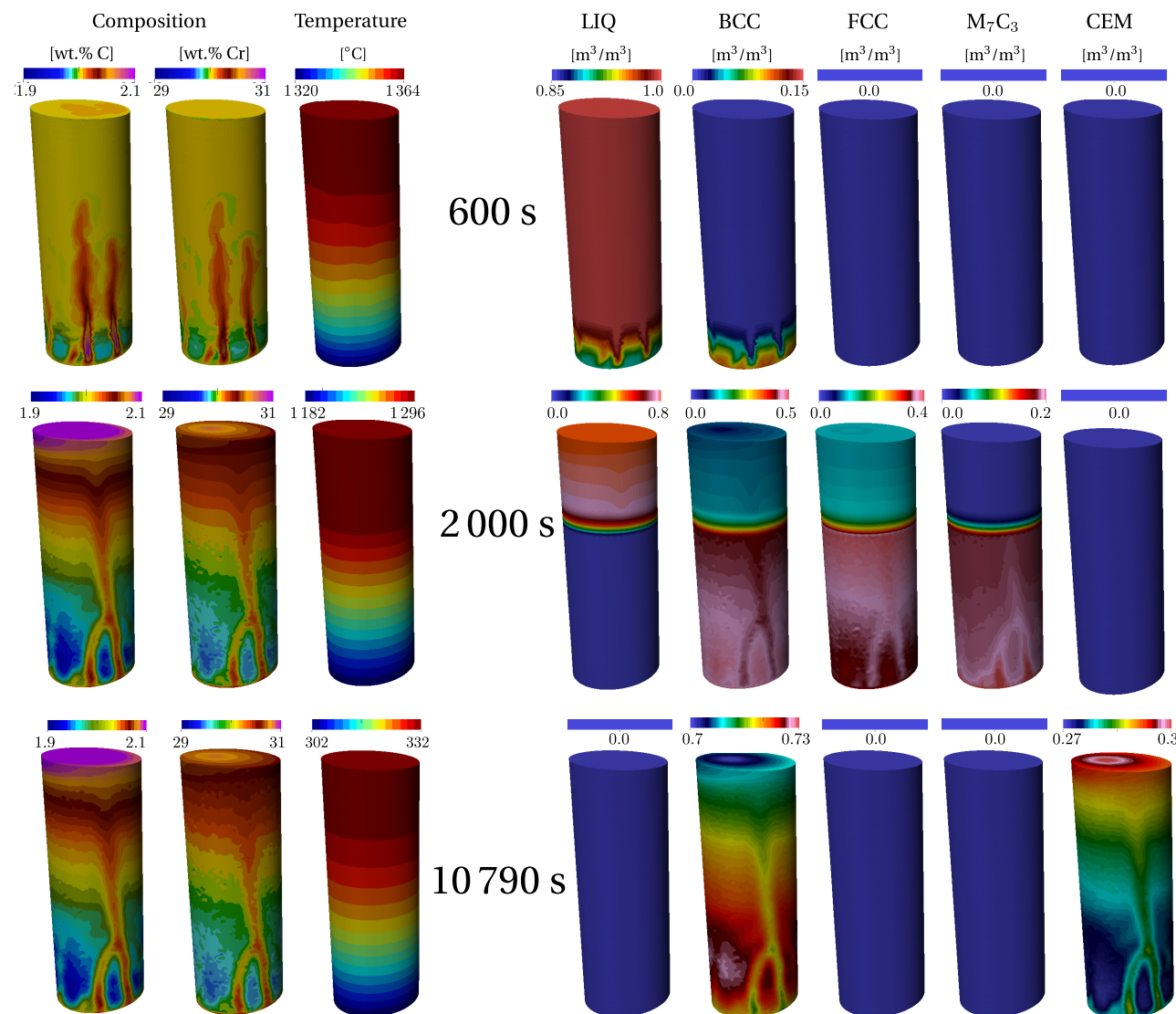


**Fig. 4.2 –**: Upward solidification of a cylinder rod at 3 stages showing the metallurgical consequences of macrosegregation Fe-2 wt.% C-30 wt.% Cr. The left columns show the average composition and temperature distribution, while the right columns show the phase fractions.

### 4.5.1 Results

Solidification starts at 407 seconds when the cylinder's bottom base temperature reaches the liquidus temperature of the alloy. In fact, the solidification onset is the same as in the pure diffusion case in [fig. 3.11](#), since the average composition remains unchanged for an entirely liquid domain (assuming an initially infinite solute mixing in the melt). As shown in [fig. 4.2](#) at 600 s, the first solid phase to form remains ferrite. We can also see solute-rich channels forming in the mushy zone and solute plumes rising in the melt above the mushy zone due to a subsequent upward flow. It is actually caused by the thermosolutal buoyancy force created by the carbon and chromium solutes. Such phenomenon could delay solidification inside liquid-rich channels and results in a freckling defect [[Felicelli et al. 1991](#)] on the surface of the cylinder as well as inside, as shown later in this section. As solidification proceeds, the liquid becomes more enriched with solute and the peritectic reaction forming the austenite phase is reached. However, for very large enriched melt, it can also be observed that primary solidification proceeds with the austenite phase rather than the ferrite phase. The carbide phase can also form with the austenite phase at some locations. These observations correspond to a simulation time of 2000 s in [fig. 4.2](#). Solidification ends at around 2475 s, the last liquid solidifying at the cylinder's top surface, where the average composition reaches a maximum of Fe-2.151 wt.% C-30.633 wt.% Cr, i.e. a relative positive macrosegregation,  $(\langle w_i \rangle - \langle w_i \rangle_0) / \langle w_i \rangle_0$ , of 7.5% for carbon and 2.1% for chromium. The fact that the maximum average composition is observed at the top, is verified in [fig. 4.3a](#) which shows the composition map in a 2D vertical slice through the longitudinal axis of the cylinder. We can also see it in [fig. 4.3b](#) where the relative composition profile are plotted at the end of the cooling process along the longitudinal cylinder axis Z-Z' and along the axis of the freckle, F-F'. The negative segregation up to 1 cm from the chill corresponds to the solute depletion caused by the first solid formation. The subsequent solidification enriches further the liquid; hence the solid composition also increases. The composition evolution trend for both solutes is similar: an overall rise until positive segregation is achieved above 5 cm from the chill. The positive macrosegregation intensifies when the profile is chosen at the center of the freckle, negative segregation then becoming less pronounced. Beyond 2475 seconds, no variations of the average composition maps are observed since solute diffusion in the solid phases is neglected. Nonetheless, as temperature decreases, solid-state transformations are still possible as for the case with no macrosegregation. The formation of a cementite phase begins at the cylinder base at 8843 s with a temperature of 496.9 °C. At about 9293 s, the isotherm 488.5 °C reaches the top surface. This temperature value is the local cementite solvus temperature. The difference in the solvus temperature between the bottom and top surfaces is due macrosegregation. Macrosegregation also explains the variation in the cementite content. The solid state transformation ends shortly before 10 500 s. The final phase distribution is clearly de-

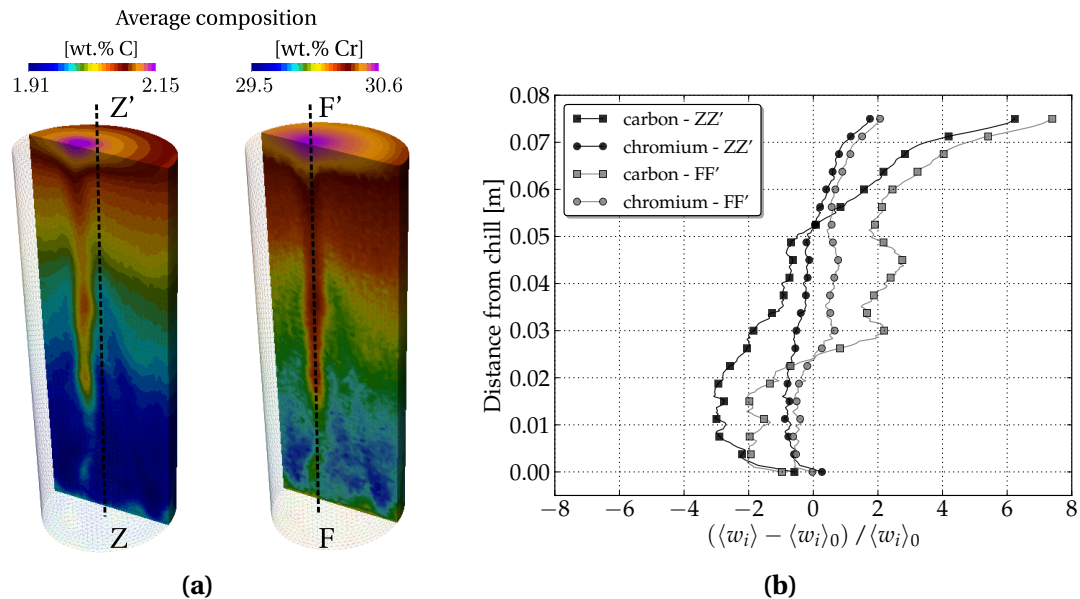
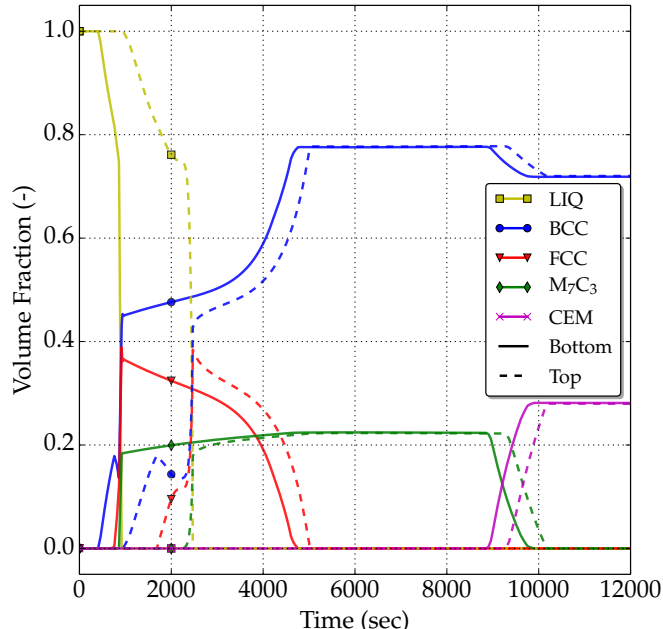


**Fig. 4.3** – (a) average composition map on a vertical section inside the sample, with (b) relative macrosegregation profiles on the vertical revolution axis.

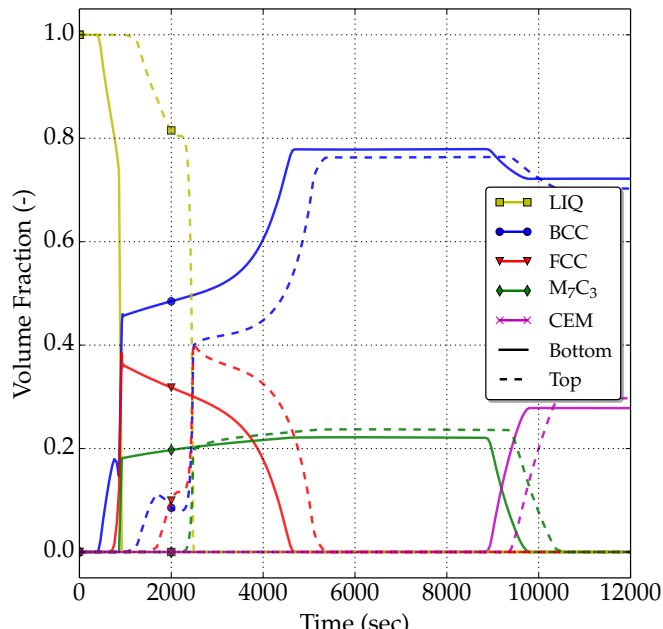
pendent on the final macrosegregation pattern. They retain the shape of the freckles that were caused by thermosolutal convection, hence demonstrating the influence of the solidification process on the final phase distribution. This is better illustrated by drawing the time evolution of phase fractions at the center of the bottom and top surfaces of the cylinder in [fig. 4.4a](#). With no macrosegregation, in [fig. 4.4a](#), the final distribution of the phases is the same at time 12 000 s, while with macrosegregation, in [fig. 4.4b](#), variations of the cementite and ferrite are revealed. The previously mentioned segregation plumes have transformed to freckles, inside the cylinder and on the boundary. This defect is marked by a noticeable gradient of composition and phase fractions, possibly changing the mechanical properties in the channels, hence the overall mechanical behavior of the alloy [[Copley et al. 1970](#)]. The coupling of the Tsolver with thermodynamic tabulations is thus demonstrated. It shows the ability to predict complex solidification paths, even if only at equilibrium. As for the computation time, the Tsolver resolution performed better: 500 seconds of solidification required 6 hours 14 minutes compared to 8 hours 6 minutes spent by the enthalpy resolution with 12 cores on the same machine. The gain factor is about 22%.

## 4.6 Macroscopic freckle prediction

I should maybe mention that a constant gradient in the coming simulation is a one big difference compared to the previous FeCrC simulation



(a)



(b)

**Fig. 4.4** – History of phase fraction (a) without macrosegregation and (b) with macrosegregation at the center of the (plain) bottom and (dashed) top surfaces of the cylinder surfaces, extracted from simulations displayed in (a) [fig. 3.11](#) and (b) [fig. 4.2](#).

### 4.6.1 Introduction

We have seen in the previous multicomponent solidification test case, another form of segregation, the so-called freckle. This defect manifests itself as a composition inhomogeneity that is highly non-isotropic. A typical description of its morphology would consider a channel with a diameter proportional to few primary dendrite arm spacing and a length that could vary from millimeters to centimeters. These “worm”-like shapes could form during directional solidification of cast parts designed for engine applications, particularly in Nickel-base superalloys [Giamei et al. 1970; Beckermann et al. 2000; Genereux et al. 2000; Schneider et al. 1997]. They are also related to A-segregates defects in large steel ingots [Pickering 2013].

Considering a binary alloy with a partition coefficient less than unity and having a negative liquidus slope, freckles may form by the following mechanisms: i) solute partitioning occurs at the scale of dendrite arms and solute is rejected in the melt, ii) local composition gradients are intensified resulting in an increase of the solutal buoyancy force in the mushy zone, iii) solute-rich pools are formed, causing segregation chimneys, iv) which lead to partial remelting of dendrites, continuous solute feeding and locally delayed solidification.

Because it is of prime importance to control the occurrence of freckles, several attempts have been made from the late 1960's [Flemings et al. 1967; Flemings et al. 1968a; Flemings et al. 1968b] to the early 2000's [Ramirez et al. 2003] to understand it and characterize it by deriving freckling criteria. These studies are summarized in [Auburtin 1998]. One of the reasons for only considering freckling criteria is that direct realistic simulations of the formation of freckles in a casting geometry are still difficult. Indeed, experimental observations show that it requires a satisfying description of the microstructure together with the 3D convective flow controlled by the cooling conditions of the complete cast part [Shevchenko et al. 2013]. Such information is not accessible yet. Only simulations in representative simple cuboid or cylindrical domains are usually achieved [Felicelli et al. 1991; Felicelli et al. 1998; Kohler 2008; Guo et al. 2003], except when considering small volume casting [Desbiolles et al. 2003]. They are usually limited to unstable thermosolutal convection without or with little regard to the microstructural features. Considering the spatial resolution of the defect, being for example of the order of the primary dendrite arm spacing, a fluid flow computation in the 3D casting part is also very demanding and not common in the literature. Among other criteria, the dimensionless Rayleigh number has been identified as a good indicator for the occurrence of freckles. The dependence of freckling tendency on the Rayleigh number has been studied numerically and compared to experimental observations, as done by [Ramirez et al. 2003].

### 4.6.2 Experimental work

An interesting experimental work on directional solidification of In-75 wt.% Ga featuring in-situ X-ray monitoring has been recently carried out by [Shevchenko et al. \[2013\]](#). The comparison with numerical modelling is paramount for two main reasons: firstly, the in-situ technique allows to follow solidification in real-time and offers visual description of the system behaviour: grain morphology, composition evolution, effect on fluid flow in the mushy zone and chimney initiation, as well as other modelling input data such as dendritic and eutectic nucleation undercooling; secondly, an indium-gallium system is more representative of metallic alloy solidification than the widely used organic systems, e.g. the succinonitrile-acetone mixture that exhibits alloy-like dendritic formation in its growth stage. Further information with respect to the experimental hardware, procedure and data analysis can be found in [\[Boden et al. 2008; Shevchenko et al. 2013\]](#).

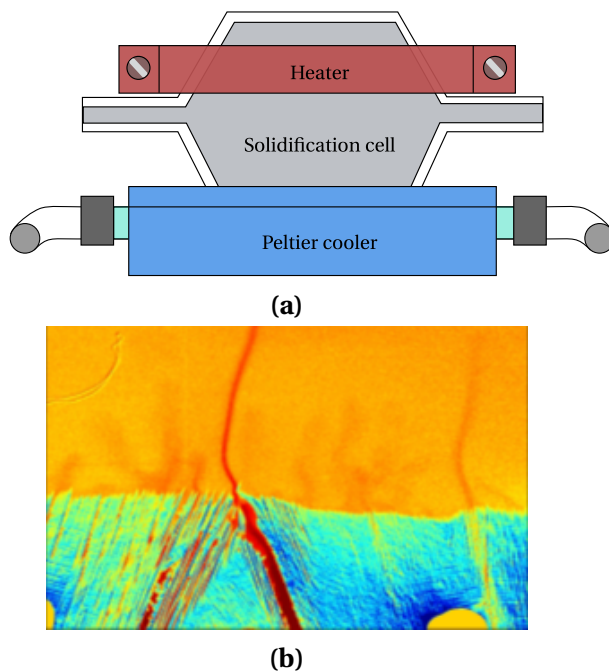


**Fig. 4.5** – Illustration of the benchmark experiments for in-situ observation of freckle formation using X-Ray radiography with (a) a schematic of the cell and (b) a typical image of the microstructure formed during directional solidification of an In-75 wt.% Ga alloy. Reproduced from [\[Shevchenko et al. 2013\]](#).

### 4.6.3 Macroscopic scale simulations

#### Configuration

The focus of this section is on qualitative comparison between numerical simulation and the previously mentioned experiment. The experimental cell geometry shown in

[fig. 1.6](#) is hexagonal. With adiabatic lateral sides, it results in a bending of the isotherm surfaces as shown in the experiment. The metallic cooling plates shown in [fig. 4.5a](#) partly compensate for this effect. However, a residual horizontal component of the temperature gradient remains. To qualitatively replicate this effect while simplifying the cell geometry, a 22 mm × 22 mm × 1 mm cuboid cell is considered with small cooling fluxes on its lateral vertical side surfaces computed using a constant heat transfer coefficient,  $h_{\text{ext}}$ , and a constant environment temperature,  $T_{\text{ext}}$ . Temperatures at the bottom and top surfaces, respectively  $T_{\text{Top}}$  and  $T_{\text{Bottom}}$ , are imposed in a way to maintain a constant vertical gradient,  $G$ , thus linearly decreasing over time with the same cooling rate  $R$ . Both square faces of the geometry, having an area of 22 mm × 22 mm, are adiabatic. In spite of taking cell dimensions similar to benchmark experiments presented above, the cell thickness is increased from 150 µm to 1 mm. This facilitates the computation and will later be subject to discussion.

**Table 4.1** – Summary of the simulations and the corresponding parameters for the FE cases, for a purely macroscopic model. Parameters are varied from (G1) low to (G2) high gradient, (R1) low to (R2) high cooling rate and (L0) no, (L1) low and (L2) high lateral cooling.

Case	aaa	sss	aaa	ffff	ffddfd
lll	ccc	sss	aaa	ffff	ffddfd
lll	ccc	sss	aaa	ffff	ffddfd

Materials properties are provided in [table 4.2](#) while initial and boundary conditions are given in [table 4.1](#). A series of computations is performed to understand the influence of process parameters on the final macrosegregation pattern. In directional growth, the main parameters are the vertical temperature gradient,  $G$ , and the cooling rate,  $R$ , since they control the isotherms speed. However, the effect of a higher lateral cooling is also considered below by increasing the heat transfer coefficient,  $h_{\text{ext}}$ . Finally, the grain structure is another crucial parameter that drastically changes the analysis inasmuch as growth undercooling is fundamental to determine the onset of solidification. The computation cases used in this study are presented in [table 4.1](#). The label of each case allows direct access to the simulation parameters as explained in the caption. Values for these parameters are inspired from the above experiments ([section 4.6.2](#)). Initial conditions consider a quiescent liquid at uniform composition given by the nominal alloy composition  $\langle w_0 \rangle$ . The temperature field is also initially uniform at a temperature averaged between the top and bottom initial values provided in [table 4.1](#). It has been checked that a uniform temperature gradient is swiftly reached, and that the unsteady regime to settle a vertical temperature gradient does not affect the phenomena studied. For simulations with grain structures, boundary conditions for nucleation at the bottom horizontal 22 mm × 1 mm surface are kept constant as given in [table 4.1](#).

The macroscale approach employs the finite element method to compute the tem-

perature and composition fields at FE nodes. The liquid fraction is then determined directly from the former fields, assuming a linear phase diagram, i.e. linear liquidus with full thermodynamic equilibrium between phases or lever rule approximation. This linear approximation is made available by the dotted line provided in fig. 4.6. Note that this line defines a phase diagram that seems very different from the correct one. However, this linear fit is only used in a composition region located around the nominal composition of the alloy. It is also worth noticing that the eutectic microstructure is expected to appear at 15.3 °C. However, experimental observations revealed that large eutectic nucleation undercooling was reached, so the eutectic solidification was not reported in the experiments studied by Shevchenko et al. [2013]. Consequently, the solidification path is computed without accounting for the eutectic microstructure in the present simulations, thus extending the liquidus and solidus lines below the eutectic temperature as sketched with the linear approximations in fig. 4.6.

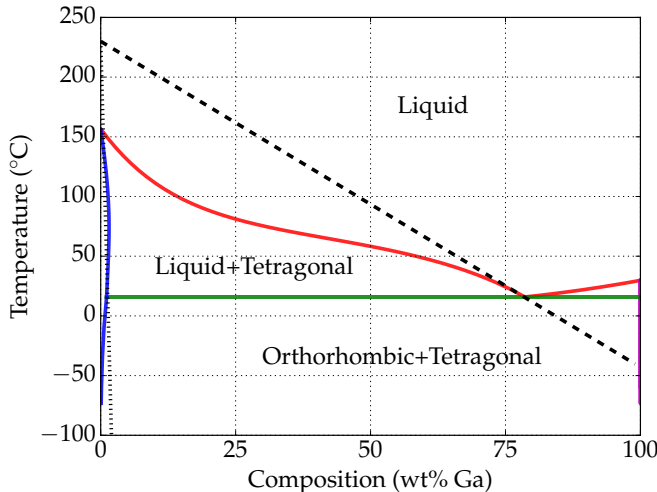


**Fig. 4.6** – Binary phase diagram of the In-Ga system [Andersson et al. 2002; TCBIN 2006] and its approximation for solidification studies with an In-75 wt.% Ga alloy. The dashed and dotted lines are linear liquidus and solidus approximations near the nominal composition.

## Results

The first case labeled FE-G1R1L0 is a reference case that features a low gradient (G1), low cooling rate (R1), and without any lateral cooling (L0), ensuring that isotherms retain a planar shape. These simulation parameters defined in table 4.2, result in a negligible fluid flow reaching a maximum velocity of  $4 \times 10^{-8}$  mm s<sup>-1</sup> in the bulk. Accordingly, the solidification front remains stable and follows the planar isotherms; no freckles are observed. The average composition field is thus only little modified in the mushy zone as shown in fig. 4.7 (mind the values of the scale limits). It is concluded

## 4.6. Macroscopic freckle prediction

---

**Table 4.2** – Material parameters for In-75 wt.% Ga and numerical parameters.

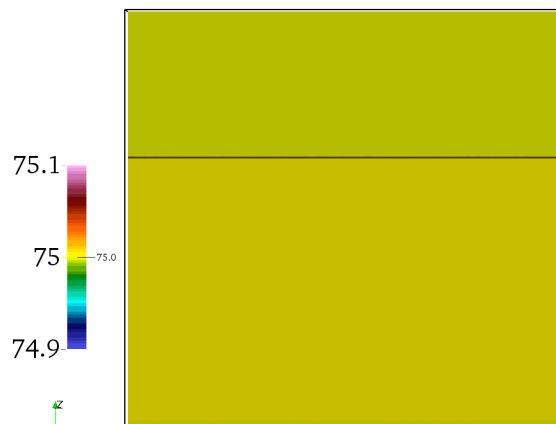
Parameter	Symbol	Value	Unit
Nominal composition	$\langle w_0 \rangle$	75	wt.%
Liquidus temperature	$T_l$	25.25	°C
Segregation coefficient	$k$	0.0165	wt.% wt.% <sup>-1</sup>
Liquidus slope	$m_l$	-2.73	K wt.% <sup>-1</sup>
Gibbs-Thomson coefficient	$\Gamma_{GT}$	$2 \times 10^{-7}$	°C m <sup>-1</sup>
Heat capacity (liquid and solid)	$C_p$	380.74	J kg <sup>-1</sup> K <sup>-1</sup>
Enthalpy of fusion	$L$	$8.02 \times 10^{-4}$	J kg <sup>-1</sup>
Diffusion coefficient of Ga in liquid In	$D^l$	$1.525 \times 10^{-9}$	m <sup>2</sup> s <sup>-1</sup>
Dynamic viscosity	$\mu^l$	$2 \times 10^{-3}$	Pas
Thermal expansion coefficient	$\beta_T$	$0.0978 \times 10^{-3}$	K <sup>-1</sup>
Solutal expansion coefficient	$\beta_{\langle w \rangle^l}$	$1.44 \times 10^{-3}$	wt.% <sup>-1</sup>
Thermal conductivity in the solid	$\langle \kappa^s \rangle$	40	W m <sup>-1</sup> K <sup>-1</sup>
Thermal conductivity in the liquid	$\langle \kappa^l \rangle$	28	W m <sup>-1</sup> K <sup>-1</sup>
Dendrite arm spacing	$\lambda$	$60 \times 10^{-6}$	m
Density	$\rho_0^l$	6725	kg m <sup>-3</sup>
Reference composition	$w_0^l$	75	wt.%
Reference temperature	$T_0$	25.25	°C
Initial temperature	$T_{init}$	1395	°C
Ingot diameter		$25 \times 10^{-3}$	m
Ingot length		$75 \times 10^{-3}$	m
CA cell size		$30 \times 10^{-6}$	m
FE mesh size		$140 \times 10^{-6}$	m
Time step	$\Delta t$	0.1	s

that velocity in the bulk is not high enough to initiate instabilities. In the next case, FE-G1R1L1, a cooling flux with a constant and very low value of the heat transfer coefficient is imposed on both vertical lateral surfaces to initiate a downward fluid flow by thermal buoyancy. Once solidification starts, solute-rich regions start to appear on the sides of the domain. Despite the visible concentration difference between these lateral regions and the central mush seen in fig. 4.7, their diffuse and uniform aspect indicates no resemblance to freckles. We keep the same configuration but increase the vertical gradient from 0.2 K mm<sup>-1</sup> (G1) to 1.5 K mm<sup>-1</sup> (G2) in the case FE-G2R1L1. The isotherms become closer to each other hence reducing the depth of the mushy zone for the same time increment compared to the preceding case. The rejected gallium solute locally accumulates at several different positions in the mushy zone, stemming from the base of the cell, with a maximum of 0.7 wt.%Ga above nominal composition. This is the consequence of segregation of gallium rich liquid being lighter than the above liquid bulk and creating an upward buoyancy force. The positive

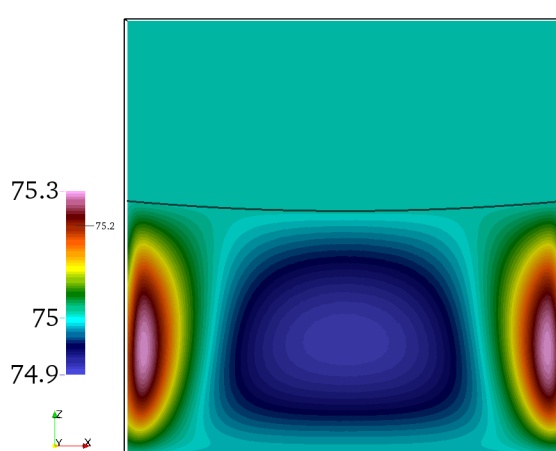
## Chapter 4. Macrosegregation with liquid metal motion

---

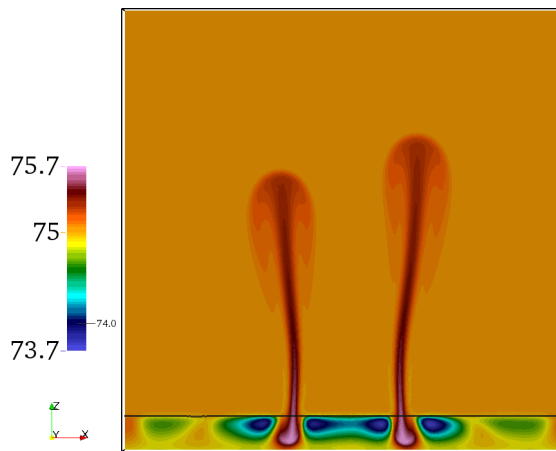
segregation and subsequent Ga-rich chimneys then rise up with an upward velocity component slightly greater than  $1 \text{ mm s}^{-1}$ . [Figure 4.8](#) gives a series of snapshots for case FE-G2R1L1 at three different times. Among the two clear distinct plumes that are visible at 250 s in [fig. 4.7](#), only one has led to the formation of a freckle that remains in [fig. 4.8](#) at 500 s. In fact, an animation between 250 s and 500 s (not shown here) reveals that one plume vanishes, thus permitting the first one to further develop. A second freckle is also seen on the left hand side of the cell. These two freckles are stable for a long time since they remain at time 1000 s. However, the left side freckle develops further to become the main one at 1500 s, while the mid-width freckle decreases in intensity, changes orientation and subsequently disappears (not shown here). Thus, the birth and death of very few freckles is observed in this simulation, mainly due to solutal instability, as the temperature field shown in [fig. 4.8](#) clearly remains stable despite the low lateral heat flux. As shown in [fig. 4.7](#), instability is yet required to create these chemical plumes and channels. Here, it is created by a very small lateral heat flow but other sources of instability could be involved, as shown with the grain structure in the next section.



(a) FE-G1R1L0



(b) FE-G1R1L1



(c) FE-G2R1L1

**Fig. 4.7** – Average Ga composition field at 250 s for the 3 FE cases showing the influence of process parameters on the freckling tendency. The black line represents the liquidus isotherm given in [table 4.2](#).

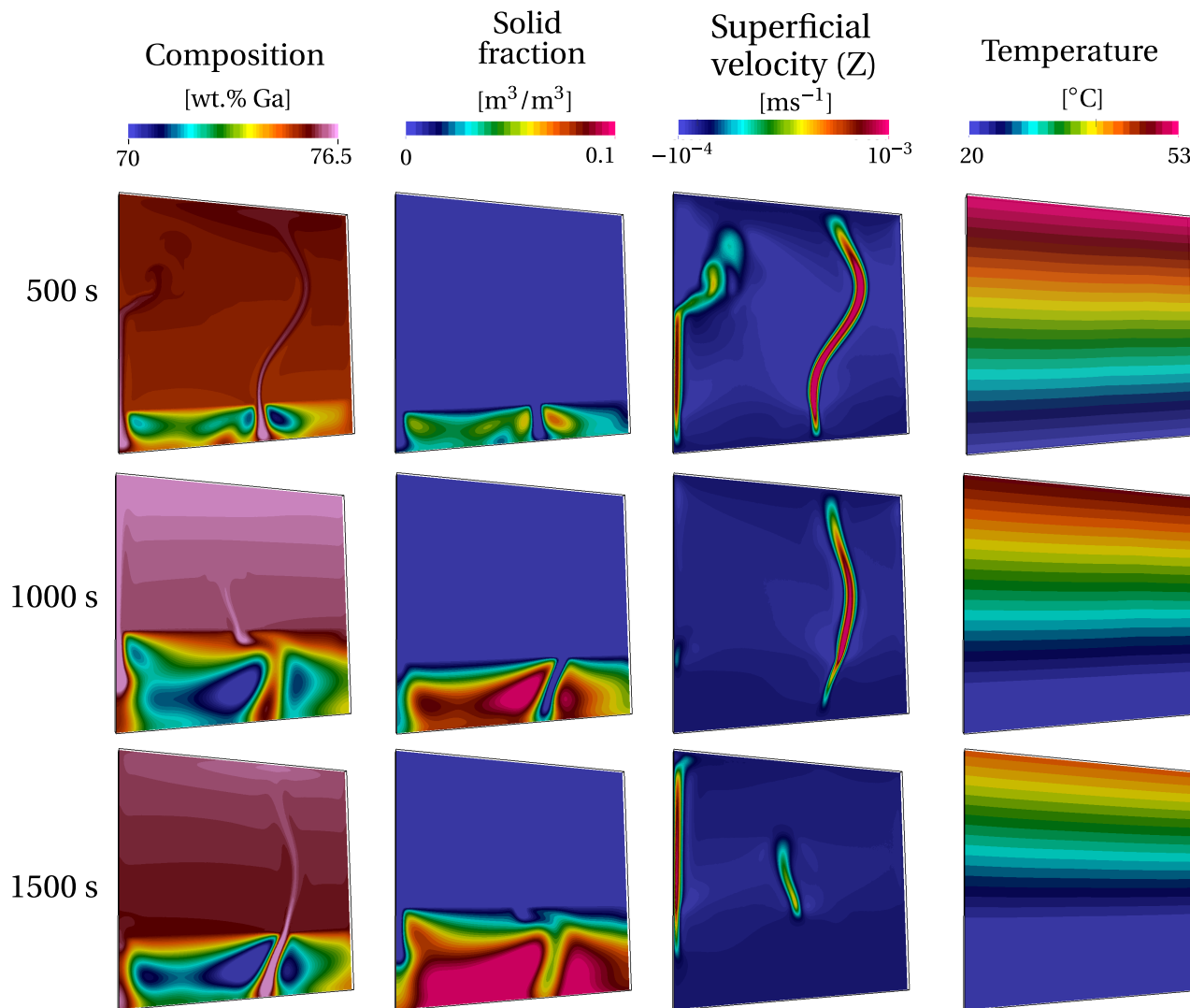


**Fig. 4.8** – Simulation results for case FE-G2R1L1 showing maps of the average composition in gallium, the solid fraction, the superficial velocity field (vertical component) and the temperature, on a cut plane at the center of the cell at 500 s, 1000 s and 1500 s.

### Discussion

In section 4.6.1, we have introduced some successful attempts of freckle predictions. The authors tackled the problem from an qualitative perspective. To our knowledge, the closest work to quantitative freckling analysis in solidification literature was done by Ramirez et al. [2003]. They attempted to draw a correlation (freckling criterion) between the process parameters and the occurrence of freckles, (without any size or shape constraints, i.e. any flow instability that may appear and form the smallest freckle is considered). To accomplish this, they took a number of experiments done independently by Pollock et al. [1996] and Auburtin et al. [2000] where the casting parameters vary one at a time: casting speed ( $R$ ), thermal gradient ( $G$ ), angle ( $\theta$ ) with respect to vertical orientation and nominal composition ( $\langle w_0 \rangle$ ), giving a database for 6 different superalloys. The experimental results were compared to a modified Rayleigh number that accounts for the various parameters. It allowed them to define a threshold for freckle formation in Nickel-base superalloys, as well as Pb-Sn alloys. Other contributions by Yuan et al. [2012] and Karagadde et al. [2014] used a medium scale model to compare the simulated formation of freckles with the results obtained by Shevchenko et al. [2013] (explain at bit more) However, all simulations show common traits in their predictions: (some words about the freckle dimensions, shape, intensity). These properties do not exactly meet with the experimental observations, just like in the In-Ga experiment. We think that the hydrodynamics scale at which freckles are born, is much smaller than the FEM scale. Since the relevant physics are not solved, even the finest FE mesh will not be enough to see the exact grain boundaries.

## 4.7 Meso-Macro freckle prediction

### 4.7.1 Numerical method

#### Microscopic scale

The CAFE model introduces a grid of regular and structured cubic cells, with a constant size in all space directions, referred to as the cellular automaton (CA) grid. It is different from the unstructured finite element mesh previously mentioned for the solution of the average conservation equations. A typical CA step dimension is smaller than the smallest FE mesh size. The CA grid serves to represent solidification phenomena including nucleation, growth and remelting of the envelope of the primary dendritic grains. Details about the CAFE model can be found in [Carozzani et al. 2012; Carozzani et al. 2013; Carozzani et al. 2014]. Cell information, such as the temperature, the average composition or the velocity of the liquid phase, is interpolated from the nodes of the FE mesh. State indices are also defined for each CA cell, providing the presence of liquid or solid phases.

### Nucleation

Initially, cells are in a fully liquid state. In the present situation, random nucleation sites are chosen based on a nucleation density,  $n_{\max}$  (expressed in surface density inverse m<sup>-2</sup>), at the bottom surface of the geometry in contact with the cooler. Nucleation occurs in a cell only if the latter contains a nucleation site, and when the local undercooling of the cell reaches the critical nucleation undercooling given as input by a Gaussian distribution of mean undercooling  $\Delta T_N$  with a standard deviation  $\Delta T_\sigma$ . The crystallographic orientation of each grain newly nucleated is also randomly chosen using values of the Euler angles to fully define the three rotations that transform the reference frame to the  $\langle 100 \rangle$  directions that define the main growth axes of the dendrite trunks and arms. Grain selection is therefore solely controlled by growth competition.

### Growth

Dendrite growth is driven by the chemical supersaturation  $\Omega_{\text{saturation}}$ , which is a dimensionless number proportional to the difference between the liquid composition at the dendrite tip and the melt composition far away from the tip. The higher the supersaturation, the faster the dendrite tip velocity. However, in the presence of a convective fluid, the chemical supersaturation is highly influenced by the intensity and the direction of the flow with respect to the growth direction of the dendrites. In the current model, convection is central in studying freckle formation. Therefore, the purely diffusive Ivantsov relation used to determine the Peclet number  $Pe$  as function of the supersaturation, is replaced by a modified relation using a boundary layer correlation model that accounts for both the intensity and the misorientation of the liquid velocity with respect to the growth direction of the dendrites [Gandin et al. 2003]. The main parameters for this growth kinetics models are the Gibbs Thomson coefficient,  $\Gamma_{\text{GT}}$ , and the diffusion coefficient for Ga in In,  $D^l$ .

### Solidification path

The CA model gives the presence of the grains in the liquid as well as its growth undercooling. For coupling with macroscopic scale modelling, the fraction of phases needs to be fed back to the FE model. This is now done by accounting for the information provided by the CA model. Thus, the fraction of solid is no longer the consequence of a simple conversion of the temperature and composition assuming thermodynamic equilibrium. It also includes the solidification delay due to the kinetics of the development of the grains as detailed elsewhere in the work of Carozzani et al. [2013].

## Numerical method

Both the finite element mesh and the cellular automaton grid play a role in predicting freckles inasmuch as this type of defect originate from interplays between hydrodynamic instabilities on the scale of the dendrites and macroscopic flows defined by the geometry of the experimental cell [Shevchenko et al. 2013]. One has to respect a small maximum FE mesh size, comparable to the dendrite arm spacing. With such an element size, composition gradients giving rise to solutal buoyancy forces can be captured. This limits consequently the CA cell size, as a minimum number of cells is required in each finite element. In the array of simulations that will be presented in the next section, the value of  $\lambda_2$  was considered. We have chosen a fixed mesh element size of  $2\lambda_2$  and a CA cell size of  $\lambda_2/2$ . An average of 4 CA cells per unit length of a finite element is enough to accurately compute the development of the grain envelopes together with the solutal, thermal and mechanical interactions.

### 4.7.2 Configuration

**Table 4.3** – Summary of the simulations and the corresponding parameters for the CAFE cases, coupling macroscopic model with the grain structure model. Parameters are varied from (G1) low to (G2) high gradient, (R1) low to (R2) high cooling rate and (L0) no, (L1) low and (L2) high lateral cooling.

Case	Vertical gradient		sss	aaa	ffff	ffddfd
	(G)	$K$				
	lll	ccc				
lll	ccc		sss	aaa	ffff	ffddfd
lll	ccc		sss	aaa	ffff	ffddfd

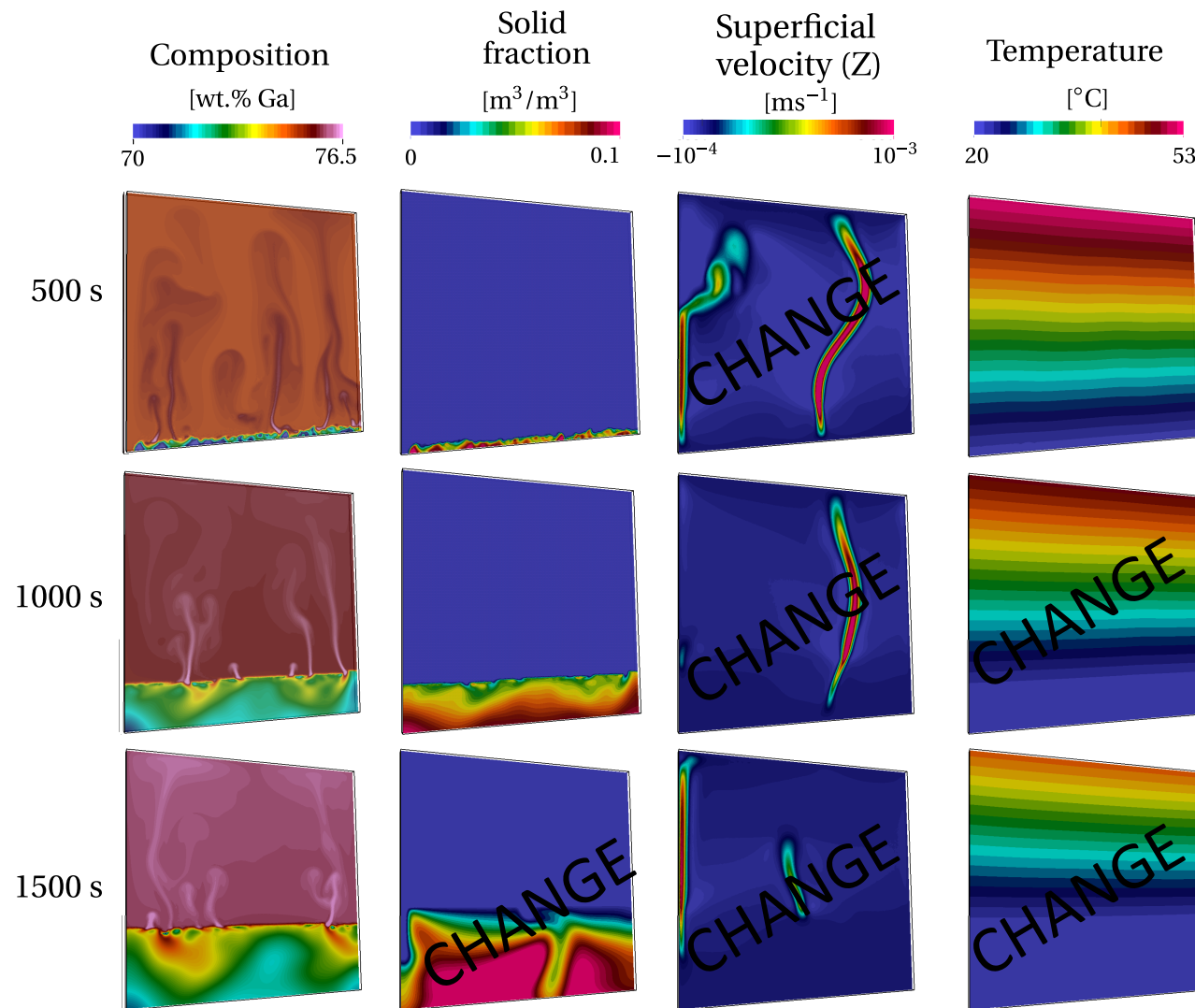


**Fig. 4.9 –** Simulation results for case CAFE-G2R1L1 showing maps of the average composition in gallium, the solid fraction, the superficial velocity field (vertical component) and the temperature, on a cut plane at the center of the cell at 500 s, 1000 s and 1500 s.

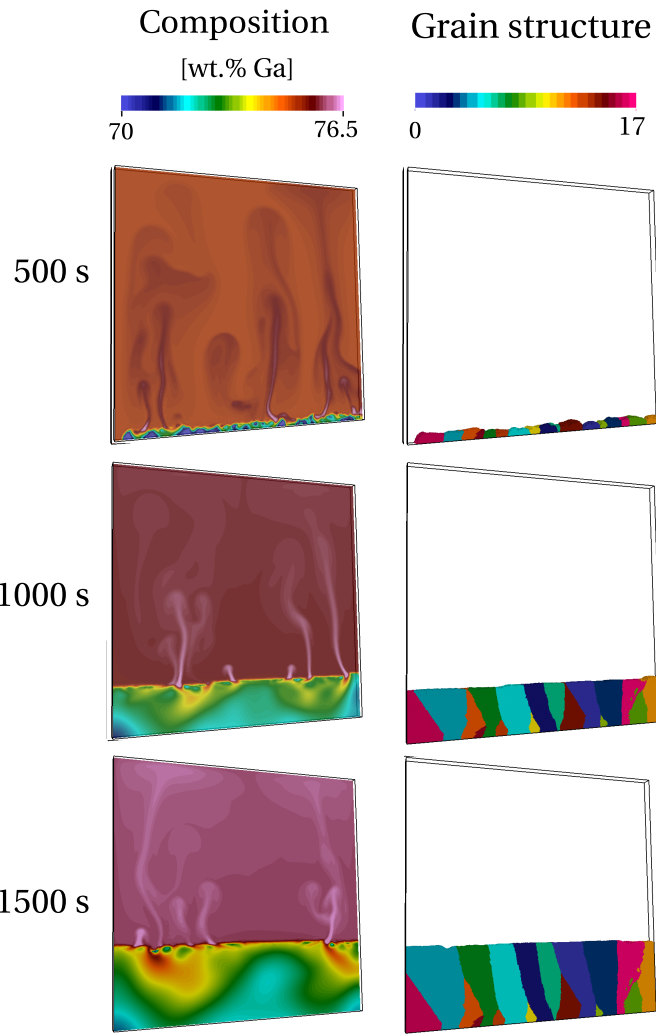


**Fig. 4.10** – Simulation results the predicted of mushy grain structure with the corresponding composition maps.

Knowing that the configuration in FE-G2R1L1 produces freckles, the same set of parameters is first used for case CAFE-G2R1L1 by adding the effect of the grain structure using the CAFE model. Results are accessible in [fig. 4.9](#) for comparison with [fig. 4.8](#). A striking difference is seen: the composition maps become more perturbed as shown by the formation of numerous plumes when coupling with grain structure is active. The growing front displayed on the grain structure at the right most column of [fig. 4.9](#) dictates the leading position of the mushy zone shown in the third column. Note that each color corresponds to one grain, with 17 grains having nucleated at the cell's bottom surface. However, comparison of the solid fraction maps between [fig. 4.8](#) and [fig. 4.9](#) at the same times reveals a delay in the growing front position. Values of the nucleation parameters in [table 4.3](#) are such that few grains rapidly form below the nominal liquidus isotherm. The delay is therefore not due to the nucleation under-

cooling but to the growth undercooling of the dendrite tips. It should be noticed that, the growth front driven by undercooling in [fig. 4.9](#) also forms with a higher initial solid fraction and hence larger solute segregation occurs at the front. This effect, together with instabilities of the composition field, is caused by a more perturbed fluid flow and more plumes as observed in CAFE-G2R1L1 compared to FE-G2R1L1. Such observations fit to the complicated fluid and solute flow patterns typically occurring in the experiments as shown in [fig. 4.11](#). It becomes obvious that the consideration of grain structure and growth undercooling are vital to accurately simulate freckle formation in these experiments. The reasons for the instabilities are discussed hereinafter. In the present 3D CAFE simulation, each grain shown in [fig. 4.10](#) is associated with a crystallographic orientation. The growth kinetics is only given for the  $\langle 100 \rangle$  crystallographic directions at the grain boundaries with the liquid. The CA growth model is based on the hypothesis that, in a quiescent liquid of uniform temperature distribution and composition, the grain envelop should reproduce an octahedral grain shape with main directions given by the six  $\langle 100 \rangle$  directions. In the present situation where complicated fields are present for temperature, composition and liquid velocity, each grain envelope with different crystallographic orientation adapts differently to its local environment. Thus, the local undercooling of the front varies everywhere. Such variations are within few degrees here, but this is sufficient to create irregularities on the growth front, as seen on the grain structure in [fig. 4.10](#). Apart from that, these variations are linked to the position of the instabilities for the chemical and liquid velocity fields, thus demonstrating the full coupling between the CA and FE models.

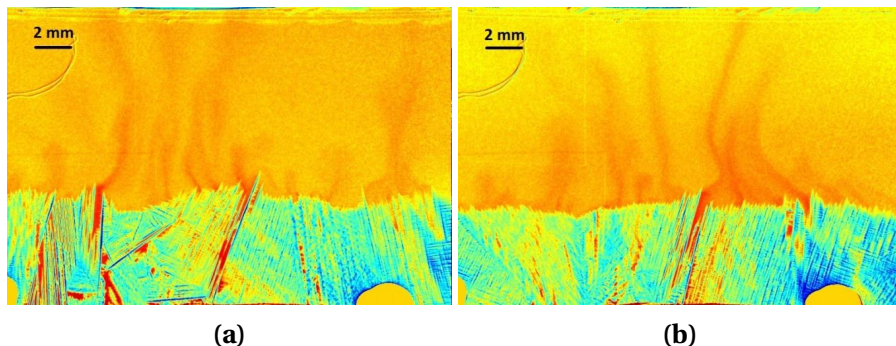


**Fig. 4.11** – Snapshots of dendritic structure and composition field obtained from two solidification experiments at a cooling rate  $R=-0.01 \text{ K s}^{-1}$  and temperature gradients of (a)  $G=1.1 \text{ K mm}^{-1}$  and (b)  $G=1.3 \text{ K mm}^{-1}$

#### 4.7.3 Effect of vertical temperature gradient

The influence of diverse process parameters can now be considered in context of the grain structure. The effect of the vertical temperature gradient is shown by comparing the previous case CAFE-G2R1L1 with case CAFE-G1R1L1. The temperature gradient

is decreased about 7 times here, from  $G_2=1.5 \text{ K mm}^{-1}$  to  $G_1=0.2 \text{ K mm}^{-1}$ . In fact, both cases share almost all traits with respect to flow patterns and velocity magnitude in the bulk. Main differences are yet seen regarding the dynamics of the plumes shown in fig. 4.12. In the case of a low temperature gradient ( $G_1$ ), the solidification front cannot maintain a shape as smooth as for the case of a large temperature gradient ( $G_2$ ): the solute gradient in the liquid of the mushy zone (basically following the lever rule approximation for a given temperature) decreases, leading to a lower gradient of the solutal buoyancy force. In turn, more solute accumulates close to the front and locally reduces the growth velocity, thus creating larger “valleys” or steps with higher solute content. The irregular geometry of the front is also influenced by the dendrite tip growth kinetics model. The velocity of the isotherms is the ratio of the cooling rate,  $R$ , to the temperature gradient,  $G$ . Consequently, the isotherm velocity in case  $G_1$  is larger than in  $G_2$ , since cooling rate,  $R_1$ , is the same in both cases. Moreover, because the dendrite tip velocity is a monotonously increasing function with the undercooling [Gandin et al. 2003], the latter for CAFE-G1R1L1 is larger than for CAFE-G2R1L1. Height differences of the growth front are proportional to the variations of the undercooling by the temperature gradient. Therefore, this forms larger steps on the growth front for case  $G_1$  compared to  $G_2$ . The freckle extends deeper in the mushy zone when the temperature gradient increases. This is confirmed by both the simulation results shown in fig. 4.12 as well as the experimental observations. Another remarkable phenomenon is also observed in the low gradient case: a “pulsing” mechanism in CAFE-G1R1L1 where a series of solute rich liquid pockets are observed one above the other. This corresponds to a repeated and localized strong spatial variation of the liquid velocity field outside the mushy zone, regularly thrusting away small plumes. These pulses are roughly similar to each other in size and exit speed, creating thus a very regular pattern during some time. In the case of a high temperature

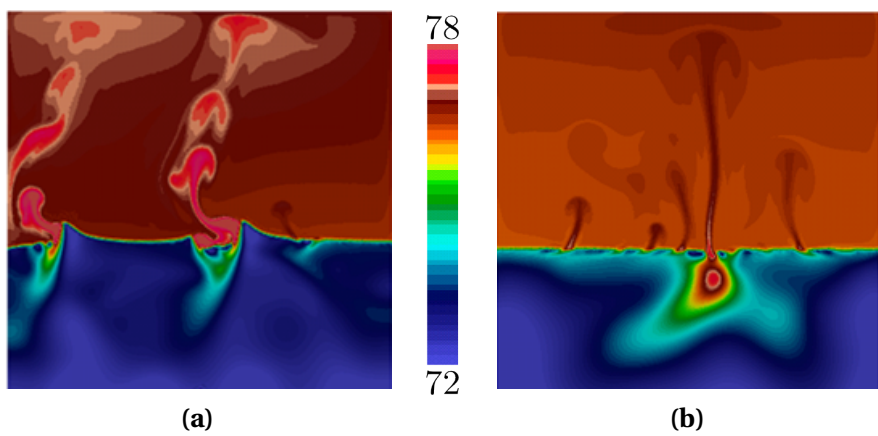


**Fig. 4.12** – Average composition maps for CAFE-G1R1L1 at time 1060 s and CAFE-G2R1L1 at time 1845 s.

**Fig. 4.13** – Animation of the pulsing mechanism coming from a groove shape in the mushy.

gradient (case CAFE-G2R1L1) this phenomenon is barely seen. In fact, the pattern shown in [fig. 4.12](#) is more typical, with continuous plume rising from the mushy zone and reaching the top of the domain. However, such regular plume is the initial and final pattern seen for low gradient before the pulsing regime. Similar observations have been made in the experiments too. [Figure 4.14a](#) displays the phenomenon of the “pulsing” plumes, which could be explained by the following mechanisms. The permeability of the mushy zone and the narrow gap of the solidification cell obstruct the feeding of the plumes by solute. A critical solute concentration has to be accumulated at a specific location in order to trigger the formation of a rising plume. An interim drop of the solute concentration below such a threshold would interrupt the plume. Flow instabilities can be another reason for the peculiar shape of the plumes. [Figure 4.14b](#) shows a pronounced continuous plume. The same plume can be seen a few seconds later in [fig. 4.14c](#). The plume structure becomes unstable; one can observe an indentation of streamlines followed by a mixing of rising solute-rich liquid with descending In-rich fluid. This mechanism also causes a non-continuous structure of the plumes.

#### **4.7.4 Effect of cooling rate**

The next parameter studied is the cooling rate, corresponding to case CAFE-G1R2L1. A snapshot of the composition map and the corresponding vertical component of the velocity field are given in [fig. 4.15](#). We see a similarity with case CAFE-G1R1L1 in [fig. 4.12a](#) with respect to the buckled interface between the liquid and the mushy zone as well a plume pulsing effect when a low temperature gradient is applied. On the other hand, segregation inside the mush is more irregular with more pronounced

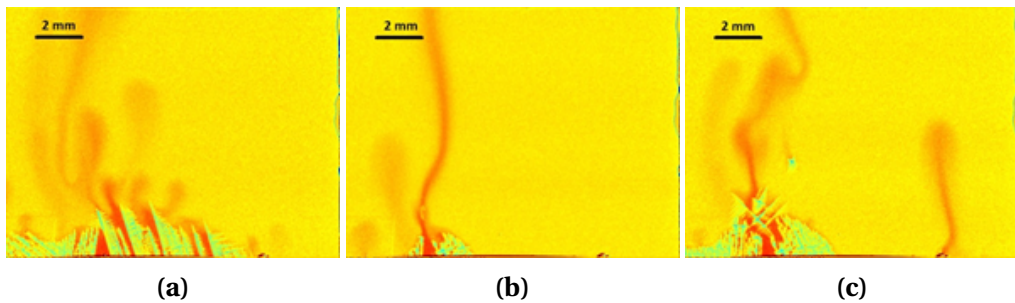


**Fig. 4.14** – Snapshots of dendrite structure and composition field from two solidification experiments conducted at a cooling rate  $R=-0.01 \text{ K s}^{-1}$  and a temperature gradient  $=1 \text{ K mm}^{-1}$ : (a) “pulsing” plumes, (b) continuous plume, (c) upcoming plume instability.

patterns reaching a larger depth. One could distinguish alternating V and A shapes patterns in the mushy zone. As for case CAFE-G1R1L1, these patterns are created by a network of pulsing plumes formed by the steps created on the delocalized growth front due to the low temperature gradient. However, these considerations are not sufficient to explain the shape of the growth front. The reason for the protuberances created at the tips of the V shape is the presence of a descending bulk liquid with a low composition seen by the growth front. It infers that favorable growth conditions are created for a higher working temperature since the dendrite tip undercooling decreases for facing liquid flow and a lower composition; the growth rate is given by the isotherm velocity. The growth front thus adjusts its position to catch up with the corresponding isotherm, the latter being located at the tips of the V shape, i.e. the outmost advanced position of the growth front. It also means that the V shape angle depends on the size and intensity of the convection loops above the front. When the steps are formed on the growth front, the plumes exiting the mushy zone follow a direction normal to the front. They are inclined towards each other above the V shape. As a result, they may join and form a larger plume as seen in CAFE-G1R1L1 ([fig. 4.12a](#)), thus forming larger and more stable freckles. The other observation in [fig. 4.15](#) is the existence of stable regions of the growth front. For instance, this is seen in between the two V shape forming or on the right hand side of the cell. The reason for this stability is the inversion of the composition gradient located ahead. Animation shows that solute coming from the top of the cell is responsible for this accumulation, creating a layering that provides a stabilization effect above the mushy zone. This is verified by the vertical component of the average velocity also made available in [fig. 4.15](#). It is negative outside the path of the plumes. A resulting concurrent effect is the formation of the A shape segregates in between the V shape patterns seen in [fig. 4.15](#). Finally, it can be observed that these patterns are sustained longer compared to [fig. 4.12](#) CAFE-G1R1L1 because, at high cooling rate, the flow in the mushy zone is decreased due to a faster solidification. This is the same effect as described for the large gradient configuration in CAFE-G2R1L1 ([fig. 4.12b](#)). It is not clear how these observations could be compared

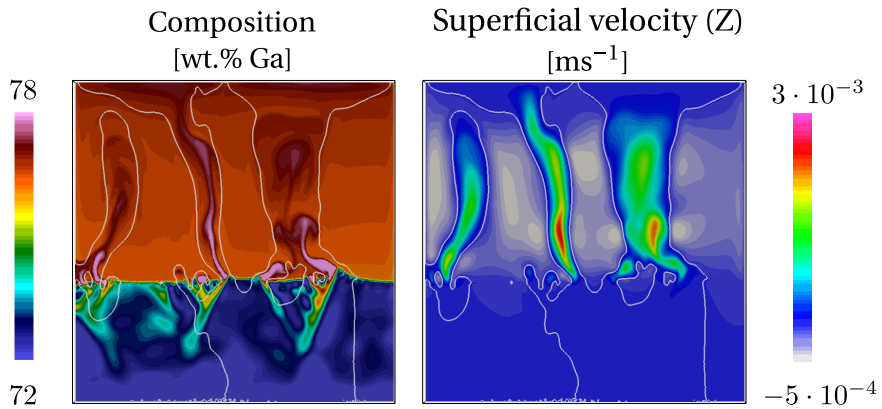


**Fig. 4.15** – Average fields inside the cell for case CAFE-G1R2L1 at 350 s. The white contour identifies the zero velocity limit for the vertical component of the velocity field

with the A and V shapes segregates reported for steel ingots [Pickering 2013]. Despite the fact that macrosegregation is the main phenomenon leading to these patterns, there has not been a clear explanation yet in the literature for their formation. However, for steel casting, the A and V patterns are believed to form concomitantly. Further investigations would thus be required to quantify the consequences of thermosolutal instabilities simulated here for an In-75 wt.% Ga alloy and check their possible correlation with experimental observations in steel casting.

#### 4.7.5 Effect of lateral temperature gradient

The previous simulations show the effect of cooling rate and temperature gradient on the survival of segregation patterns deep in the mushy zone. Another simulation is performed by increasing the cooling rate using higher heat flux extracted from the vertical side boundaries. This is achieved in case CAFE-G1R1L2 where the heat transfer coefficient reaches  $500 \text{ W m}^{-2} \text{ K}^{-1}$ . As a consequence of the large cooling from the sides, the temperature gradient is no longer vertical. A distinct flow due to thermal buoyancy is created, driving a cold liquid downwards near the sides of the cell. Under the influence of these 2 main convection loops, all segregation plumes tend to regroup in the middle of the domain, forming a larger central plume, as seen in the composition map at 450 s in [fig. 4.16](#). However, this regime occurs at times earlier than 500 s, where the effect of thermally induced buoyancy forces is prevailing, feeding the convection loops. Approximately 500 s later, the mushy zone has extended, favoring the segregation mechanical forces i.e.  $\rho_{\text{ref}} \left( 1 - \beta_{\langle w \rangle^l} \Delta \langle w \rangle^l \right) \vec{g}$ , rather than the thermal mechanical forces,  $\rho_{\text{ref}} (1 - \beta_T \Delta T) \vec{g}$ . [Figure 4.16](#) shows the corresponding composition maps with stable freckles at about 1000 s that also remain at 1500 s. The solidification front then tends to form a concave shape at the center of the cell, thus partially revealing the form of the isotherms toward the cell center. The stable pattern in the center is similar to the plateau seen at the center of the A shapes in [fig. 4.12](#)

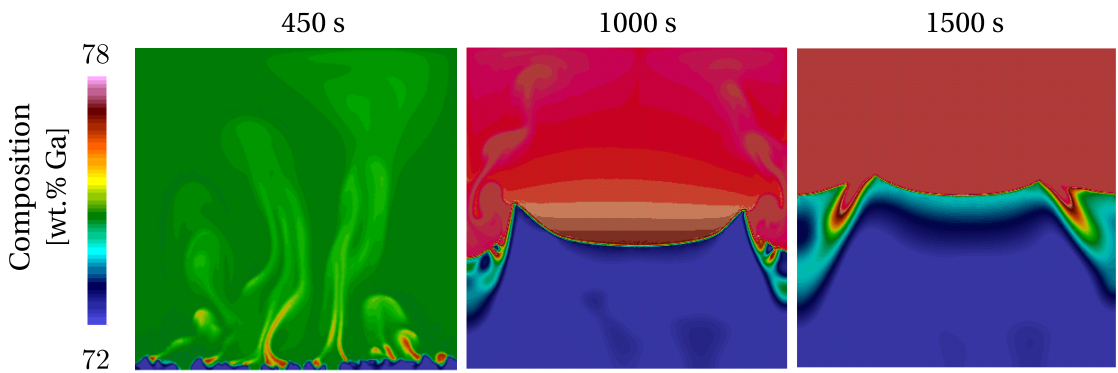


**Fig. 4.16** – 2D cut plane of the average composition inside the cell for case CAFE-G1R1L2 at the following time increments: 450 s, 1000 s and 1500 s.

and [fig. 4.15](#). As stated before, it is an inactive region with respect to plume initiation due to the inversion of the solute composition gradient. The composition field indeed shows accumulation of solute on top of the plateau in an established cuvette where no flow comes to destabilize the layering of solute. Outside of the plateau, 2 plumes are observed from the prominent instabilities of the growth front, adopting diverging directions. This is also observed at the center of the cell in [fig. 4.15](#) on each side of the A shape segregate. These plumes in [fig. 4.16](#) lead to the formation of two stable freckles. Liquid channels then form below the growth front. The corresponding situation in the experiment is shown in [fig. 4.17](#). The two freckles on both side and the plateau in between are clearly recognizable. The additional cooling at the side walls produces two flow vortices between the side wall and the strong plumes above the freckles. The central part of the sample remains almost unaffected by the additionally driven thermal convection. This area is characterized by the occurrence of a number of smaller plumes.

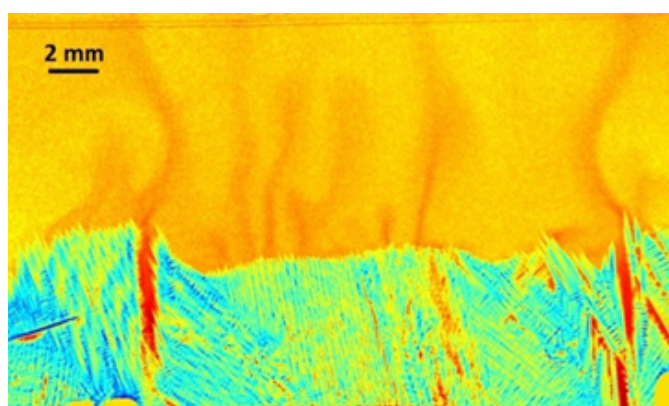


**Fig. 4.17** – Snapshot of dendritic structure and composition field from a solidification experiment recorded at 1000 s for a cooling rate  $R=-0.01 \text{ K s}^{-1}$  and a temperature gradient  $G=-1 \text{ K mm}^{-1}$ .



# Bibliography

## [AFS 2014]

AFS (2014). *American Foundry Society: Understanding Porosity*. URL: <http://www.afsinc.org/about/content.cfm?ItemNumber=6933> (cited on page 3).

## [Andersson et al. 2002]

Andersson, J.-O., Helander, T., Höglund, L., Shi, P., and Sundman, B. (2002). “Thermo-Calc & DICTRA, computational tools for materials science”. *Calphad*, 26 (2), pp. 273–312. URL: <http://www.sciencedirect.com/science/article/pii/S0364591602000378> (cited on pages 57, 59, 74).

## [Arnold et al. 1984]

Arnold, D. N., Brezzi, F., and Fortin, M. (1984). “A stable finite element for the stokes equations”. *CALCOLO*, 21 (4), pp. 337–344. URL: <http://link.springer.com/article/10.1007/BF02576171> (cited on page 64).

## [Auburtin et al. 2000]

Auburtin, P., Wang, T., Cockcroft, S. L., and Mitchell, A. (2000). “Freckle formation and freckle criterion in superalloy castings”. *Metallurgical and Materials Transactions B*, 31 (4), pp. 801–811. URL: <http://link.springer.com/article/10.1007/s11663-000-0117-9> (cited on page 79).

## [Auburtin 1998]

Auburtin, P. B. L. (1998). “Determination of the influence of growth front angle on freckle formation in superalloys”. PhD thesis. Vancouver, BC, Canada: University of British Columbia. URL: [https://circle.ubc.ca/bitstream/handle/2429/8676/ubc\\_1998-345084.pdf?sequence=1](https://circle.ubc.ca/bitstream/handle/2429/8676/ubc_1998-345084.pdf?sequence=1) (cited on page 71).

## [Basset 2006]

Basset, O. (2006). “Simulation numérique d’écoulements multi-fluides sur grille de calcul”. PhD Thesis. École Nationale Supérieure des Mines de Paris. URL: <https://tel.archives-ouvertes.fr/tel-00376484> (cited on page 33).

## [Beckermann 2002]

Beckermann, C. (2002). “Modelling of macrosegregation: applications and future needs”. *International Materials Reviews*, 47 (5), pp. 243–261. URL: <http://www.maneyonline.com/doi/abs/10.1179/095066002225006557> (cited on pages 5, 6).

## Bibliography

---

### [Beckermann et al. 1999]

Beckermann, C., Diepers, H. J., Steinbach, I., Karma, A., and Tong, X (1999). “Modeling Melt Convection in Phase-Field Simulations of Solidification”. *Journal of Computational Physics*, 154 (2), pp. 468–496. URL: <http://www.sciencedirect.com/science/article/pii/S0021999199963234> (cited on page 28).

### [Beckermann et al. 2000]

Beckermann, C., Gu, J. P., and Boettinger, W. J. (2000). “Development of a freckle predictor via rayleigh number method for single-crystal nickel-base superalloy castings”. *Metallurgical and Materials Transactions A*, 31 (10), pp. 2545–2557. URL: <http://link.springer.com/article/10.1007/s11661-000-0199-7> (cited on pages 66, 71).

### [Bellet et al. 2009]

Bellet, M. et al. (2009). “Call for contributions to a numerical benchmark problem for 2D columnar solidification of binary alloys”. *International Journal of Thermal Sciences*, 48 (11), pp. 2013–2016. URL: <http://www.sciencedirect.com/science/article/pii/S129007290900177X> (cited on page 40).

### [Boden et al. 2008]

Boden, S., Eckert, S., Willers, B., and Gerbeth, G. (2008). “X-Ray Radioscopic Visualization of the Solutal Convection during Solidification of a Ga-30 Wt Pct In Alloy”. *Metallurgical and Materials Transactions A*, 39 (3), pp. 613–623. URL: <http://link.springer.com/article/10.1007/s11661-007-9462-5> (cited on page 72).

### [Boettinger et al. 2002]

Boettinger, W. J., Warren, J. A., Beckermann, C., and Karma, A. (2002). “Phase-Field Simulation of Solidification1”. *Annual Review of Materials Research*, 32 (1), pp. 163–194. URL: <http://dx.doi.org/10.1146/annurev.matsci.32.101901.155803> (cited on page 26).

### [Brackbill et al. 1992]

Brackbill, J. U., Kothe, D. B., and Zemach, C (1992). “A continuum method for modeling surface tension”. *Journal of Computational Physics*, 100 (2), pp. 335–354. URL: <http://www.sciencedirect.com/science/article/pii/002199919290240Y> (cited on page 29).

### [Brooks et al. 1982]

Brooks, A. N. and Hughes, T. J. R. (1982). “Streamline upwind/Petrov-Galerkin formulations for convection dominated flows with particular emphasis on the incompressible Navier-Stokes equations”. *Computer Methods in Applied Mechanics and Engineering*, 32 (1–3), pp. 199–259. URL: <http://www.sciencedirect.com/science/article/pii/0045782582900718> (cited on page 32).

### [Carozzani et al. 2012]

Carozzani, T., Digonnet, H., and Gandin, C.-A. (2012). “3D CAFE modeling of grain structures: application to primary dendritic and secondary eutectic solidification”. *Modelling and Simulation in Materials Science and Engineering*, 20 (1), p. 015010. URL: <http://iopscience.iop.org/0965-0393/20/1/015010> (cited on page 79).

**[Carozzani et al. 2014]**

Carozzani, T., Gandin, C.-A., and Digonnet, H. (2014). "Optimized parallel computing for cellular automaton-finite element modeling of solidification grain structures". *Modelling and Simulation in Materials Science and Engineering*, 22 (1), p. 015012. URL: <http://iopscience.iop.org/0965-0393/22/1/015012> (cited on page 79).

**[Carozzani 2012]**

Carozzani, T. (2012). "Développement d'un modèle 3D Automate Cellulaire-Éléments Finis (CAFE) parallèle pour la prédition de structures de grains lors de la solidification d'alliages métalliques". PhD Thesis. Ecole Nationale Supérieure des Mines de Paris. URL: <http://pastel.archives-ouvertes.fr/pastel-00803282> (cited on pages 10, 54).

**[Carozzani et al. 2013]**

Carozzani, T. et al. (2013). "Direct Simulation of a Solidification Benchmark Experiment". *Metallurgical and Materials Transactions A*, 44 (2), pp. 873–887. URL: <http://link.springer.com/article/10.1007/s11661-012-1465-1> (cited on pages 40, 54, 55, 79, 80).

**[Chen et al. 1997]**

Chen, S., Merriman, B., Osher, S., and Smereka, P. (1997). "A Simple Level Set Method for Solving Stefan Problems". *Journal of Computational Physics*, 135 (1), pp. 8–29. URL: <http://www.sciencedirect.com/science/article/pii/S0021999197957211> (cited on page 26).

**[Chen 2014]**

Chen, S. (2014). "Three dimensional Cellular Automaton - Finite Element (CAFE) modeling for the grain structures development in Gas Tungsten / Metal Arc Welding processes". PhD Thesis. Ecole Nationale Supérieure des Mines de Paris. URL: <https://pastel.archives-ouvertes.fr/pastel-01038028> (cited on page 27).

**[Clyne et al. 1981]**

Clyne, T. W. and Kurz, W. (1981). "Solute redistribution during solidification with rapid solid state diffusion". *Metallurgical Transactions A*, 12 (6), pp. 965–971. URL: <http://link.springer.com/article/10.1007/BF02643477> (cited on page 18).

**[Combeau et al. 1996]**

Combeau, H., Drezet, J.-M., Mo, A., and Rappaz, M. (1996). "Modeling of microsegregation in macrosegregation computations". *Metallurgical and Materials Transactions A*, 27 (8), pp. 2314–2327. URL: <http://link.springer.com/article/10.1007/BF02651886> (cited on page 18).

**[Combeau et al. 2009]**

Combeau, H., Založník, M., Hans, S., and Richy, P. E. (2009). "Prediction of Macrosegregation in Steel Ingots: Influence of the Motion and the Morphology of Equiaxed Grains". *Metallurgical and Materials Transactions B*, 40 (3), pp. 289–304. URL: <http://link.springer.com/article/10.1007/s11663-008-9178-y> (cited on page 6).

## Bibliography

---

### [Copley et al. 1970]

Copley, S. M., Giamei, A. F., Johnson, S. M., and Hornbecker, M. F. (1970). “The origin of freckles in unidirectionally solidified castings”. *Metallurgical Transactions*, 1 (8), pp. 2193–2204. URL: <http://link.springer.com/article/10.1007/BF02643435> (cited on page 69).

### [Courtois et al. 2014]

Courtois, M., Carin, M., Masson, P. L., Gaied, S., and Balabane, M. (2014). “A complete model of keyhole and melt pool dynamics to analyze instabilities and collapse during laser welding”. *Journal of Laser Applications*, 26 (4), p. 042001. URL: <http://scitation.aip.org/content/jia/journal/jla/26/4/10.2351/1.4886835> (cited on page 27).

### [Dantzig et al. 2009]

Dantzig, J. A. and Rappaz, M. (2009). *Solidification*. EPFL Press (cited on pages 3, 14, 18, 19, 21, 22, 44).

### [Darcy 1856]

Darcy, H. (1856). *Les fontaines publiques de la ville de Dijon : exposition et application des principes à suivre et des formules à employer dans les questions de distribution d'eau*. V. Dalmont (Paris). URL: <http://gallica.bnf.fr/ark:/12148/bpt6k624312> (cited on page 15).

### [Desbiolles et al. 2003]

Desbiolles, J.-L., Thévoz, P., Rappaz, M., and Stefanescu, D. (2003). “Micro-Macrosegregation Modeling in Casting: A Fully Coupled 3D Model”. TMS Publ., pp. 245–252 (cited on page 71).

### [Desmaison et al. 2014]

Desmaison, O., Bellet, M., and Guillemot, G. (2014). “A level set approach for the simulation of the multipass hybrid laser/GMA welding process”. *Computational Materials Science*, 91, pp. 240–250. URL: <http://www.sciencedirect.com/science/article/pii/S092702561400278X> (cited on page 27).

### [Digonnet et al. 2007]

Digonnet, H., Silva, L., and Coupez, T. (2007). “Cimlib: A Fully Parallel Application For Numerical Simulations Based On Components Assembly”. *AIP Conference Proceedings*. Vol. 908. AIP Publishing, pp. 269–274. URL: <http://scitation.aip.org/content/aip/proceeding/aipcp/10.1063/1.2740823> (cited on page 10).

### [Dijkstra 1959]

Dijkstra, E. W. (1959). “A note on two problems in connexion with graphs”. *Numerische Mathematik*, 1 (1), pp. 269–271. URL: <http://link.springer.com/article/10.1007/BF01386390> (cited on page 36).

### [DLR 2014]

DLR (2014). *ElectroMagnetic Levitation*. <http://goo.gl/e5JhiA> (cited on page 9).

**[DoITPoMS 2000]**

DoITPoMS (2000). *Dissemination of IT for the Promotion of Materials Science*. URL: <http://www.doitpoms.ac.uk/> (cited on page 15).

**[Doré et al. 2000]**

Doré, X., Combeau, H., and Rappaz, M. (2000). “Modelling of microsegregation in ternary alloys: Application to the solidification of Al–Mg–Si”. *Acta Materialia*, 48 (15), pp. 3951–3962. URL: <http://www.sciencedirect.com/science/article/pii/S1359645400001774> (cited on page 40).

**[Du et al. 2007]**

Du, Q., Eskin, D. G., and Katgerman, L. (2007). “Modeling Macrosegregation during Direct-Chill Casting of Multicomponent Aluminum Alloys”. *Metallurgical and Materials Transactions A*, 38 (1), pp. 180–189. URL: <http://link.springer.com/article/10.1007/s11661-006-9042-0> (cited on page 40).

**[Du et al. 2001]**

Du, Q., Li, D., Li, Y., Li, R., and Zhang, P. (2001). “Simulating a double casting technique using level set method”. *Computational Materials Science*, 22 (3–4), pp. 200–212. URL: <http://www.sciencedirect.com/science/article/pii/S0927025601001902> (cited on page 27).

**[Easton et al. 2011]**

Easton, M., Davidson, C., and StJohn, D. (2011). “Grain Morphology of As-Cast Wrought Aluminium Alloys”. *Materials Transactions*, 52 (5), pp. 842–847 (cited on page 14).

**[ESAB 2014]**

ESAB (2014). *New Lean Duplex Steels*. URL: <http://www.esab.com/global/en/education/new-lean-duplex-steels.cfm> (cited on page 3).

**[Ettrich et al. 2014]**

Ettrich, J. et al. (2014). “Modelling of transient heat conduction with diffuse interface methods”. *Modelling and Simulation in Materials Science and Engineering*, 22 (8), p. 085006. URL: <http://iopscience.iop.org/0965-0393/22/8/085006> (cited on page 31).

**[Felicelli et al. 1991]**

Felicelli, S. D., Heinrich, J. C., and Poirier, D. R. (1991). “Simulation of freckles during vertical solidification of binary alloys”. *Metallurgical Transactions B*, 22 (6), pp. 847–859. URL: <http://link.springer.com/article/10.1007/BF02651162> (cited on pages 7, 15, 68, 71).

**[Felicelli et al. 1998]**

Felicelli, S. D., Poirier, D. R., and Heinrich, J. C. (1998). “Modeling freckle formation in three dimensions during solidification of multicomponent alloys”. *Metallurgical and Materials Transactions B*, 29 (4), pp. 847–855. URL: <http://link.springer.com/article/10.1007/s11663-998-0144-5> (cited on page 71).

## Bibliography

---

### [Flemings 1974]

Flemings, M. C. (1974). "Solidification processing". *Metallurgical Transactions*, 5 (10), pp. 2121–2134. URL: <http://link.springer.com/article/10.1007/BF02643923> (cited on page 6).

### [Flemings et al. 1967]

Flemings, M. C. and Nereo, G. E. (1967). "Macrosegregation: Part I". *Transactions of the Metallurgical Society of AIME*, 239, pp. 1449–1461 (cited on pages 15, 71).

### [Flemings et al. 1968a]

Flemings, M. C., Mehrabian, R., and Nereo, G. E. (1968a). "Macrosegregation: Part II". *Transactions of the Metallurgical Society of AIME*, 242, pp. 41–49 (cited on pages 15, 71).

### [Flemings et al. 1968b]

Flemings, M. C. and Nereo, G. E. (1968b). "Macrosegregation: Part III". *Transactions of the Metallurgical Society of AIME*, 242, pp. 50–55 (cited on pages 15, 71).

### [Gada et al. 2009]

Gada, V. H. and Sharma, A. (2009). "On Derivation and Physical Interpretation of Level Set Method-Based Equations for Two-Phase Flow Simulations". *Numerical Heat Transfer, Part B: Fundamentals*, 56 (4), pp. 307–322. URL: <http://dx.doi.org/10.1080/10407790903388258> (cited on page 29).

### [Gandin 2000]

Gandin, C. A. (2000). "From constrained to unconstrained growth during directional solidification". *Acta Materialia*, 48 (10), pp. 2483–2501. URL: <http://www.sciencedirect.com/science/article/pii/S1359645400000707> (cited on page 49).

### [Gandin et al. 2003]

Gandin, C. A., Guillemot, G., Appolaire, B., and Niane, N. T. (2003). "Boundary layer correlation for dendrite tip growth with fluid flow". *Materials Science and Engineering: A*, 342 (1–2), pp. 44–50. URL: <http://www.sciencedirect.com/science/article/pii/S0921509302002617> (cited on pages 80, 85).

### [Genereux et al. 2000]

Genereux, P. D. and Borg, C. A. (2000). "Characterization of Freckles in a High Strength Wrought Nickel Superalloy". Warrendale, PA: K.A. Green, M. McLean, S. Olson, J.J. Schirra, TMS (The Minerals, Metals, and Materials Society), pp. 19–27. URL: [http://www.tms.org/superalloys/10.7449/2000/Superalloys\\_2000\\_19\\_27.pdf](http://www.tms.org/superalloys/10.7449/2000/Superalloys_2000_19_27.pdf) (cited on page 71).

### [Giamei et al. 1970]

Giamei, A. F. and Kear, B. H. (1970). "On the nature of freckles in nickel base superalloys". *Metallurgical Transactions*, 1 (8), pp. 2185–2192. URL: <http://link.springer.com/article/10.1007/BF02643434> (cited on pages 7, 71).

### [Gibou et al. 2003]

Gibou, F., Fedkiw, R., Caflisch, R., and Osher, S. (2003). "A Level Set Approach for the Numerical Simulation of Dendritic Growth". *Journal of Scientific Computing*, 19 (1–3),

- pp. 183–199. URL: <http://link.springer.com/article/10.1023/A%3A1025399807998> (cited on page 26).
- [Gouttebroze 2005]**  
Gouttebroze, S. (2005). “Modélisation 3d par éléments finis de la macroségrégation lors de la solidification d’alliages binaires”. PhD thesis. École Nationale Supérieure des Mines de Paris. URL: <https://pastel.archives-ouvertes.fr/pastel-00001885/document> (cited on page 10).
- [Guo et al. 2003]**  
Guo, J. and Beckermann, C. (2003). “Three-Dimensional Simulation of Freckle Formation During Binary Alloy Solidification: Effect of Mesh Spacing”. *Numerical Heat Transfer, Part A: Applications*, 44 (6). <http://dx.doi.org/10.1080/716100512>, pp. 559–576. URL: <http://user.engineering.uiowa.edu/~becker/documents.dir/GuoFreckle.pdf> (cited on page 71).
- [Hachani et al. 2012]**  
Hachani, L. et al. (2012). “Experimental analysis of the solidification of Sn–3 wt.%Pb alloy under natural convection”. *International Journal of Heat and Mass Transfer*, 55 (7–8), pp. 1986–1996. URL: <http://www.sciencedirect.com/science/article/pii/S0017931011007009> (cited on page 54).
- [Hachem et al. 2010]**  
Hachem, E., Rivaux, B., Kloczko, T., Digonnet, H., and Coupez, T. (2010). “Stabilized finite element method for incompressible flows with high Reynolds number”. *Journal of Computational Physics*, 229 (23), pp. 8643–8665. URL: <http://www.sciencedirect.com/science/article/pii/S0021999110004237> (cited on page 65).
- [Hachem 2009]**  
Hachem, E. (2009). “Stabilized finite element method for heat transfer and turbulent flows inside industrial furnaces”. PhD Thesis. École Nationale Supérieure des Mines de Paris. URL: <https://tel.archives-ouvertes.fr/tel-00443532> (cited on page 65).
- [Harlow et al. 1965]**  
Harlow, F. H. and Welch, J. E. (1965). “Numerical Calculation of Time-Dependent Viscous Incompressible Flow of Fluid with Free Surface”. *Physics of Fluids (1958-1988)*, 8 (12), pp. 2182–2189. URL: <http://scitation.aip.org/content/aip/journal/pof1/8/12/10.1063/1.1761178> (cited on page 26).
- [Hebditch et al. 1974]**  
Hebditch, D. J. and Hunt, J. D. (1974). “Observations of ingot macrosegregation on model systems”. *Metallurgical Transactions*, 5 (7), pp. 1557–1564. URL: <http://link.springer.com/article/10.1007/BF02646326> (cited on page 54).
- [Hirt 1971]**  
Hirt, C. W. (1971). “An arbitrary Lagrangian-Eulerian computing technique”. *Proceedings of the Second International Conference on Numerical Methods in Fluid Dynamics*.

## Bibliography

---

Ed. by M. Holt. Lecture Notes in Physics 8. Springer Berlin Heidelberg, pp. 350–355. URL: [http://link.springer.com/chapter/10.1007/3-540-05407-3\\_50](http://link.springer.com/chapter/10.1007/3-540-05407-3_50) (cited on page 26).

### [Hirt et al. 1981]

Hirt, C. W and Nichols, B. D (1981). “Volume of fluid (VOF) method for the dynamics of free boundaries”. *Journal of Computational Physics*, 39 (1), pp. 201–225. URL: <http://www.sciencedirect.com/science/article/pii/0021999181901455> (cited on page 26).

### [Hysing et al. 2009]

Hysing, S. et al. (2009). “Quantitative benchmark computations of two-dimensional bubble dynamics”. *International Journal for Numerical Methods in Fluids*, 60 (11), pp. 1259–1288. URL: <http://onlinelibrary.wiley.com/doi/10.1002/fld.1934/abstract> (cited on page 34).

### [Karagadde et al. 2014]

Karagadde, S., Yuan, L., Shevchenko, N., Eckert, S., and Lee, P. D. (2014). “3-D microstructural model of freckle formation validated using in situ experiments”. *Acta Materialia*, 79, pp. 168–180. URL: <http://www.sciencedirect.com/science/article/pii/S1359645414004984> (cited on page 79).

### [Karma et al. 1996]

Karma, A. and Rappel, W.-J. (1996). “Phase-field method for computationally efficient modeling of solidification with arbitrary interface kinetics”. *Physical Review E*, 53 (4), R3017–R3020. URL: <http://link.aps.org/doi/10.1103/PhysRevE.53.R3017> (cited on page 26).

### [Khan et al. 2014]

Khan, M. I., Mostafa, A. O., Aljarrah, M., Essadiqi, E., and Medraj, M. (2014). “Influence of Cooling Rate on Microsegregation Behavior of Magnesium Alloys”. *Journal of Materials*, 2014, e657647. URL: <http://www.hindawi.com/journals/jma/2014/657647/abs/> (cited on page 18).

### [Kobayashi 1988]

Kobayashi, S. (1988). “Solute redistribution during solidification with diffusion in solid phase: A theoretical analysis”. *Journal of Crystal Growth*, 88 (1), pp. 87–96. URL: <http://www.sciencedirect.com/science/article/pii/S0022024898900100> (cited on page 18).

### [Kohler 2008]

Kohler, F. (2008). “Peritectic solidification of Cu-Sn alloys: microstructure competition at low speed”. PhD Thesis. EPFL (cited on page 71).

### [Lesoult 2005]

Lesoult, G. (2005). “Macrosegregation in steel strands and ingots: Characterisation, formation and consequences”. *Materials Science and Engineering: A*, International Conference on Advances in Solidification Processes 413–414, pp. 19–29. URL: <http://www.sciencedirect.com/science/article/pii/S0921509305010063> (cited on page 6).

**[Liu 2005]**

Liu, W. (2005). "Finite Element Modelling of Macrosegregation and Thermomechanical Phenomena in Solidification Processes". PhD thesis. École Nationale Supérieure des Mines de Paris. URL: <http://pastel.archives-ouvertes.fr/pastel-00001339> (cited on page 10).

**[Maitre 2006]**

Maitre, E. (2006). "Review of numerical methods for free interfaces". Les Houches, France. URL: <http://goo.gl/Re6f3a> (cited on page 26).

**[Martorano et al. 2003]**

Martorano, M. A., Beckermann, C., and Gandin, C.-A. (2003). "A solutal interaction mechanism for the columnar-to-equiaxed transition in alloy solidification". *Metallurgical and Materials Transactions A*, 34 (8), pp. 1657–1674. URL: <http://link.springer.com/article/10.1007/s11661-003-0311-x> (cited on page 18).

**[Mesri et al. 2009]**

Mesri, Y., Digonnet, H., and Coupez, T. (2009). "Advanced parallel computing in material forming with CIMLib". *European Journal of Computational Mechanics/Revue Européenne de Mécanique Numérique*, 18 (7-8), pp. 669–694. URL: <http://www.tandfonline.com/doi/abs/10.3166/ejcm.18.669-694> (cited on page 10).

**[Mosbah 2008]**

Mosbah, S. (2008). "Multiple scales modeling of solidification grain structures and segregation in metallic alloys". PhD thesis. École Nationale Supérieure des Mines de Paris. URL: <https://tel.archives-ouvertes.fr/tel-00349885/document> (cited on page 10).

**[Ni et al. 1991]**

Ni, J. and Beckermann, C. (1991). "A volume-averaged two-phase model for transport phenomena during solidification". *Metallurgical Transactions B*, 22 (3), pp. 349–361. URL: <http://link.springer.com/article/10.1007/BF02651234> (cited on pages 18, 19, 21).

**[Osher et al. 1988]**

Osher, S. and Sethian, J. A. (1988). "Fronts propagating with curvature-dependent speed: Algorithms based on Hamilton-Jacobi formulations". *Journal of Computational Physics*, 79 (1), pp. 12–49. URL: <http://www.sciencedirect.com/science/article/pii/0021999188900022> (cited on pages 26, 27).

**[Osher et al. 2003]**

Osher, S. and Fedkiw, R. (2003). "Signed Distance Functions". *Level Set Methods and Dynamic Implicit Surfaces*. Applied Mathematical Sciences 153. Springer New York, pp. 17–22. URL: [http://link.springer.com/chapter/10.1007/0-387-22746-6\\_2](http://link.springer.com/chapter/10.1007/0-387-22746-6_2) (cited on page 36).

**[Peng et al. 1999]**

Peng, D., Merriman, B., Osher, S., Zhao, H., and Kang, M. (1999). "A PDE-Based Fast Local Level Set Method". *Journal of Computational Physics*, 155 (2), pp. 410–438. URL:

## Bibliography

---

<http://www.sciencedirect.com/science/article/pii/S0021999199963453> (cited on pages 29, 35).

### [Pickering 2013]

Pickering, E. J. (2013). "Macrosegregation in Steel Ingots: The Applicability of Modelling and Characterisation Techniques". *ISIJ International*, 53 (6), pp. 935–949 (cited on pages 71, 88).

### [Poirier 1987]

Poirier, D. R. (1987). "Permeability for flow of interdendritic liquid in columnar-dendritic alloys". *Metallurgical Transactions B*, 18 (1), pp. 245–255. URL: <http://link.springer.com/article/10.1007/BF02658450> (cited on page 15).

### [Pollock et al. 1996]

Pollock, T. M. and Murphy, W. H. (1996). "The breakdown of single-crystal solidification in high refractory nickel-base alloys". *Metallurgical and Materials Transactions A*, 27 (4), pp. 1081–1094. URL: <http://link.springer.com/article/10.1007/BF02649777> (cited on page 79).

### [Prosperetti 2002]

Prosperetti, A. (2002). "Navier-Stokes Numerical Algorithms for Free-Surface Flow Computations: An Overview". *Drop-Surface Interactions*. Ed. by M. Rein. CISM International Centre for Mechanical Sciences 456. Springer Vienna, pp. 237–257. URL: [http://link.springer.com/chapter/10.1007/978-3-7091-2594-6\\_8](http://link.springer.com/chapter/10.1007/978-3-7091-2594-6_8) (cited on page 26).

### [Ramirez et al. 2003]

Ramirez, J. C. and Beckermann, C. (2003). "Evaluation of a rayleigh-number-based freckle criterion for Pb-Sn alloys and Ni-base superalloys". *Metallurgical and Materials Transactions A*, 34 (7), pp. 1525–1536. URL: <http://link.springer.com/article/10.1007/s11661-003-0264-0> (cited on pages 15, 71, 79).

### [Rappaz et al. 2003]

Rappaz, M., Bellet, M., and Deville, M. (2003). *Numerical Modeling in Materials Science and Engineering*. Springer Series in Computational Mathematics. Springer Berlin Heidelberg (cited on pages 15, 20, 41, 44).

### [Rivaux 2011]

Rivaux, B. (2011). "Simulation 3D éléments finis des macroségrégations en peau induites par déformations thermomécaniques lors de la solidification d'alliages métalliques". PhD Thesis. École Nationale Supérieure des Mines de Paris. URL: <http://pastel.archives-ouvertes.fr/pastel-00637168> (cited on pages 9, 10, 54).

### [Sarazin et al. 1992]

Sarazin, J. R. and Hellawell, A. (1992). "Studies of Channel-Plume Convection during Solidification". *Interactive Dynamics of Convection and Solidification*. Ed. by S. H. Davis, H. E. Huppert, U. Müller, and M. G. Worster. NATO ASI Series 219. Springer Netherlands, pp. 143–145. URL: [http://link.springer.com/chapter/10.1007/978-94-011-2809-4\\_22](http://link.springer.com/chapter/10.1007/978-94-011-2809-4_22) (cited on page 3).

**[Schneider et al. 1997]**

Schneider, M. C., Gu, J. P., Beckermann, C., Boettinger, W. J., and Kattner, U. R. (1997). “Modeling of micro- and macrosegregation and freckle formation in single-crystal nickel-base superalloy directional solidification”. *Metallurgical and Materials Transactions A*, 28 (7), pp. 1517–1531. URL: <http://link.springer.com/article/10.1007/s11661-997-0214-3> (cited on pages 3, 71).

**[Sethian 1996]**

Sethian, J. A. (1996). “A fast marching level set method for monotonically advancing fronts”. *Proceedings of the National Academy of Sciences*, 93 (4), pp. 1591–1595. URL: <http://www.pnas.org/content/93/4/1591> (cited on page 36).

**[Shakoor et al. 2015]**

Shakoor, M., Scholtes, B., Bouchard, P.-O., and Bernacki, M. (2015). “An efficient and parallel level set reinitialization method - Application to micromechanics and microstructural evolutions”. *Applied Mathematical Modelling (submitted)*, (cited on page 36).

**[Shevchenko et al. 2013]**

Shevchenko, N., Boden, S., Gerbeth, G., and Eckert, S. (2013). “Chimney Formation in Solidifying Ga-25wt pct In Alloys Under the Influence of Thermosolutal Melt Convection”. *Metallurgical and Materials Transactions A*, 44 (8), pp. 3797–3808. URL: <http://link.springer.com/article/10.1007/s11661-013-1711-1> (cited on pages 3, 71, 72, 74, 79, 81).

**[Strotos et al. 2008]**

Strotos, G., Gavaises, M., Theodorakakos, A., and Bergeles, G. (2008). “Numerical investigation of the cooling effectiveness of a droplet impinging on a heated surface”. *International Journal of Heat and Mass Transfer*, 51 (19–20), pp. 4728–4742. URL: <http://www.sciencedirect.com/science/article/pii/S001793100800149X> (cited on page 31).

**[Süli 2000]**

Süli, E. (2000). *Lecture Notes on Finite Element Methods for Partial Differential Equations* (cited on page 43).

**[Sun et al. 2004]**

Sun, Y. and Beckermann, C. (2004). “Diffuse interface modeling of two-phase flows based on averaging: mass and momentum equations”. *Physica D: Nonlinear Phenomena*, 198 (3–4), pp. 281–308. URL: <http://www.sciencedirect.com/science/article/pii/S0167278904003689> (cited on page 28).

**[Sussman et al. 1994]**

Sussman, M., Smereka, P., and Osher, S. (1994). “A Level Set Approach for Computing Solutions to Incompressible Two-Phase Flow”. *Journal of Computational Physics*, 114 (1), pp. 146–159. URL: <http://www.sciencedirect.com/science/article/pii/S0021999184711557> (cited on pages 34, 35).

## Bibliography

---

### [Swaminathan. et al. 1993]

Swaminathan., C. R. and Voller, V. R. (1993). "On The Enthalpy Method". *International Journal of Numerical Methods for Heat & Fluid Flow*, 3 (3), pp. 233–244. URL: <http://www.emeraldinsight.com/journals.htm?articleid=1665561&show=abstract> (cited on page 40).

### [Tan et al. 2007]

Tan, L. and Zabaras, N. (2007). "A level set simulation of dendritic solidification of multi-component alloys". *Journal of Computational Physics*, 221 (1), pp. 9–40. URL: <http://www.sciencedirect.com/science/article/pii/S0021999106002737> (cited on page 26).

### [TCBIN 2006]

TCBIN (2006). *TCBIN: TC Binary Solutions Database*. Stockholm, SE (cited on page 74).

### [TCFE6 2010]

TCFE6 (2010). *TCFE6: a thermodynamic database for different kinds of steels and Fe-based alloys*. Stockholm, SE. URL: <http://goo.gl/qiD3kE> (cited on pages 57, 59).

### [Thuinet et al. 2004]

Thuinet, L. and Combeau, H. (2004). "Prediction of macrosegregation during the solidification involving a peritectic transformation for multicomponent steels". *Journal of Materials Science*, 39 (24), pp. 7213–7219. URL: <http://link.springer.com/article/10.1023/B%3AJMSC.0000048734.34597.1e> (cited on page 40).

### [Tiller et al. 1953]

Tiller, W. A, Jackson, K. A, Rutter, J. W, and Chalmers, B (1953). "The redistribution of solute atoms during the solidification of metals". *Acta Metallurgica*, 1 (4), pp. 428–437. URL: <http://www.sciencedirect.com/science/article/pii/0001616053901266> (cited on page 14).

### [Tourret et al. 2009]

Tourret, D. and Gandin, C. A. (2009). "A generalized segregation model for concurrent dendritic, peritectic and eutectic solidification". *Acta Materialia*, 57 (7), pp. 2066–2079. URL: <http://www.sciencedirect.com/science/article/pii/S1359645409000184> (cited on page 18).

### [Vigneaux 2007]

Vigneaux, P. (2007). "Méthodes Level Set pour des problèmes d'interface en microfluide". PhD thesis. Université Sciences et Technologies - Bordeaux I. URL: <https://tel.archives-ouvertes.fr/tel-00189409/document> (cited on page 35).

### [Ville et al. 2011]

Ville, L., Silva, L., and Coupez, T. (2011). "Convected level set method for the numerical simulation of fluid buckling". *International Journal for Numerical Methods in Fluids*, 66 (3), pp. 324–344. URL: <http://onlinelibrary.wiley.com/doi/10.1002/fld.2259/abstract> (cited on page 35).

## Bibliography

---

### [Wang et al. 1993]

Wang, C. Y. and Beckermann, C. (1993). "A multiphase solute diffusion model for dendritic alloy solidification". *Metallurgical Transactions A*, 24 (12), pp. 2787–2802. URL: <http://link.springer.com/article/10.1007/BF02659502> (cited on page 18).

### [WeldReality 2014]

WeldReality (2014). *Aluminum Alloys*. URL: <http://www.weldreality.com/aluminumalloys.htm> (cited on page 3).

### [WSA 2014]

WSA (2014). *World Steel Association: Statistics archive*. URL: <http://www.worldsteel.org/statistics/statistics-archive.html> (cited on page 8).

### [Xu et al. 1991]

Xu, D. and Li, Q. (1991). "Gravity- and Solidification-Shrinkage-Induced Liquid Flow in a Horizontally Solidified Alloy Ingot". *Numerical Heat Transfer, Part A: Applications*, 20 (2), pp. 203–221. URL: <http://dx.doi.org/10.1080/10407789108944817> (cited on page 15).

### [Yuan et al. 2012]

Yuan, L. and Lee, P. D. (2012). "A new mechanism for freckle initiation based on microstructural level simulation". *Acta Materialia*, 60 (12), pp. 4917–4926. URL: <http://www.sciencedirect.com/science/article/pii/S1359645412003205> (cited on page 79).